

AD-A040 769

PATTERN ANALYSIS AND RECOGNITION CORP ROME N Y  
ADVANCED DIGITAL EXPLOITATION TECHNIQUES (ADET).(U)  
APR 77 G E FORSEN, F H FENG, M J GILLOTTE

F/G 15/4

F30602-75-C-0141

UNCLASSIFIED

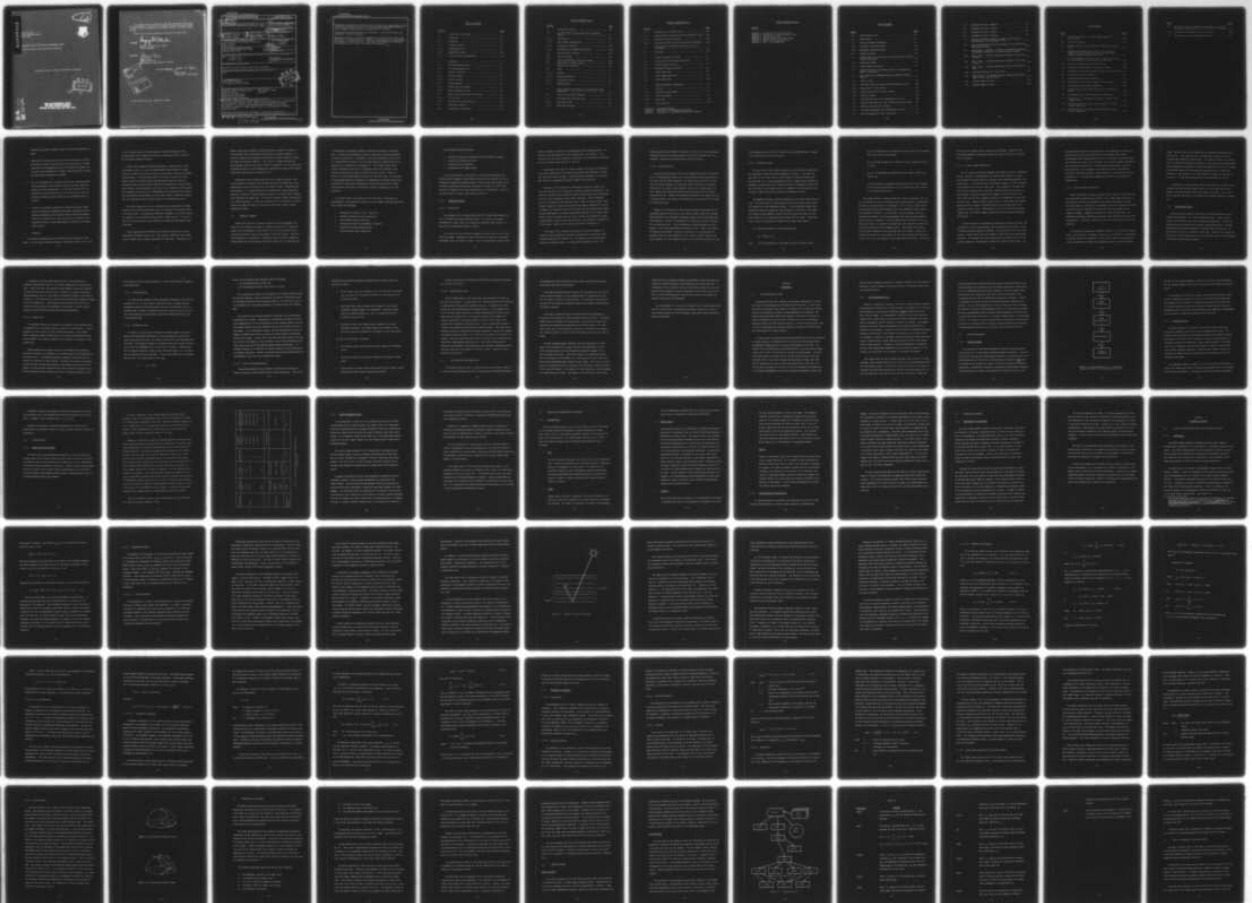
PAR-77-3

RADC-TR-77-145

NL

1 OF 3

AD  
A040769



ADA 040769

RADC-TR-77-145  
Final Technical Report  
April 1977

ADVANCED DIGITAL EXPLOITATION TECHNIQUES (ADET)  
Pattern Analysis and Recognition Corporation



Approved for public release; distribution unlimited.



AD No. \_\_\_\_\_  
DDC FILE COPY,

ROME AIR DEVELOPMENT CENTER  
AIR FORCE SYSTEMS COMMAND  
GRIFFISS AIR FORCE BASE, NEW YORK 13441



This report has been reviewed by the RADC Information Office (OI) and is releasable to the National Technical Information Service (NTIS). At NTIS it will be releasable to the general public, including foreign nations.

This report has been reviewed and approved for publication.

APPROVED:

*Gregory B. Pavlin*

GREGORY B. PAVLIN, 1/Lt, USAF  
Project Engineer

APPROVED:

*Howard Davis*

HOWARD DAVIS  
Technical Director  
Intelligence & Reconnaissance Division

Accession for	White Section	<input checked="" type="checkbox"/>
NTIS	Dist. Section	<input type="checkbox"/>
ONS		
UNANNOUNCED		
JUSTIFICATION		
BY	DISTRIBUTION AVAILABILITY CODES	
Dist.	Avail.	and/or SPECIAL
<i>PA</i>		

FOR THE COMMANDER:

*John P. Huss*

JOHN P. HUSS  
Acting Chief, Plans Office

Do not return this copy. Retain or destroy.

UNCLASSIFIED

SECURITY CLASSIFICATION OF THIS PAGE (When Data Entered)

19 REPORT DOCUMENTATION PAGE		READ INSTRUCTIONS BEFORE COMPLETING FORM	
1. REPORT NUMBER RADC-TR-77-145	2. GOVT ACCESSION NO.	3. RECIPIENT'S CATALOG NUMBER 9	
4. TITLE (and Subtitle) ADVANCED DIGITAL EXPLOITATION TECHNIQUES (ADET).		5. TYPE OF REPORT & PERIOD COVERED Final Technical Report.	
7. AUTHOR(s) George E. Forsen, John C. Lietz Dr. Frank H. Feng, Dennis J. Lucey Michael J. Gillotte, Dr. Mark R. Nelson Dr. Michael J. Zoracki		6. PERFORMING ORG. REPORT NUMBER PAR Report - 77-3	
8. PERFORMING ORGANIZATION NAME AND ADDRESS Pattern Analysis & Recognition Corporation 228 On the Mall Rome NY 13440		9. CONTRACT OR GRANT NUMBER(s) F30602-75-C-0141	
11. CONTROLLING OFFICE NAME AND ADDRESS Rome Air Development Center (IRRE) Griffiss AFB NY 13441		10. PROGRAM ELEMENT, PROJECT, TASK AREA & WORK UNIT NUMBERS 62702F 62441059	
14. MONITORING AGENCY NAME & ADDRESS (if different from Controlling Office) Same		12. REPORT DATE April 1977	
15. SECURITY CLASS. (of this report) UNCLASSIFIED		13. NUMBER OF PAGES 239	
16. DISTRIBUTION STATEMENT (of this Report) Approved for public release; distribution unlimited.			
17. DISTRIBUTION STATEMENT (of the abstract entered in Block 20, if different from Report) Same			
18. SUPPLEMENTARY NOTES RADC Project Engineer: Lt Gregory B. Pavlin (IRRE)			
19. KEY WORDS (Continue on reverse side if necessary and identify by block number) Automatic Terrain Classification      Semiautomatic Target Image Processing      Detection Multispectral Photography Image Feature Extraction Interactive Image Processing			
20. ABSTRACT (Continue on reverse side if necessary and identify by block number) This effort developed and tested certain digital techniques that are applicable to the problem of tactical target detection using multispectral aerial photography. In addition key algorithms were provided for the Digital Interactive Complex for Image Feature Extraction and Recognition (DICIFER) located at RADC.  Algorithms were designed and implemented to provide the capability for normalizing digitized image data. These include the following areas: → over			

DD FORM 1 JAN 73 1473

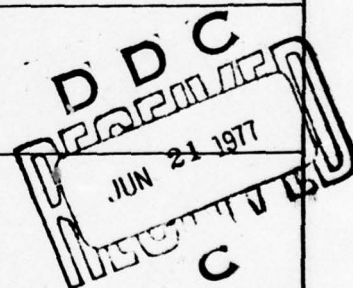
EDITION OF 1 NOV 65 IS OBSOLETE

UNCLASSIFIED

SECURITY CLASSIFICATION OF THIS PAGE (When Data Entered)

390 101

1B





UNCLASSIFIED

SECURITY CLASSIFICATION OF THIS PAGE(When Data Entered)

with  
→ radiometric and geometric corrections for the Computer Eye digitization device, point-spread function correction, and registration program embellishments. A general purpose image-combinations program was also provided.

A major task of this effort was the development of sensor/sun position and atmospheric correction programs.

Experimental efforts included the digitization of multispectral imagery and generation of ground truth data. Automatic classification logic was designed and tested on a limited data set. This logic was successful in separating camouflaged tactical targets from vegetative backgrounds.

↑

UNCLASSIFIED

SECURITY CLASSIFICATION OF THIS PAGE(When Data Entered)



## TABLE OF CONTENTS

<u>Section</u>	<u>Page</u>
1. Introduction and Summary .....	1-1
1.1. Background .....	1-1
1.2. Commentary .....	1-2
1.3. Summary of Results .....	1-4
1.3.1. Programming Effort .....	1-6
1.3.2. Experimental Effort .....	1-13
1.4. Conclusions and Recommendations .....	1-20
2. Background .....	2-1
2.1. The Reconnaissance Scene .....	2-1
2.1.1. The Reconnaissance Role .....	2-2
2.2. Physical Properties .....	2-3
2.2.1. Military Targets .....	2-3
2.2.2. Sources of Error .....	2-5
2.3. Current Methods .....	2-8
2.3.1. Cameras and Line Scanners .....	2-8
2.3.2. Photo Interpreter's Role .....	2-11
2.4. Manual Photo-Interpretation Techniques .....	2-13
2.4.1. The Cues Used .....	2-13
2.4.2. Identification and Mensuration .....	2-15
2.5. Technology Assessment .....	2-17
2.5.1. Assistance Vs. Replacement .....	2-17

# TABLE OF CONTENTS (Cont.)

<u>Section</u>		<u>Page</u>
3.	Atmospheric Modeling .....	3-1
3.1.	An Aerial Remote Sensing Model for Photographic Sensors .....	3-1
3.1.1.	Introduction .....	3-1
3.1.2.	Basic Remote Sensing Model .....	3-3
3.1.3.	Atmospheric Luminosity .....	3-23
3.1.4.	Astronomical and Geographical Factors .....	3-30
3.2.	Limitations of the Model .....	3-34
3.3.	Computer Program .....	3-37
3.4.	Tests on Atmospheric Correction Program .....	3-43
3.5.	Application to Digital Imagery .....	3-53
4.	Computer Eye Calibration .....	4-1
4.1.	EYECAL .....	4-1
4.1.1.	Purpose .....	4-1
4.1.2.	Operating Procedure .....	4-1
4.1.3.	Calibration Strategy .....	4-3
4.1.4.	Program Details .....	4-3
5.	Error Estimation and Removal in Multispectral Image Registration .....	5-1
5.1.	Cursor Control Error Estimation .....	5-2
5.2.	Intra-Band Point Transfer Error .....	5-5
5.2.1.	Experiment Design .....	5-6
5.2.3.	Experiment Procedure .....	5-9

## TABLE OF CONTENTS (Cont.)

<u>Section</u>	<u>Page</u>
5.3. Intra-Band Point Transfer Error .....	5-20
5.4. Removing Cursor Control Error and Intra-Band PT Error .	5-20
5.4.1. Correlation Formula Selection .....	5-24
5.4.2. Window Size Effect in Local Correlation Calculation .	5-26
5.5. Inter-Band Point Transfer Error Removal by Local Correlation .....	5-31
5.6. Conclusion .....	5-34
6. Special Programs for DICIFER .....	6-1
6.1. Correlation-Assisted Image Registration .....	6-1
6.2. Modify Design Vector File .....	6-3
6.3. Radiometric Image Calibration .....	6-5
6.4. Change Image Scale .....	6-6
6.5. Linear Image Restoration .....	6-7
6.6. Image Combinations .....	6-11
7. Pattern Recognition Experiments .....	7-1
7.1. Overview .....	7-1
7.2. Interactive Logic Design .....	7-1
7.2.1. Structure Analysis .....	7-4
7.2.2. Logic Tree .....	7-10
7.3. Logic Evaluation .....	7-19
Appendix A Blackbody Radiation	
Appendix B Calculation of Atmospheric Backscatter	
Appendix C Calculation of the Normalized Earth-Sun Distance	



## TABLE OF CONTENTS (Cont.)

### Section

Appendix D	Calculation of Solar Declination
Appendix E	Calculation of Solar Evaluation Angle
Appendix F	Classification Logic
Appendix G	Imagery Available for ADET Program
Appendix H	Table Showing Film Resolution
Appendix I	ADET - Site Information

# LIST OF FIGURES

<u>Figure</u>		<u>Page</u>
2-1	Reconnaissance Cycle . . . . .	2-4
3-1	Target Scene . . . . .	3-2
3-2	Example of Layered Atmosphere. . . . .	3-9
3-3a	Horizontal Coordinate System . . . . .	3-33
3-3b	Equatorial Coordinate System . . . . .	3-33
3-4	Program Structure. . . . .	3-39
3-5	Computed Values of Extinction as a Function of Air Mass for Several Wavelengths. . . . .	3-48
4-1	Calibration Reseau . . . . .	4-2
4-2	EYECAL Program Structure . . . . .	4-2
4-3	Apparent Positions of Fiducial Points and Corresponding Best-Fit Square Grid . . . . .	4-4
4-4	Grey Values in the Neighborhood of the Image of Fiducial Point K. . . . .	4-4
4-5	Steps of SEGB. . . . .	4-8
4-6	The Phase Vector $f_0$ and the Lattice Vectors $f_1$ and $f_2$ . . .	4-10
4-7a	Phase Error in Trial Vectors . . . . .	4-13
4-7b	Lattice Vector Error in Trial Vectors. . . . .	4-13
4-8	Points of Image. . . . .	4-19
4-9	The Points $\Delta w$ Used in the Interpolation to (I,J) . . . . .	4-22
5-1	Digital Images Used for Visual Intra-band PT Error Study .	5-7
6-1	Results of Deconvolution Process . . . . .	6-9
7-1	Four Band Photography over Stockbridge Test Site . . . . .	7-2
7-2	Band 1 Enlarged with Area 1 and Area 2 . . . . .	7-3

7-3	Histograms for Band 1 Samples. . . . .	7-5
7-4	Histograms for Band 2 Samples. . . . .	7-6
7-5	Histograms for Band 3 Samples. . . . .	7-7
7-6	Histograms for Band 4 Samples. . . . .	7-8
7-7	Optimal Discriminant Plane for Classes T and W Used for Restructuring T into Subclasses T and Q. . . . .	7-9
7-8	Logic Tree Showing Functional Description of the Hierarchical Classification Logic . . . . .	7-11
7-9	Node 0 Logic: Projection of Data to Illustrate Distribution of Samples with Respect to the Boolean Logic Statement . .	7-13
7-10	Node 2 Logic: Two-Space Eigenvector Projection of All Data at Node 2. . . . .	7-14
7-11	Node 3 Logic: Two-Space Eigenvector Projection of All Data at Node 3. . . . .	7-16
7-12	Node 5 Logic: Two-Space Eigenvector Project of All Data at Node 5 . . . . .	7-17
7-13	Two-Space Projection of Data at Node 4 . . . . .	7-18
7-14	Node 10 Logic: Two-Space Projection (Optimal Discriminant Plane) for All Data at Node 10 . . . . .	7-20
7-15	Decision Image for Area 1. . . . .	7-22
7-16	Decision Image for Area 2. . . . .	7-22



# LIST OF TABLES

<u>Table</u>		<u>Page</u>
2-1	Basic Characteristics of Aerial Imaging Sensors <sup>(3)</sup> Flown by RADC. . . . .	2-10
3-1	Subroutine Functions . . . . .	3-40
3-2	Computed Values of Solar Radiation Compared to Tabulated Values . . . . .	3-46
3-3	Computed Solar Elevation on 2Aug74 at 90° W and 40° N Compared to Values Computed by Hand from Solar Right Ascension and Declination on That Date . . . . .	3-47
3-4	The Scene Radiation (Arbitrary Units) Reaching the Camera For Latitude 53° at Various Times and Longitudes . . . . .	3-49
3-5	Fraction of Sunlight Reaching Target Scene . . . . .	3-50
3-6	Extinction in Magnitudes for Various Air Masses. . . . .	3-51
3-7	Comparison of Computed and Measured Extinction Coefficients. . . . .	3-52
5-1	Cursor/Control Error Estimation. . . . .	5-4
5-2	Euclidean Distance Error Summary( $e_{ij}$ ). . . . .	5-12
5-3	ANOVA Table for Intra-band Visual PT Error Analysis. . . . .	5-16
5-4	Intra-band Visual PT Error Estimation. . . . .	5-18
5-5	Recorded (Row, Column) Point Locations in Inter-Band PT Study. . . . .	5-21
5-6	Inter-Band Point Transfer Radial Error Estimation. . . . .	5-22
5-7	Unnormalized vs. Normalized Correlation in Machine Point Transfer (PT). . . . .	5-25
5-8a	Window Size Effect on Machine Point Transfer (PT) High Contrast Image Group . . . . .	5-27
5-8b	Window Size Effect on Machine Point Transfer (PT) Poor Contrast Image Group . . . . .	5-29

<u>Table</u>	<u>Page</u>
5-9 Window Size Effect to Machine Point Transfer (x: ratio of the highest correlation value to that of the second highest)	5-32
5-10 Intra-Band Error Removal By Local Correlation. . . . .	5-33
7-1 Assigned Classes (via Classification Logic). . . . .	7-21

## EVALUATION

This investigation was significant because it resulted in the development of a first-order capability to normalize the basic factors which degrade the information content of digitized photographic images (solar illumination, digitization, atmospheric, etc).

The software developed during this effort enhances the capability of the RADC Image Processing System. The analysis of digitized multi-spectral photography that was conducted during this effort was significant in that it provided a thorough exercise and demonstration of the capability of the RADC Image Processing System.

This effort directly supports the RADC TPO-2 objective to develop image exploitation techniques in support of intelligence requirements of various DOD agencies. Specifically, the significance of this study has direct relevance to the TPO-2 subtask objectives defined for photosensor exploitation and digital image exploitation techniques.



GREGORY B. PAVLIN, 1/Lt, USAF  
Project Engineer



## SECTION 1

### INTRODUCTION AND SUMMARY

#### 1.1. BACKGROUND

The Advanced Digital Exploitation Techniques (ADET) effort developed and tested certain digital techniques that may aid the Image Interpreter (I/I) in tactical target detection using multispectral aerial photography. In addition, it provided necessary additions to the Digital Interactive Complex for Image Feature Extraction and Recognition (DICIFER) located at Rome Air Development Center (RADC).

Section 2.1 provides the background context thought relevant at the beginning of this effort. The salient points are included as follows:

- o Data collection systems are improving in resolution, sensitivity, productivity and use of available spectral bands, thus creating a potential deluge of data and variety of image types.
- o Different sensor types create imagery requiring new interpretation skills in addition to those acquired with traditional single image, black/white, high resolution frame photography.
- o The increased mobility of targets having large threat capability demands substantially increased responsiveness by the reconnaissance

operation, and places a greater burden on tactical interpretation speed.

- o Exploitation techniques are still mostly film-oriented in spite of the growth of digital technology and the growing trend to transmit image data via cryptographic digital communications channels, and in spite of the large growth of digital image restoration, enhancement and pattern recognition techniques.
- o The I/I is burdened with "routine" tasks such as image and sensor quality assessment, cloud cover and mission plotting, data base updating and data dissemination. It has been estimated from an assessment of SEA operations that the I/I spends only 20% of his working time actually searching for and/or identifying areas of interest.
- o A wealth of information exists about collection systems, target types and signatures, degradation phenomena, operational requirements and potentially useful digital image processing techniques. However, the practicing I/I does not yet have the benefit of the appropriate fusion of these technologies to enhance the reconnaissance function.

#### 1.2. COMMENTARY

The current reconnaissance photo interpretation methodology is film-based. Film has large information storage capabilities relative to its cost.

It has a natural place in future schemes for archival storage and other functions which can tolerate the necessity to physically handle, transport and chemically process the medium.

Digital data streams from anticipated sensors, whether radars, FLIRs, multichannel DLIRs, etc., plus the responsiveness requirements for modern tactical scenarios are forcing the data to be processed, stored and displayed electronically. As more and more data is collected, encrypted and transmitted to the I/I stations, and as more and more of the I/I's output is digitized, fused with other data, encrypted and transmitted to other intelligence centers, the more natural it will be to use a completely digital system. Such systems will not only do the bookkeeping, report generation and mensuration calculations now performed, but also store, restore, enhance and manipulate the image data during the active period of interpreting the data.

The human's capacity to use his training skills, experience, knowledge, judgment and intuitive capabilities will not be replaced by mechanical means in the near future. His perceptual system far surpasses in its total function the capability of any present electro-optical "visual" system. He should be used in the total system in such a manner as to take best advantage of these attributes.

Human productivity and reliability are affected, however, by fatigue, distraction, emotional factors, etc. Thus, results, especially under conditions of stress, are not always predictable or repeatable. Furthermore, the



target cueing process requires screening voluminous amounts of imagery to find sometimes almost imperceptible indications of possible targets. In addition, numerous data management, mensuration and report generation duties can easily be performed digitally. Thus, there is strong motivation for investigating techniques that would enhance the operation of an all-electronic exploitation system in which computational algorithms and digital data manipulation play important roles in aiding the I/I.

Performing the more routine functions such as image screening, cloud cover and mission plotting as well as data base search, updating and product dissemination, would alleviate much of the present burden. Performing data normalization, i.e., image restoration and registration, image enhancement through the variety of methods already available, can provide visual displays which highlight the target type. A completely automatic target cueing system is obviously desirable. It has been the objective of this project to utilize digital processing techniques for obtaining significant progress towards achieving this goal.

### 1.3. SUMMARY OF RESULTS

ADET's first task was to review the many topics of investigation described in the proposal as relevant to digital exploitation of imagery and choose, with the agreement of RADC staff, those that would benefit RADC's long-term objectives in their reconnaissance technology mission. Because of the availability of multispectral photographic data of tactical targets of known ground truth, made available from prior efforts [1], we were directed

to concentrate on developing automatic exploitation techniques using these data. RADC has had considerable success in exploiting color aerophotography in unique situations [2]. Furthermore, there was considerable investment in the construction of DICIFER [3,4,5] and some experience already gained in its application to multispectral photography [5]. This latter effort showed certain inadequacies that had to be remedied before full advantage of the automatic classification power of DICIFER could be utilized. These had mostly to do with normalization and control of the input data. The objective of the selected tasks was, therefore, to complement the existing capabilities of DICIFER with particular normalization routines and make tactical target detection less susceptible to atmospheric, seasonal, geographic, and other variations.

The project effort was divided into two major parts, development and implementation, and experimental testing of certain image processing algorithms. These include the following:

- o Radiometric Correction of the Computer Eye
- o Geometric Correction of the Computer Eye
- o Point Spread Function Correction
- o Sensor/Sun Position and Atmospheric Correction
- o Registration Program Embellishments
- o General-Purpose Image Combinations

The experimental effort included:

- o Selection, scanning and registration of multispectral imagery
- o Collection of ground truth data
- o Testing of above algorithms
- o Classification of target scenes

A line item was added to the effort to develop terrain mapping techniques using B/W imagery. These thematic maps would be converted for use in radiometric correlation guidance systems. Thematic maps were obtained using automatic classification techniques available on DICIFER for low and high altitude B/W images of six scenes representative of target areas. This work has been reported in detail under separate cover [6].

#### 1.3.1. Programming Effort

##### 1.3.1.1. Computer Eye

The Computer Eye is a vidicon closed circuit TV raster scan camera plus an A/D convertor and digital interface logic. It allows an illuminated transparency or opaque copy to be scanned and digitized under computer control with the data stored directly in memory.

As is typical of most vidicon TV cameras, the device gain is not uniform across the image. Furthermore, these variations are a function of equipment adjustments, age, and subject to drift. Thus it is important to remove their



effects, perhaps as often as at the beginning of each scanning session. In addition, the light intensity of the illumination is not uniform. It is important that like scene categories having equal film densities be digitized the same no matter where they are on the film.

Though better than some CCTV vidicon cameras, the Computer Eye exhibits some S-curve distortion of the camera and potential for pincushion or barrel type distortion along the edges. Matching adjacent subimages is made easier when little or no geometric distortion remains after correction.

The purpose of the Computer Eye Radiometric Correction Program is to allow the Computer Eye to be used as a calibrated scanning densitometer. The method of calibration uses reference neutral density filters and compensates for both vidicon shading and light table variations. Several digitized calibration images are scanned using a small number of neutral density films having a sequency of known values spanning the range of densities in the set of images to be digitized and which are stored with the corresponding images. During normalization, the program interpolates between the two closest calibration values (one higher and one lower in value), and computes the corresponding density value at each pixel position. This program is available to DICIFER users. Details of the method can be found in Section 6.3.

The purpose of the Computer Eye Geometric Correction Program is to compensate for the geometric distortion introduced by the nonlinear scan/sampling pattern of the Computer Eye. The program uses data obtained by scanning a calibration grid. An interpolation technique is used. The

program was written in FORTRAN IV and runs on a PDP 11/45. Tape conversion programs exist to allow imagery obtained on DICIFER's Computer Eye to be corrected. Details of the method can be found in Section 5.

#### 1.3.1.2. Super-Resolution

The point spread function (PSF) of an imaging device like the Computer Eye or a reconnaissance camera is the two-dimensional spatial equivalent to the linear circuit impulse response. By deconvolving the circuit's output with its impulse response, the unfiltered input waveform can be obtained. Similarly in the linear, space invariant, model of an imaging device, the input image can be obtained by deconvolution techniques from the sensed output and the PSF. Because the degradation associated with finite PSF's is a blurring effect, the process of compensating for the device's PSF is known as "super-resolution".

Because of the existence of fast Fourier transform techniques and the equivalence between convolution in the spatial (image) domain and (complex) multiplication in the frequency (transform) domain, Fourier techniques have been suggested. However, the assumptions of linearity and space invariance do not necessarily hold. Plus the inversion of large matrices can pose a problem. Thus, other approximate techniques are used. Rather than develop an algorithm from scratch, we chose to obtain an existing deconvolution program, albeit for one dimension only [8], written by Peter Janssen [see also reference 9]. This program written in 1108 FORTRAN was modified to run

in two dimensions on the PDP 11/45 under RSX-11 in FORTRAN IV-Plus. Details of this task can be found in Section 6.5.

#### 1.3.1.3. Atmospheric Model

The major task of this project turned out to be the Sensor/Sun Position and Atmospheric Correction program described in Section 3. Sun angle has been found to be a major cause in the variation of remotely spaced, multi-spectral data [5]. To use classification logic on imagery sets differing in geographic location and time of flight, but based on reflected intensities of only one scene, it was thought useful to compensate for the effects of solar elevation, sensor altitude and first-order atmospheric effects.

The algorithm assumes vertical photography and the usual camera field of view. The tabular data for scattering and absorption assumed clear weather. Also assumed is a flat Lambertian surface. It was originally thought these assumptions would be adequate for the photography to be used in this effort. The program is quite general, though, and could account for haze and other particulates with the appropriate data entered into its tables. These data would, however, be difficult to obtain for the usual recce mission.

The program calculates the following expression:

$$G_S = G_{TAT_{TS}} + D_{TS}$$

where  $G_S$  is the irradiance at the sensor in watts per square meter,



$G_T$  is the irradiance of the target area and is caused by two sources, direct and indirect sky radiance,

$A_T$  is the target albedo and is assumed to have a reflectance-value of unity,

$T_{TS}$  is the transmission attenuation from the target scene to the sensor, and

$D_{TS}$  is the indirect irradiance at the sensor due to "path radiance" of the volume of atmosphere in the solid acceptance angle defined by the sensor field of view.

The program assumes a layered atmosphere as this is convenient not only for calculations but also for available tabular data obtained by measurements. The data is a strong function of wavelength. If it were not, simple ratios between multispectral band intensity values would normalize most sun angle and atmospheric variations. In particular, the path radiance term,  $D_{TS}$ , increases much faster in the blue wavelengths than for other wavelengths as sensor altitude is increased. This is separate from but similar to the so-called haze effect in which Mie scattering from water droplets can make high altitude blue-sensitive recce imagery useless. The program also assumes uniform filter response for each frequency band of the data. However, the tabular data divides the total range into many bands allowing the assumption to hold for all but the narrowest of hard-pass/rejection filters. The filters

used for the SDC camera posed no problem in this respect. Details of the sun-sensor-atmosphere normalization method are found in Section 3 and Appendices A through E.

#### 1.3.1.4. Multiple Image Registration

The SDC camera produces four separate film images that must be separately scanned. Because no indexing marks are available and because the images cover slightly displaced areas on the ground, post-scanning registration must be performed. In a previous effort using Landsat imagery [5] narrow features would sometimes have only one-pixel width. When necessary to use data from more than one spectral band to correctly classify these narrow features, it was necessary to precisely register the images so that each point in the scene would have the same coordinate values in the images for all bands used for that scene. Edges of objects should line up in each image, particularly when small and the number of boundary pixels is of the same order as the number of interior pixels. Unfortunately, for all but the lowest altitude imagery used, the tactical target sizes were such that precise registration was critical.

To further enhance the registration capabilities already on DICIFER, the registration routine was embellished with the capability to perform a cross-correlation between designated subimages. The procedure for use would be as follows: control points would be selected as usual and a gross registration performed. This insures that small areas around the control points for each spectral image have insignificant rotation with respect to each other. The

cross-correlation function of image pairs is then computed as a function of vertical and horizontal displacements from the control point location. Assuming grey-tone correspondence in most of the subimage, the cross-correlation function will peak when the subimages are precisely aligned; thus providing a correction displacement to the hand-picked control point locations. When grey-tones do not correspond, edge gradient locations were assumed useful for correlation purposes. Further details on the method can be found in Section 6.1. The embellished registration routine is now available to DICIFER users.

#### 1.3.1.5. Multiple Image Combinations

Rather than modify the general-purpose search routine on DICIFER to work with multispectral image sets in addition to its single-image capability, it was decided to develop and implement a multi-image combination's routine. For this program, a compiler for a rudimentary high-level language was written. It allows the user to specify the instructions that the program uses to combine the images. Images are combined on a pixel-by-pixel basis. All arithmetic and logical operations are allowed, plus functions such as log and exponentiation. Floating or fixed point arithmetic can be specified for each operation.

The instruction sequence or "program" consists of a list of IF-DO statements. At each pixel, the program is executed in the order of the statements. If the data satisfy the predicate of an IF clause, then the corresponding DO clause is performed to compute the corresponding pixel of the new combined



image. The next pixel is then tested and the appropriate computation performed for it. Full word and double word precision is used in fixed and floating point operations, respectively. If a given IF clause is not satisfied, the default DO statement is exercised. This general routine supersedes certain specialized routines on DICIFER that worked only with pairs of images and performed only specific mathematical operations such as average and difference. More details of the Image Combination Program can be found in Section 6.6. It has been installed and is now operational on DICIFER.

In addition to the above major routines and additions to DICIFER, other programs that only had user program status, plus some minor routines and changes to existing routines, were also added to the system. The current status should be reflected in the updated user's manual presently in preparation.

#### 1.3.2. Experimental Effort

All routines were tested to show that they worked according to their external specifications, i.e., their functional design. Their ultimate utility can be verified only under extensive experimentation. The initial experience here was limited due to several complicating factors, including malfunctioning peripheral equipment and uncontrollable environmental conditions which could not be remedied at that time. However, some insight was obtained as to their applicability to their intended purpose of aiding digital exploitation of multispectral imagery.

#### 1.3.2.1. Data Set

Multispectral reconnaissance imagery had been previously obtained on several missions flown at various days and times of day in 1973-74 over the Stockbridge, Floyd and other NETA\* test sites. Mostly clear weather conditions prevailed and imagery was obtained at several altitudes using two different sets of filters. One set, designated T1, had been chosen to maximize the color contrast of military targets in natural backgrounds. The other set, designated P1, had been chosen to normalize the color signature of all vegetation. Several sets of four-band imagery were chosen because they contained military targets, ground truth could be readily obtained, and a variety of times of day and dates were available. Further details, including ground truth maps can be obtained in Appendix I.

Positive transparencies were obtained as first generation copies from the originals. No attempt was made to balance the density ranges for the separate bands because digital processing does not require the same control as does electro-optic techniques [7]. However the use of density wedges in development of the original films and of the copies is necessary to achieve absolute normalization.

---

\* NETA is the Northeast Test Area which is comprised of a number of well documented industrial and military sites.

Resolution estimates were made by RADC Data Base personnel using standard P/I techniques on the Floyd test site scene that contained a bar-type chart. Unfortunately, one band showed rather poor focus and because no motion compensation was used during these missions, the overall film resolution was somewhat disappointing, especially in the direction of flight. The linepairs per mm ranged from 4.94 to 9.96. See the table in Appendix H for details.\*

The purpose of the resolution tests were to provide a rationale for choosing a reasonable sample spacing used during scanning. The criteria was based on the dual objectives to make the scanning and digitization as transparent as possible and at the same time minimize the number of samples necessary to cover scenes of interest. A spacing of 25.6 points per mm was chosen for scanning, using the Computer Eye.

The Computer Eye failed midway through the scanning effort, an immediate return to service was not possible. Fortunately, but not without some additional effort, a different scanner was available - the Laser Input Processing System (LIPS). A 20 micron spacing between samples was used on LIPS. RADC personnel participated in the LIPS scanning effort. Ten frames were scanned. Each frame was divided into four subframes. Four spectral bands for each subframe were scanned producing a total of 160 digitized images. Each such image contained 1024 x 1024 pixels. The density scale on LIPS is from zero to 2.56 and is quantized into 256 equal levels.

\* An interesting phenomenon occurred when comparing the apparent resolution of the original negative and that of the positive duplicate transparencies. The perceived resolution was observed better on the copy. An explanation for this is that the copy also exhibited more contrast, thus enhancing the apparent resolution. Perhaps this suggests the utility of mechanical and objective resolution tests that can make resolution measurements independent of contrast.



A necessary but often labor-intensive task in the development of automatic classification logic is the careful determination of ground truth data. Ground truth data was supplied by Rome Research Corporation personnel who were familiar with the test sites. Boundaries of regions of specific surface materials likely to have unique multispectral signatures are shown in Appendix I. Also shown are the location and identification of specific targets at the Stockbridge site. These targets include several tanks and 3/4-ton trucks plus one with unique camouflaging, an assortment of other military vehicles, a mock SAM site, artillery and mortar emplacements.

#### 1.3.2.2. Computer Eye

The algorithm testing for radiometric and geometric was performed first to determine that the programs function according to specifications. Equally important is their utility in their intended application. As mentioned above, conclusions cannot be made based on the limited experimentation made on this effort. The following comments must, therefore, be treated as indications only.

Enough experience was gained with both the radiometric and geometric correction routines to be confident in the methods used, their implementation and their utility. Considerable shading and geometric distortion was discovered and corrected by these routines. Sections 5 and 6 gives the details. Had the Computer Eye been used throughout the scanning of the total set of images, it would have been imperative that these correction routines be used. These adjustments make the Computer Eye, which is already convenient to use

and operates on-line, almost equivalent to a fast (low-resolution) scanning microdensitometer.

#### 1.3.2.3. Super-Resolution

The deconvolution program showed encouraging performance on the data set supplied with it. It did, however, under some values of program control parameters, exhibit oscillatory behavior and was not particularly quick to converge, both in number of iterations and actual computer time on the 11/45. These characteristics were especially pronounced during experiments using two-dimensional data.

#### 1.3.2.4. Atmospheric Model

The sensor-sun position and atmosphere correction program was checked against known extinction measurement at various wavelengths, sunrise and sunset tables and other data. The current version shows close agreement with these data. This program computes an irradiance value at the sensor aperture as a function of wavelength, which is the sum of two terms. Although each term is computed explicitly, there is only one sensed value, i.e., the original film density value at each pixel. In the linear portion of the exposure-density curve, for a given pixel in the image,

$$d = d_0 + \gamma \log E$$

where  $E$  is the incident light intensity times the exposure,

$\gamma$  is the proportionality factor, and

$d_0$  is the background density (fog) level of the film.

If the relationship between the irradiance of the camera objective lens and the film exposure,  $\gamma$  and  $d_0$  were known, the absolute reflectance values of the surface material could be computed directly. The values of  $d_0$  and  $\gamma$  can be obtained if a step wedge calibration is applied before film development.

This effort did not include sensor/film modelling; thus the necessary relationship is not known. Furthermore, the additional processing involved in the generation of the copy transparency and the scanning thereof introduce more factors between the sensor irradiance values and the number output by the scanner. It is conjectured, however, that the relationship has only two degrees of freedom when the above linear log exposure-density relationship holds for both films. If true, and if the same scene were viewed on the same roll of film, for example, at two altitudes, a set of two simultaneous equations could be solved for the absolute ground surface reflectances. An alternate approach is to identify one surface material of known reflectance to calibrate each frame. However, this precludes automatic generalization of classification logic until such calibration is made.

#### 1.3.2.5. Multiple Image Registration

Controlled experiments were performed to determine the accuracy of manual selection of control points used for image registration. This set of



experiments was carefully planned and executed and the results can be regarded as reliable.

1. Cursor Control Error was estimated to be 0.46 pixel in the vertical and 0.58 pixel in the horizontal direction in the center part of the monitor screen.
2. Intra-band visual point transfer error depends on the relative orientation between images to be registered. The median radial error was estimated between 1.11 and 1.22 pixels for relative orientation less than  $10^\circ$ .
3. Inter-band visual point transfer error increases as the band difference increases. The median radial error between the blue band and IR band was estimated to be between 2.26 and 2.98 pixels.

The use of the automatic correlation

1. Can eliminate cursor control and intra-band visual point transfer error.
2. Can reduce inter-band visual print transfer error between visible bands.
3. Cannot reduce inter-band visual print transfer error between visible bands and IR bands without suitable preprocessing.

Details of this effort in which both PAR and RADC personnel participated can be found in Section 5.

#### 1.3.2.6. Classification Logic

Initial classification logic experiments were attempted just prior to the end of this effort. The data from the T1 filters exhibited some difficulty in distinguishing between some vegetation and soil, as expected, but also between the tank camouflage paint and grassy tracks. In this respect only two of the four bands contributed to target discrimination, the most useful being the near-infrared band. The mission altitudes, focal length, and limited resolution of the camera combined to make very few target pixels available for training the classifier logic. Lower altitude data, using T1 filters, was available and did provide an adequate sample. Very good classification accuracy of several ground surface categories, including the targets, was obtained within the frame. One 3/4-ton truck, however, was difficult to isolate. Its data consistently fell close to a certain type of vegetation no matter what transformation was made on it. Upon further examination of ground truth information it was discovered that additional camouflage netting had been placed over this target at the time of flight. Details of these efforts are in Section 7.

#### 1.4. CONCLUSIONS AND RECOMMENDATIONS

The DICIFER system was used to correctly detect most tactical targets in a section of the Stockbridge test site using digitized four-band multispectral

photography with pre-selected narrow band filters, where the training and testing data came from the same frame.

Normalization algorithms were developed and implemented in the form of digital computer programs to allow generalization of classification logic from one frame to another in time and space. The individual routines which accounted for sun angle and atmospheric factors, and scanner characteristics performed as expected.

Additional routines that model the camera and film development are required to obtain absolute surface material reflectivity values. Negligible shadow detail is available for high altitude, high sun-angle imagery used, preventing self-normalizing techniques like SCAT from working. The clear weather data used in the atmospheric model did not account for the degree of path radiance observed in the T1 filter data because of haze at the time of flight.

Specific recommendations, therefore, are that algorithms that model camera, film development and scanner functions be implemented so that a direct correspondence can be made between the digitized imagery and the ground surface reflectivity. This would complete the underlying approach that was the basis of this effort, i.e., to account for all the known variables before attempting target detection logic design. Until this is done it cannot be determined whether this approach of normalizing to absolute reflectivity values is viable. In the absence of these algorithms, certain alternative approaches may be tried. For example, the use of one (or more) known



reflectivities can possibly normalize the remainder of each new frame even though the camera/film/scanner relationships are not known explicitly. A combination of the sun-sensor position and atmospheric model with the SCAT approach that requires no a priori knowledge of time of day or day of the year, or filter characteristics used (but also requires the presence of shadows) should also be investigated.

Also recommended is a review of the expected role of multispectral film data in future tactical reconnaissance situations, especially in view of other modern sensors that have all-weather, stand-off and quick data-availability capabilities.

## SECTION 2

### BACKGROUND

#### 2.1. THE RECONNAISSANCE SCENE

Beginning with the first recorded use of aerial photography as a practical source of reconnaissance in the early days of World War I, it was found that photo interpreters could predict the movement of the enemy and otherwise disclose his intentions in time for counteroffensives to be planned. The aerial hand-held graflex cameras were capable of providing vast amounts of military information despite attempts to deceive it by use of camouflage materials, decoys and other deceptive devices. By 1918, reports indicate that over 10,000 photographs were being developed and printed by the French each day during periods of intense activity.

In recent years, pictures from space have paved the way for our exploration to distant planets, as evidenced by the far-reaching remote sensing effort accomplished during Explorer's "close-in" reconnaissance of Jupiter. The enormity of the technological accomplishments which could lead from the Meuse - Argonne line of WWI to the Red Spot of Jupiter is indeed awesome. Yet while we exercise satellite systems such as the NASA Earth Resources Technology Satellite (ERTS), one of whose imaging sensors generates images with 4000-line TV resolution, and which produces and handles data at the rate of 10 million bits per second, we are still in need of substantive improvements to the military reconnaissance cycle where continued advancements in space and

aircraft sensor subsystems threaten to completely overwhelm the total system's capability to store, transmit, process and exploit the available sensor data in a responsive manner.

2.1.1. The Reconnaissance Role

Whether by satellite, or aircraft, or remotely piloted vehicles; whether during periods of hostility or in times of peace; the primary role of military reconnaissance is to produce and disseminate timely information about an area, event or target. A reconnaissance information center must respond to requests from a large number of defense and government agencies for specific types of coverage of specific areas for a variety of purposes. Both imagery hardcopy and written reports are generated and transmitted/delivered in response to such requests. Sources of data that affect reconnaissance mission planning include record of past flights and evaluation of previous results (if available), inventory of available collection systems and space platforms, specific satellite data, weather data and ancillary activity (intelligence) reports (when supplied). The manner in which reconnaissance is performed will also vary tremendously depending upon the nature and intensity of the conflict, and the extent of our military or diplomatic involvement.

Even though there are many variables affecting each situation, the main ingredient which remains common for all is the need for responsiveness within the reconnaissance system. Thus, while, during the conflict in Viet Nam, we witnessed the continued introduction of improved collection systems such as the high resolution, wide field of view, optical bar panoramic camera and



improved resolution and sensitivity characteristic in passive infrared line scanning systems, and accelerated film processing capabilities (owing primarily to the implementation and skilled operation of improved Versamat black-and-white and color processes); there was little if any advance to the rudimentary pre-Viet Nam film handling and exploitation processes. Figure 2-1 illustrates the results of one of the many reviews which highlights the problem. The flow times indicate that a total of three (3) hours 20 minutes was required to produce an interpretation report on a routine mission request. The photo interpretation effort accounted for approximately 40% of this time with less than half of that time (~ 40 minutes) actually spent on interpreting the film. The balance of the PI time was spent in performing non-exploration duties such as checking film for evidence of sensor malfunction, determining the image quality and amount of cloud cover, and plotting the film [10].

## 2.2. PHYSICAL PROPERTIES

### 2.2.1. Military Targets

The objective of the effort encompassed developing cueing algorithms which can be used to discriminate camouflage targets successfully. The major problem which surfaces when considering conventional film exploitation is the overwhelming amount of data which is traditionally collected in hopes that an interpreter may successfully extract some useful targetting information. Regrettably, as repeatedly evidenced by conventional reconnaissance/interpretation operations in Vietnam, the interpreter is confronted with too much

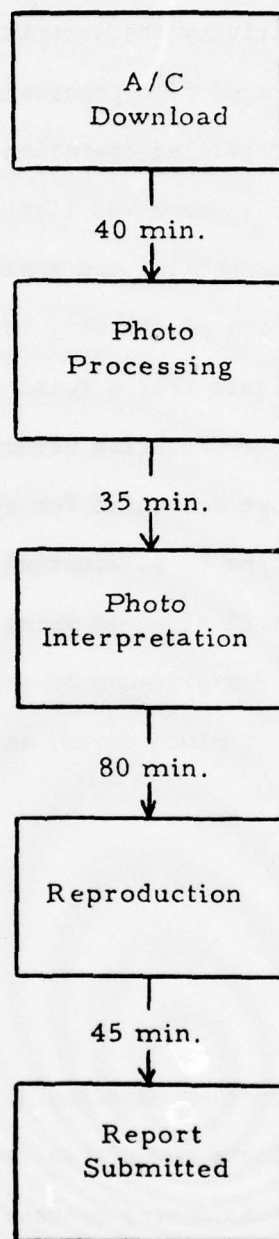


Figure 2-1 Reconnaissance Cycle -- Average Time  
Based On Priority II (Routine) Mission 460 TRW

data and too few cueing techniques to satisfy the need for rapid identification and response against highly mobile, deceptively camouflaged, high-payoff targets.

The successes of systems like Gunship employing electro-optical viewers to cue on targets for near-real time supply line interdiction suggest that more emphasis must be directed at dealing with systems and techniques that can maximize detection rates within acceptable weapons-response envelopes. A necessary and vital first step toward achieving this capability is represented by the objective of developing effective cueing techniques.

#### 2.2.2. Sources of Error

The mere listing of the sources of error that influence the target cueing and recognition task would occupy considerable space itself. The radiation which is reflected or emitted by an object and recorded by a sensing device is a function of many variables. These were grouped under the headings of sensor, and environment. Sensor variants depend on the sensor type, mode of operation, lens/film/filter set(s), detector, field of view, scale, format, recording technique. These and other variants interact to influence the energy received by the system and the manner in which it is recorded or displayed.

Environmental variables include, in part, the situation within which a system must operate and survive, including the geographic area, the intensity and nature of the conflict. Following on this are the factors influencing



the flight envelope such as sensor V/H, altitude and depression angle. Ground parameters include the type, number and location of targets, and the foliage camouflage and background conditions.

Other environmental parameters include time-over-target, weather and scene illumination. These factors weigh heavily on the appearance of targets as evidenced by the tonal shifting caused by diurnal effects on infrared imagery, and the diurnal and seasonal effects of sun angle on target/scene density in various visible bands.

In addition to these general influences, atmospheric effects add to influencing the apparent reflectance of a target. Changes in atmospheric conditions result in variation in sunlight and sky light distribution and yield apparent reflectance changes due to the consequent transformation of the spectral character of the incident radiation. The signal received through this atmospheric channel is given by:

$$I_s(\lambda, p_s) = I_o(\lambda, p_o) \tau_2(\lambda, p_t) + I_{PR}(\lambda, p_{PR})$$

where

$\lambda$  = wavelength  
 $p_x$  = those parameters which determine the value of the function

$I_s$	=	radiance at the sensor
$I_o$	=	radiance at the scene
$\tau_2$	=	transmittance of the atmosphere along the scene to sensor path
$I_{PR}$	=	path radiance at the sensor

This equation is the basis for all atmospheric models. However, the form of  $p_x$ ,  $I_o$ ,  $I_{PR}$ , and  $\tau_2$  are dependent upon the particular sensor system that is employed.

Consider  $I_o(\lambda)$ , the radiance at the scene. For active systems such as radar and microwave systems,  $I_o(\lambda)$  is dependent upon the power and configuration of the particular equipment used, upon the atmospheric transmission from source to scene and upon the reflectivity of the scene. For an emissive IR sensor system,  $I_o(\lambda)$  is simply dependent upon the absolute temperature and emissive characteristics of the scene. For normal aerial photography,  $I_o(\lambda)$  is dependent upon the reflectivity of the scene, the brightness of the sun, the sun angle, the sun-to-scene atmospheric transmittance, and the atmospheric illumination. The other terms,  $I_{PR}$  and  $\tau_2$  are likewise dependent upon the particular sensor system.

The radiometric error introduced by the atmosphere consists of attenuation due to  $\tau_2$ , noise introduced by  $I_{PR}$ , and possible changes in  $I_o$ . The problem consists not of this absolute error, but rather the changes in this absolute error due to changes in  $\tau_2$ ,  $I_{PR}$ , and  $I_o$ .

Atmospheric changes in temperature, pressure and composition (molecular and particular) alter the scattering and absorption properties of the atmosphere. Changes in these properties alter  $\tau_2$ ,  $I_{PR}$  and  $I_o$ .

Effects of the sensor, environment (atmosphere) and target must be removed from the measurement process to obtain accurate estimates of spectral reflectance.

### 2.3. CURRENT METHODS

#### 2.3.1. Cameras and Line Scanners

The major source of reconnaissance information is the high resolution optical camera which records a wealth of detail either in the form of different shades of grey on black-and-white (B/W) aerial film, or the chromaticity of each small area as recorded on color film. Because optical framing cameras play such a major role in tactical aerial reconnaissance, it is fortunate that RADC operates and maintains several different framing cameras as part of the reconnaissance flight-test operation.



The mode of operation of the framing camera is relatively simple. Exposure of the film is accomplished while the film is stationary or moving at an image motion compensation (IMC) rate. After each exposure sequence the film is transported to move an unexposed portion into correct position for exposure. Basic characteristics of these cameras are lens speed, focal length, range of shutter speeds and format or film size.

Besides the conventional single lens framing cameras, the multispectral camera systems available at RADC each have the capability to record the same scene simultaneously in several different regions of the visible and near infrared spectrum. The four-lens Hasselblad configuration and the 9-lens K-22 system have each been used to collect imagery over NETA sites. Other sources of multispectral photography are the 4-lens Spectral Data system which had been flown extensively over the Northeast Test Area during 1973-74, and 11-channel multispectral data, in analog tape format, collected over local targets from late 1972 through the summer of 1973 by a Daedalus multispectral line scanner. As yet, multispectral cameras and scanners are not used as operational sensing devices by the services, although their potential for narrowband sampling and the use of this data to obtain unique characteristics for militarily significant target/background scenes remains an attractive adjunct to the conventional optical camera. The Spectral Data system imagery was the primary subject of experimentation during this effort.

Table 2-1 contains a listing of the characteristics of several camera and line scan sensors available at RADC.

Type Camera	Designation	Format	Focal Length	Resolution l/mm	Angular Coverage
Vertical	RC-8	9" x 9"	6"	33 Plus X	73°44' x 73°44'
	KC-1B	9" x 9"	6"	20 Plus X	73°44' x 73°44'
	KS-87	4.5" x 4.5"	3"	45 Plus X	73°44' x 73°44'
	White	9" x 9"	6"	60 Plus X	41°06' x 41°06'
			12"	40 Plus X	21°14' x 21°14'
			6"	--	--
				Spectral Bands	
Multispectral	Hasselblad	70mm x 70mm	3"	4	20° x 37°
	Spectral Data	55mm x 105mm	6"	4	
	9-Lens (K-22)	70mm x 70mm	6"	9	
Infrared Line Scanner	MAIRS	5" Strip	2" EFL	1	90°

Table 2-1 Basic Characteristics of Aerial Imaging Sensors  
Flown by RADC

### 2.3.2. Photo Interpreter's Role

In an operational situation and in the training activities of tactical reconnaissance units in times of peace, the classic role of the image interpreter has remained basically unchanged, although his field has broadened and become more complex since the advent and usage of systems other than optical cameras. The interpreter serves as the vital link in the intelligence system between the raw data (sensor imagery) and the finished product (image interpretation reports).

The skilled image interpreter (I/I) combines prior knowledge about an area and target classes, logical constraints and contextual and ancillary data to extract information of strategic or tactical importance from sensor imagery. The skill of the I/I reflects years of specific training and experience often enhanced by specialization by target class and/or geographic region.

A capable interpreter must have some knowledge of mathematics as he is frequently required to make accurate measurements and computations from sensor imagery. The calculations become somewhat complex when working with oblique and panoramic photography, unrectified line sensor imagery, and radar imagery. The interpreter should be familiar with the basics of film processing inasmuch as he is usually the first person to critically examine processed film and can identify and report defects due to processing errors or equipment failures. In order to perform detailed work, the interpreter is required to



be familiar with many subjects including the enemy force's air, ground and naval order of battle, industries, processing and manufacturing techniques and transportation systems.

Because he is requested to prepare special reports on subjects as diverse as raw material mining and processing, chemical refining and production, soils and trafficability studies to name but a few, special training and experience in these areas are also required.

With the introduction of side-looking radar and line scan infrared sensors, interpreters should be knowledgeable in the physical sciences to better understand the various sensor, natural and man-made target interaction, and atmospheric effects which are responsible for the way target images appear on film and display.

It is clear that the I/I's tasks are becoming more complex. He is becoming inundated with imagery of different kinds in which the traditional behavioral cues are no longer valid. The desired response times are being shortened due to increased mobility of targets. Digital image processing techniques have the potential for enhancing the performance of certain tasks. Thus, it is anticipated that digital exploitation techniques will be utilized in future specialized interpretation systems.

## 2.4. MANUAL PHOTO-INTERPRETATION TECHNIQUES

### 2.4.1. The Cues Used

Before proceeding further, it may be instructive to briefly review some of the accepted conventions governing the image interpretation process. While there is still no universally acceptable analysis of the factors which affect the interpretability of an aerial image, several are worth noting. First, the features commonly used to establish target identity will be discussed.

#### o Size

The size of objects represents one of the major clues to identification. Errors in identification are frequently avoided by measuring objects on photography of a known scale. In addition to two-dimensional length and width measurements, parallax measurements and shadow measurements are frequently employed to determine the height of objects or simply to determine the apparent height or depth of an object.

#### o Shape

Planar views of objects, as observed on vertical photography, can serve as an important indication as to their structure, composition and function. The shape of an aircraft, for example, distinguishes

it with considerable certainty from other objects and can furthermore be used to characterize various types of aircraft.

o Tonal Contrast

Tonal contrast refers to the differences in brightness between an object and its background which, on black-and-white photographs, is manifested as levels of grey. The extent to which tonal contrast can be optimized depends on several factors such as the spectral reflectance characteristics of the object and its background, the transmission characteristics of filters, the spectral sensitivity of the recording film, and atmospheric scattering. Multispectral photography attempts to capitalize on the control which can be exerted by the judicious selection of film/filter combinations to sample reflected light in narrow spectral bands. Moreover, various atmospheric absorption models have been developed to account for the effects of light-scattering which degrade the tonal contrast of an image. Gradual changes in tonal values provide valuable clues leading to the interpretability and discrimination of soil types, vegetation classes and numerous other properties where gradual variations are important stimuli.

o Acutance

Abrupt edge gradients, or acutance, is a factor derived from density gradients and refers to the abruptness (or distance) over which



the tone contrast appears to occur on the image. This apparent sharpness characteristic is measured in terms of the resolving power of the collection system and is governed by several factors. These include aberrations of the lens system, focus of the lens system, image motion at the time of exposure, as well as the characteristics of the film and development process. Line scanners have their own set of edge-smearing effects. Edge detection is important because man-made objects tend to have well-defined boundaries leading to the visualization of recognizable shapes.

- o Texture

Texture is yet another quality of an image which can provide visual clues to target detection. It is created by tonal repetitions in groups of objects which are too small to be individually discerned. For example, the leaves or needles of trees may not be discernable separately, but contribute to the texture of the individual tree crowns on large-scale imagery; whereas on small-scale imagery the texture created by the large stands of trees can contribute to the identity of the species. Cultural features generally have different texture than natural features.

#### 2.4.2. Identification and Mensuration

As referenced earlier, interpreters are frequently called upon to make specific identifications of various targets detected on reconnaissance

imagery. One of the techniques used to achieve this level of interpretation with satisfactory confidence is to perform mensuration on the target or some component of a target complex. In other cases, such as the case of a cluttered target environment, the size of a target, its dimensions, surface area or volume, are some of the most useful cues available for eliminating many possibilities from consideration. Sometimes these measurements are no more than rough approximations of length-width ratios, an accepted cue to differentiate between tracked and wheeled vehicles. On the other extreme, interpreters confronted with high resolution, small-scale vertical photography over foreign military installations must obtain highly accurate measurements on relatively small target surfaces to ascertain the identity of the target or to confirm alterations to known target characteristics. In this latter example, the imagery is measured with the aid of light tables and viewers equipped with high quality optics and precision mensuration devices such as found on mono and stereo comparators.

One major problem encountered when attempting to perform image measurements is the need for working with an image with good tonal contrast and acutance. Thus, image processing routines which reduce system and atmospheric degradation and enhance contrast and edges on selected targets will conceivably result in an image upon which more accurate measurements can be achieved.

## 2.5. TECHNOLOGY ASSESSMENT

### 2.5.1. Assistance Vs. Replacement

The human visual system's capacity to perceive is impressive, especially when compared to attempts to mechanize vision. Even the eye as a sensor is a marvel of engineering. The image interpreter relies on his vision, training, experience, and general and specialized knowledge to detect, recognize, locate, describe and report on targets of national importance as recorded on film and/or displayed from a memory file. It is doubtful whether any one system could include all the skills, training, heuristic techniques and knowledge that the I/I possesses. Even so, the usual human limitations of fatigue, boredom and emotional state can sometimes affect the quality and consistency of results.

Although the human visual system can detect small differences in juxtaposed grey levels and object size, and can adapt to a wide range of illumination and scale, it is not suited by itself for precise measurement and memory of absolute grey scale, length or location. Even though the eye is quick to locate even subtle changes which may indicate the presence or absence of an object of interest, it has to be directed in a thorough and methodical search, a task influenced by the above-mentioned human factors. Although the search is often narrowed by a combination of external directives, good judgment, the recognition of analogous situations, and the human ability to predict, there remains the fact that such heuristics tend to trade accuracy for timeliness.



For the above reasons, and others, it has been suggested for as many years as there has been interest in computers and pattern recognition that the techniques of these disciplines be applied to the automation of certain of the photo-interpreter functions. However, as is usual, prophecy outpaces accomplishment. Past support of the many efforts to automate the I/I function have achieved a realization that computers compute and interpreters interpret. In other words, their skills are complementary rather than interchangeable.

The notion of semiautomated photo-interpretation is therefore a more plausible goal, especially in an interactive environment in which the computer system aids the I/I and vice versa, so that together a more accurate, productive and efficient I/I function can be performed.

Sensibly, the emphasis of this effort has been placed on image restoration and enhancement, i.e., the ability of a computer to transform a set of images, using a combination of selected algorithms, to another set of images - highlighting areas of potential interest and subduing those of no interest. A human can quickly assess the "quality" of the resulting transformations and select the combination most suited to the application.

SECTION 3  
ATMOSPHERIC MODELING

3.1. AN AERIAL REMOTE SENSING MODEL FOR PHOTOGRAPHIC SENSORS

3.1.1. Introduction

The aerial remote sensing of a ground scene has a great number of variables which determine the type and quality of information received by the sensor. This remote sensing model has been developed to describe the conditions during a clear weather aerial photographic reconnaissance mission.\* This model has as its objective the description of the irradiation at the camera lens aperture in terms of known and presumed parameters.

The restriction of the sensor to photographic cameras limits (or fixes) several variables. First, the wavelength of the radiation detectable by such type of photographic sensor is limited to the visible and near infrared radiation. The specific wavelength range used in this model runs from  $.38 \mu$  to  $1.00 \mu$ . Secondly, the source of the detected electromagnetic radiation is also fixed to be reflected solar irradiation. These two variables, the source and range of the electromagnetic radiation, determine the basic form of the aerial remote sensing model. (See Figure 3-1)

---

\* Most of the technical data and the mathematical formulations of the model developed were obtained from two reference sources; The Handbook of Geophysics and Space Environments [11] and Solar Radiation [12]. To avoid undue use of referencing in the text, please assume the aforementioned references for Section 3.

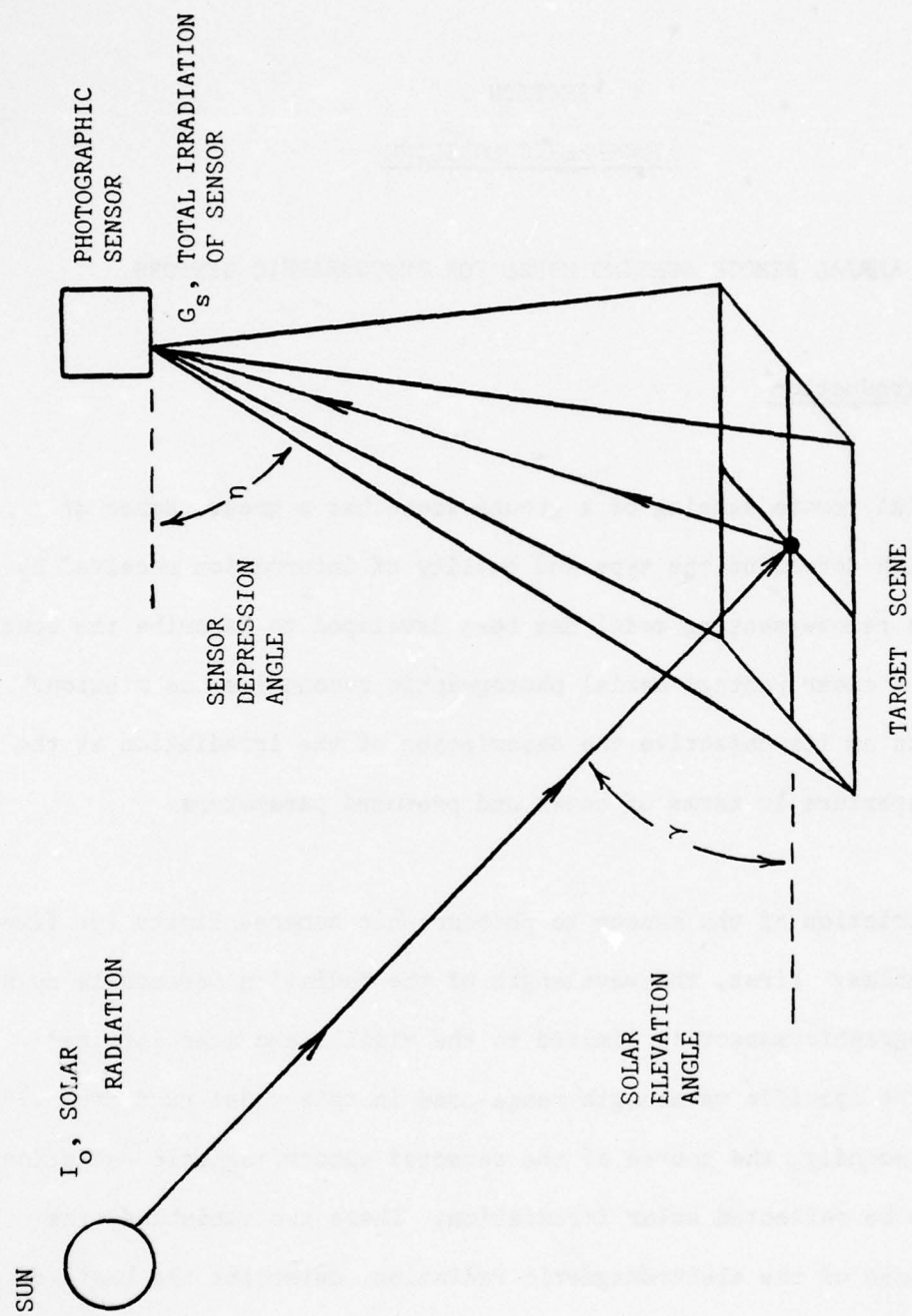


Figure 3-1



### 3.1.2. Basic Remote Sensing Model

The remote sensing model follows the path of the electromagnetic radiation from its source, the sun, to the target scene and then to the sensor, and takes the form:

$$G_S = h_A(g_{TS}(f_A(I_0)))$$

where  $I_0$  is the solar irradiation above the earth's atmosphere,  $f_A$  is the functional transformation by the atmosphere  $I_0$  from the top of the atmosphere to the target scene,  $g_{TS}$  is the functional transformation on  $f_A(I_0)$  by the target scene and  $h_A$  is the functional transformation of  $g_{TS}(f_A(I_0))$  by the atmosphere from the target scene to the sensor. Fortunately, these functions can be modeled by relatively simple additive and multiplicative terms. Both  $f_A$  and  $h_A$  are modeled the same way, only different limits are used. The atmospheric transformation is modeled as an attenuating medium plus a noise source, so that

$$f_A(I_0) = I_0 * T_{A1} + D_{A1} = I_1$$

where  $T_{A1}$  is the percentage of  $I_0$  which was transmitted by the atmosphere and  $D_{A1}$  is the irradiation of the target scene due to sources other than the

direct beam of sunlight. The function  $g_{TS}(I_1)$  can be modeled as two multiplicative terms, so that

$$g_{TS}(I_1) = R_{TS} * \text{Geom} * I_1 = I_2$$

where  $R_{TS}$  represents the reflectivity of the target scene and Geom represents the detailed geometric considerations of the sun-target scene-sensor system. Finally,  $h_A(I_2)$  has the same form as  $f_A(I_0)$ , so that

$$h_A(I_2) = (I_2 * T_{A2}) + D_{A2} = G_S$$

Combining all the models of the various functions, we have the basic model as

$$G_S = ((R_{TS} * \text{Geom} * ((I_0 * T_{A1}) + D_{A1})) * T_{A2}) + D_{A2} \quad (3-1)$$

This is the basic model of the aerial photographic sensing system. It should be stressed that every term, excepting Geom, is a function of the wavelength of the radiation. This wavelength dependence is one of the prime reasons that a model of the aerial photographic system is needed. Even though a material will have an approximately constant spectral signature, as represented by the term  $R_{TS}$ , the other atmospheric terms, which are all wavelength dependent, can cause the detected signature to change as a result of changing atmospheric conditions. To the extent that all of these other terms can be computed, then the detected signature can be transformed back to the material signature.

### 3.1.2.1. Atmospheric Effects

The effects of the atmosphere on the detected radiation have been modeled in the basic model by four terms:  $T_{A1}$ ,  $D_{A1}$ ,  $T_{A2}$  and  $D_{A2}$ . The terms  $T_{A1}$  and  $T_{A2}$  represent the attenuation of intensity caused by the atmospheric transmission medium, while  $D_{A1}$  and  $D_{A2}$  represent the noise of that transmission medium. These noise terms,  $D_{A1}$  and  $D_{A2}$ , represent the luminosity of the atmospheric medium. This luminosity has two sources: emissive and scattered radiation. These attenuating and luminosity effects depend upon the nature of the atmospheric medium. Therefore, the atmospheric medium must be modeled so that these effects may be calculated based upon the condition of the atmosphere.

#### 3.1.2.1.1. A Model Atmosphere

The atmosphere is a complex, time-varying mixture of gases and suspended particles of various sizes, shapes and composition. In order to calculate the effect the atmosphere will have upon the propagation of E-M radiation, mathematical models of the different physical effects observed have been developed. Since these models require certain atmospheric parameters as input variables, a representation of the atmosphere which defines these atmospheric parameters has been developed.



Simplifying approximations were made which reduce the complexity while retaining the significant characteristics of the atmosphere. The most difficult aspect of the atmosphere to model is its variation over time and space. Since the atmosphere does vary, the exact condition of the atmosphere at a given time and place will be unknown unless data describing its condition is collected at that time and place. This type of data is rarely available for routine aerial reconnaissance. However, certain parts of the atmosphere remain fairly constant over time and geographic location.

The gaseous composition of the atmosphere tends to be invariant with respect to its main constituents. Nitrogen (78.08%), oxygen (20.95%) and argon (.934%) constitute over 99.9% of atmospheric gases for a normal, clean, dry atmosphere. Of the other constituent gases only carbon dioxide (.031%) and other trace gases (such as methane, sulfur dioxide, etc.) have any significant variations with respect to time and place. The one constituent of a normal atmosphere neglected in the above accounting is water vapor. Water vapor is the one major gaseous constituent of the atmosphere that has major variations over time and space. However, even for a saturated atmosphere, the maximum water vapor content is approximately 1%. Thus, for atmospheric effects which depend on the bulk effects of the atmosphere, such as scattering, the atmospheric gases can be considered essentially invariant with respect to time. However, for atmospheric effects which depend selectively on a particular constituent(s) gases, such as absorption, the variability of these gases should be considered, even if the gases represent a very small part of the total.

Even though the relative amounts of the main atmospheric gases remain relatively constant, the density of these gases changes drastically with altitude. For example, an order-of-magnitude decrease in atmospheric density occurs in going from sea level to an altitude of 18 km. Such major variations must be accounted for when calculating atmospheric effects. Additionally, meteorological variations of temperature and pressure will cause small variations of the atmospheric density at a given altitude.

In addition to the gaseous components of the atmosphere, the effects caused by the suspended particles (or aerosols) must be accounted for. Aerosols are not as uniform over time and space as are the atmospheric gases. The relative material composition, the size distribution and the total density of the aerosols in the atmosphere are all subject to variation over time, geographic location and altitude. Such local conditions as dust storms, volcanic activity and industrial pollution can radically change atmospheric aerosol content in a region. In addition to the drastic conditions, normal meteorological and geographic variations cause aerosol content to vary to some extent. The aerosol density, as with the gases, varies with altitude. Aerosol densities decrease quite rapidly with increasing altitude, exhibiting an order-of-magnitude decrease in the 3 km rise above sea level for a clear standard atmosphere.

Another variation in atmospheric aerosols occurs in cloud formations. Clouds (and fog) are just volumes of the atmosphere containing very high densities of liquid and/or solid particles of water. As such, clouds represent the largest source of aerosol variation encountered under normal

circumstances. Because of the extremely high variability in time and space that clouds exhibit, they will be treated separately from the normal aerosol effects.

The effects on a beam of electromagnetic radiation produced by atmospheric aerosols are essentially the same two effects produced by the atmospheric gases: scattering and absorption. The scattering effect of the aerosols (sometimes including atmospheric molecular scattering) is observed as atmospheric haze.

One other effect that the atmosphere produces is thermal or blackbody emission or radiation. Thus, modeling the magnitude of the effects of the atmosphere on electromagnetic radiation requires modeling the effects of the absorption, scattering and thermal emission of atmospheric gases, aerosols and clouds.

A model atmosphere which would precisely describe the state of the atmosphere at a given time and place would be too complex and cumbersome to use. Certain simplifying approximations were be made as to the condition of the atmosphere in order to model it without an inordinate amount of descriptive atmospheric data. The model atmosphere consists of a series of homogeneous layers at different altitudes (see Figure 3-2). Each atmospheric layer is assumed to have constant atmospheric conditions, such as temperature, pressure, atmospheric and aerosol densities, composition, etc. This layered model allows the order-of-magnitude changes with altitude of certain atmospheric conditions to be included in the calculation of atmospheric effects



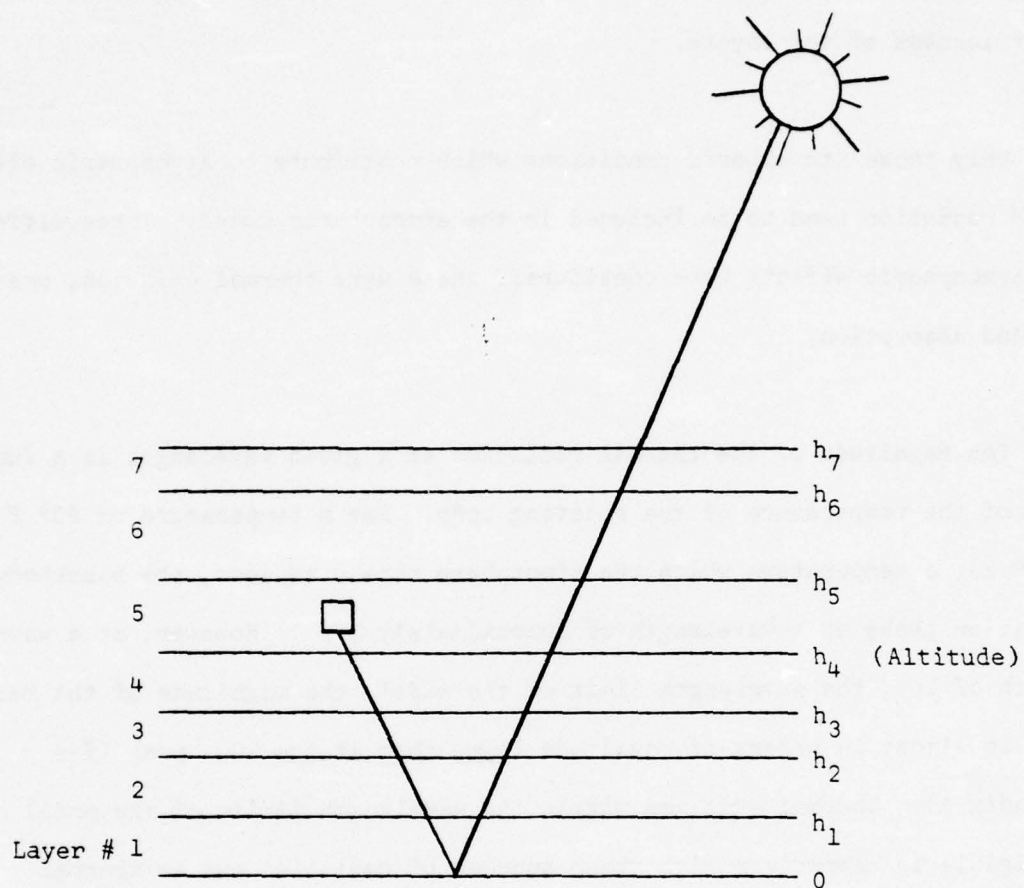


Figure 3-2 Example of Layered Atmosphere

while reducing the atmospheric description from continuous functions to a series of discrete values. The precision of such a layered model depends on the thickness of the layers.

Only those atmospheric conditions which contribute to atmospheric effects on EM radiation need to be included in the atmospheric model. Three different atmospheric effects were considered; these were thermal emission, scattering and absorption.

The magnitude of the thermal radiation at a given wavelength is a function of the temperature of the emitting body. For a temperature of  $80^{\circ}\text{ F}$  ( $300^{\circ}\text{ K}$ ), a temperature which the atmosphere rarely exceeds, the blackbody radiation peaks at a wavelength of approximately  $10\mu$ . However, at a wavelength of  $1\mu$ , the wavelength limit of the model, the magnitude of the radiation is almost 14 orders-of-magnitude lower than at the  $10\mu$  peak (See Appendix A). Thermal emission within the wavelength limits of the model are negligible in comparison with other sources of radiation and so thermal emission is ignored. It should be noted, however, that an extension to wavelength further into the infrared region would necessitate the inclusion of thermal emission as a significant effect.

Scattering occurs over the entire range of wavelengths and particle sizes, but the mathematical description of scattering in the general case is too cumbersome and complex, requiring a detailed knowledge of the radiation and particle involved. However, for limited ranges of wavelength and particle

sizes, mathematical models describing the bulk-scattering effects of a homogenous medium of randomly positioned and oriented particles, have been developed.

For the wavelength region of interest and the particle size and density constituting the atmosphere, the scattering effects can be described as a combination of two bulk-scattering models, Rayleigh scattering and Mie scattering. Rayleigh scattering is the scattering due to particles which are small compared to the wavelength of the radiation; thus the atmospheric gas molecules constitute Rayleigh scatterers. Mie scattering is due to particles of the same general size as the wavelength of the radiation and so the atmospheric aerosols act as Mie scatterers.

Rayleigh scatterers, essentially the  $N_2$  and  $O_2$  molecules, are of a consistent size and shape with only the densities changing. Thus, Rayleigh scatters may be described simply and accurately by the atmospheric density number for a given atmospheric layer.

Mie scatterers are more complex, including a variety of types, shapes, sizes and densities. To accurately describe Mie scattering would require data regarding the shapes, sizes and densities of the aerosols; however, this information would not be attainable without a tremendous data collection effort. Therefore, the effect of an aerosol content of a clear standard atmosphere is modeled in such a manner that only the density of the aerosols is retained as a variable. Thus, only two atmospheric parameters, the atmospheric number density and the aerosol number density, are used for each layer to calculate the scattering effect of the atmosphere.



Absorption of radiation is a highly wavelength-specific effect, and a highly material-specific effect. To explain why various molecules will only absorb radiation at specific wavelengths requires a quantum mechanical model of the interaction between radiation and matter. It is sufficient for this atmospheric model to simply state that each molecular constituent of the atmosphere will uniquely absorb radiation at specific wavelengths. This absorption effect can severely reduce the radiation transmitted through the atmosphere, even when the absorber occurs in trace amounts. Over the wavelength region of interest, three atmospheric constituents have an appreciable effect; they are ozone, water vapor and carbon dioxide. Of these, carbon dioxide has a minimal effect and has been neglected in the model. The only atmospheric parameter of importance needed to calculate the effect of an absorber is the density of the absorber. Thus, the density of water vapor and ozone at each atmospheric layer are needed to complete the description of the model atmosphere.

The model atmosphere developed to predict the effect that the atmosphere would have on radiation transmitted through it consists of four parameters: the atmospheric number density, the aerosol number density, the concentration of atmospheric water vapor and the concentration of ozone. These parameters allow the significant atmospheric effects of scattering and absorption to be modeled within the wavelength range of  $.38$  to  $1.0\ \mu$ . To account for changes of the parameters as a function of altitude, the average value of the parameter between two altitudes is used as the value of the parameter throughout that layer of atmosphere.

### 3.1.2.1.2. Atmospheric Attenuation

One of the two primary effects of the atmosphere upon propagating radiation is the attenuation of its intensity. For a given path from point P to point Q through the atmosphere, and a given intensity of radiation at point P,  $I_P$ , then the intensity of radiation at point Q,  $I_Q$ , is given by the equation

$$I_Q = I_P \exp\left[-\int_P^Q a(\lambda) ds\right] \quad (3-2.1)$$

where  $a(\lambda)$  is the wavelength-dependent extinction coefficient per unit length and  $ds$  is the differential length along path PQ. The variable  $\lambda$  will represent the wavelength of the radiation throughout the discussion of atmospheric effects. If the effects of refraction are negligible, then the path PQ becomes a straight line. Equation 3-2.1 can then be written as

$$I_Q = I_P \exp\left[-\int_{H_P}^{H_Q} a(\lambda) \sec\theta dh\right] \quad (3-2.2)$$

where  $H_Q$  is the height of point Q,  $H_P$  is the height of point P,  $dh$  is the differential height increment and  $\theta$  is the angle between the line PQ and the horizontal. The extinction coefficient per unit length,  $a(\lambda)$  is due to both atmospheric scattering and absorption and is therefore dependent upon the atmospheric composition. But the model atmosphere developed consists of layers of homogenous atmosphere. This being the case, Equation 3-2.2 can be further simplified into the form

$$I_Q = I_P \exp\left[- \sum_{h=H_P}^{H_Q} a(\lambda, h) \sec\theta \Delta h\right] \quad (3-2.3)$$

or

$$I_Q = I_P * \exp[-\tau_a(\lambda, P, Q) \sec\theta]$$

$$\text{where } \tau_a(\lambda, P, Q) = \sum_{h=H_P}^{H_Q} a(\lambda, h) \Delta h.$$

Let  $\tau_a$  be referred to the extinction coefficient from P to Q.  $\tau_a$  is a compound function, consisting of both absorption and scattering effects. These two different effects can be separated, so that  $\tau_a = \tau_S + \tau_A$ , and Equation 3-2.3 becomes

$$I_Q = I_P * \exp[-(\tau_S + \tau_A) \sec\theta] \quad (3-2.4)$$

$$= I_P * \exp(-\tau_S \sec\theta) * \exp(-\tau_A \sec\theta)$$

or

$$I_Q = I_P * TS(P, Q, \lambda, \theta) * TA(P, Q, \lambda, \theta)$$

$$\text{where } TS = \exp(-\tau_S(P, Q, \lambda) * \sec\theta)$$

$$\text{and } TA = \exp(-\tau_A(P, Q, \lambda) * \sec\theta)$$

Finally, by combining TS, TA so that



$$T_{PQ}(P, Q, \theta, \lambda) = TS(P, Q, \theta, \lambda) * TA(P, Q, \theta, \lambda) \quad (3-2.5)$$

where  $T_{PQ}$  is the atmospheric transmission factor from P to Q along path-slant angle  $\theta$ .

Recapping the foregoing

$$I_P = I_Q * T_{PQ}(P, Q, \theta, \lambda)$$

where  $T_{PQ} = TS(P, Q, \theta, \lambda) * TA(P, Q, \theta, \lambda)$

where  $TS(P, Q, \theta, \lambda) = \exp(-\tau_S(P, Q, \lambda) * \sec\theta)$

and  $TA(P, Q, \theta, \lambda) = \exp(-\tau_A(P, Q, \lambda) * \sec\theta)$

where  $\tau_S(P, Q, \lambda) = \sum_{h=H_P}^{H_Q} \tau_S(\lambda, h) \Delta h$

and  $\tau_A(P, Q, \lambda) = \sum_{h=H_P}^{H_Q} \tau_A(\lambda, h) \Delta h$

where  $\tau_S(\lambda, h)$  is the extinction coefficient due to scattering and  $\tau_A(\lambda, h)$  is the extinction coefficient due to absorption.

### 3.1.2.1.2.1. Atmospheric Scattering

The attenuating effect of atmospheric scattering upon propagating radiation has been modeled by the term

$$TS(P,Q,\theta,\lambda) = \exp - (\sec\theta * \sum_{h=H_P}^{H_Q} \tau_S(h, \lambda) \Delta h).$$

Everything but the term  $\tau_S(h, \lambda)$  is only a function of the specified atmospheric path. The term  $\tau_S(h, \lambda)$  represents the physical mechanisms responsible for scattering. As was stated earlier, the atmospheric scattering can be modeled as two separate scattering phenomena: Rayleigh scattering and Mie scattering. Therefore, the extinction coefficient due to scattering can be broken into two terms so that

$$\tau_S(h, \lambda) = \tau_R(h, \lambda) + \tau_M(h, \lambda)$$

where  $\tau_R(h, \lambda)$  is the Rayleigh scattering extinction coefficient and  $\tau_M(h, \lambda)$  is the Mie scattering extinction coefficient.

### 3.1.2.1.2.2. Rayleigh Scattering

Rayleigh scattering is that scattering which occurs when the scattering particle is roughly spherical and small compared to the wavelength of the

radiation. This requirement that the scattering particle be small is usually set so that the radius of the particle,  $r$ , is  $r < 0.1\lambda$ . For the wavelength region of interest, this condition is met by the gas molecules composing the atmosphere.

The Rayleigh scattering extinction coefficient,  $\tau_R(h, \lambda)$ , can be expressed as factors which independently are functions of  $h$  and  $\lambda$ , so that

$$\tau_R(h, \lambda) = \sigma(\lambda) * N(h) \quad (3-3.1)$$

where the Rayleigh scattering cross section;

$$\sigma(\lambda) = (5.408 \times 10^{25}) * (\mu - 1)^2 / \lambda^4 \text{ (m}^2\text{)} \quad (3-3.2)$$

and  $N(h)$  = atmospheric number density at altitude  $h(\text{m}^{-3})$

The variable  $\mu$  represents the real index of refraction of the scatters. This variable is wavelength dependent, and is given by the equation

$$(\mu - 1) = \left( 64.328 + \frac{29498.10}{146 - 1/\lambda^2} + \frac{255.40}{41 - 1/\lambda^2} \right) \times 10^{-6} \quad (3-3.3)$$

at a temperature of  $288^\circ \text{ K}$  and a pressure of 1013.25 mb. The temperature and pressure dependency of the refractive index have been neglected as second-order effects.



Since  $\sigma$  is only a function of  $\lambda$  and not  $h$ , the summation of the Rayleigh extinction coefficient,  $\tau_R$ , can be accomplished as

$$\sum_h \tau_R(h, \lambda) \Delta h = \sigma(\lambda) * \sum_h N(h) \Delta h$$

Since Equations (3-3.2) and (3-3.3) define  $\sigma(\lambda)$  in terms of  $\lambda$ , and  $N(h)$  is acquired from the model atmosphere,  $\tau_R$  is defined for a given atmosphere.

#### 3.1.2.1.2.3. Mie Scattering

Mie scattering is that scattering which occurs due to particles of roughly the same size as the wavelength of the scattered radiation. The approximate size range of the radii of particles causing this scattering is  $0.1\lambda < r < 25\lambda$ . The theory and mathematical models used to describe this phenomenon are quite complex, due to the interaction of the radiation which has been reflected, refracted and diffracted by the scatters. The size and shapes of natural aerosols vary widely, ranging in size from particles with radii of  $10^{-3}$  to  $10^2 \mu$ . Not only do the aerosols vary in size, but the distribution of the different sizes vary over time and space, especially over altitude.

Both the lack of data on the size distribution of aerosols for a given time and place, and the extreme complexity of the Mie theory have led to the development of a simpler model for aerosol scattering based on empirical measurements. This model depends upon two tabulated variables, the aerosol scattering coefficient at sea level as a function of wavelength and the

aerosol number density as a function of altitude. The aerosol number density,  $N_p$ , is one of the components of the model atmosphere. The aerosol scattering coefficient at sea level,  $B_p$ , has been tabulated for certain wavelengths. The Mie scattering extinction coefficient is then given by

$$\tau_M(h, \lambda) = B_p(\lambda) * N_p(h)/N_p(0).$$

Therefore,

$$\sum_h \tau_M(h, \lambda) \Delta h = \sum_h \beta_p(\lambda) * N_p(h)/N_p(0) \Delta h = \frac{\beta_p(\lambda)}{N_p(0)} * \sum_h N_p(h) \Delta h$$

#### 3.1.2.1.2.4. Atmospheric Absorption

Atmospheric absorption is not an effect caused by the bulk properties of atmosphere as is scattering, but an effect due to the specific absorption spectrum of each atmospheric constituent. Even atmospheric constituents comprising but a small fraction of the atmosphere can have a major attenuation effect. The atmosphere happens to be remarkably transparent in the .38 to 1.00 $\mu$  region of the spectrum. Only 2 gases, ozone and water vapor, have important effects within this spectral region and even these gases have their primary absorption effects outside of this region. Carbon dioxide constitutes a strong near infrared absorber, but it has no appreciable effect until a wavelength of approximately 2.0 $\mu$ .

Each molecule has a unique absorption and, conversely, emission spectrum. This absorption spectrum is the result that energy states are quantized.

Only energy transitions of certain values are allowed by the structure of a particular atom or molecule. Each allowed energy transition is accompanied by the emission or absorption of a quanta of light with the energy equal to that transition.

The energy of a quanta of light is related to the wavelength of the light by the relationship

$$E = hc/\lambda$$

where  $E$  = energy of the quanta (J)

$h$  = Planck's constant =  $6.625 \times 10^{-34}$  (Js)

$c$  = speed of light =  $3.00 \times 10^8$  (m/s)

and  $\lambda$  = wavelength of the radiation (m)

Certain factors cause a broadening of the energy transitions allowed so that absorption occurs in a narrow band of wavelengths instead of one exact wavelength. The mathematics and theory of the absorption spectra of a molecule is very complex, so that absorption spectra are obtained by empirical measurements. Therefore, the model of atmospheric absorption is based on empirical wavelength-dependent functions and the atmospheric concentration of a given absorber.

The effect of atmospheric absorption has been modeled by the term  $\tau_A$ , the absorption extinction coefficient. Since each absorber acts independently



of other absorbers, each attenuation effect due to absorption can be calculated independently.

The effect of atmospheric absorption has been modeled by the term,  $\tau_A(\lambda, h)$ , the extinction coefficient due to absorption. Then the effect, along path PQ at slant angle  $\theta$ , is given by

$$TA = \exp(-\sec\theta * \sum_{h=H_p}^{H_Q} \tau_A(h, \lambda) \Delta h). \quad (3-4.1)$$

This type of expression has been used to model the effect of ozone absorption, but not the effect due to water vapor absorption. Instead, the effect of water vapor absorption has been modeled as a separate attenuation term, such that

$$TA = TW(P, Q, \lambda, \theta) * (\exp(-\sec\theta * \sum_{h=H_p}^{H_Q} \tau_{O_3}(h, \lambda) \Delta h)) \quad (3-4.2)$$

where  $TW$  = the attenuation due to water vapor

and  $\tau_{O_3}$  = the extinction coefficient due to ozone absorption.

The extinction coefficient due to ozone absorption,  $\tau_{O_3}$ , is derived from two empirical tabulated variables: the Vigroux ozone absorption coefficient,  $A_v(\lambda)$ , and the ozone concentration  $N_{O_3}(h)$ . The ozone concentration, at a given altitude, is obtained from the model atmosphere while values of the ozone absorption coefficient have been evaluated and tabulated for certain wavelengths. The extinction coefficient due to ozone absorption is given by the following simple relationship

$$\tau_{O_3}(h, \lambda) = A_V(\lambda) * N_{O_3}(h) \quad (3-4.3)$$

From this it follows that

$$\sum_{h=H_P}^{H_Q} \tau_{O_3} \Delta h = A_V(\lambda) \sum_{h=H_P}^{H_Q} N_{O_3}(h) \Delta h. \quad (3-4.4)$$

Thus, by Equation (3-4.4), the effect of absorption due to atmospheric ozone has been defined in terms of the ozone concentration of the model atmosphere, the altitudes at the beginning and end of the atmospheric path, and the path slant angle for a given wavelength.

The effect of water vapor absorption is also calculated on the basis of empirical measurements. The  $\text{LOG}_{10}$  of the attenuation due to water vapor is obtained from a table as a function of total precipitable water in the atmospheric path,  $w$ , and the wavelength of the radiation,  $\lambda$ . The total precipitable water along an atmospheric path has been calculated by the following formula

$$w = \sec \theta * \sum_{h=H_P}^{H_Q} w \text{ pcm } (\Delta h) \quad (3-5)$$

where  $w \text{ pcm } (\Delta h)$  = the amount of precipitable water (in cm) between two given altitudes

The term  $w \text{ pcm } (\Delta h)$  is obtained from the model atmosphere. Thus, by Equation (3-5) and an empirical table of attenuation coefficients, the atmospheric

effect due to water vapor absorption has been defined in terms of the model atmosphere, the altitude limits of the beginning and end of the atmospheric path and the path slant angle for a given  $\lambda$ .

### 3.1.3. Atmospheric Luminosity

#### 3.1.3.1. Introduction

The atmosphere acts as a source of radiation as well as acting as an attenuator. This atmospheric luminosity can be attributed to two distinct phenomena, emissivity and scattering. This luminosity is the manifestation of noise that degrades every transmission medium. In the basic remote sensing model, the two terms  $D_{A1}$  and  $D_{A2}$  represented this atmospheric luminosity. The major degradation effect of the atmospheric medium due to atmospheric luminosity is caused by the  $D_{A2}$  term, since most of the information of the photographic output is due to the reflectivity of the target scene which appears after degradation caused by  $D_{A1}$ .

#### 3.1.3.2. Emissive Radiation

The emissivity of the atmosphere is due to the same factors which cause atmospheric absorption. However, it is convenient to separate this phenomenon into two parts, thermal or blackbody emissivity and photochemical emissivity. Blackbody radiation has been discussed previously and it has been shown that for normal temperatures, blackbody radiation is insignificant for wavelengths of  $1.00\mu$  and shorter. The photochemical emissivity here refers to the



energy of molecules with electrons in an excited state as well as unstable molecules caused by chemical changes induced by radiation absorption. Empirical measurements have shown that except for times at night, such photochemical emissivity is negligible when compared to the luminosity caused by scattering. Therefore, no factor due to atmospheric emissivity has been included in the model.

#### 3.1.3.3. Scattered Radiation

The radiation which is scattered by the atmosphere from a beam of radiation is simply redirected at some angle from the original beam. This redirected light can be considered as an anisotropic source of light from a small volume of atmosphere. Therefore, the scattered sunlight from the atmosphere not in the direct atmospheric path appears as a separate source of radiation.

#### 3.1.3.4. Skylight

In the case of the irradiation of the target scene, the entire half sphere of the visible sky acts as a source of scattered radiations and is commonly known as skylight. The intensity of skylight is considerable, as can be demonstrated by the illumination of an area shadowed by an opaque object while still open to most of the sky. The computation of this skylight from scattering theory is extremely complex and more exact than can be justified by the rest of the model. An approximate value of the total skylight irradiating a horizontal plane can be obtained by the following formula:

$$D_{\text{SKY}}(\lambda) = k * (I_A(\lambda) - I_T(\lambda)) * \sin \gamma \quad (3-6)$$

where  $D_{\text{SKY}}$  = the total diffuse radiation irradiating a horizontal target scene

$k$  = empirical coefficient =  $0.5 * (\sin \gamma)^{1/3}$

$I_T$  = direct solar irradiation of the target scene (includes atmospheric attenuation from both absorption and scattering)

$I_A$  = direct solar irradiation of the target scene if only atmospheric attenuation by absorption is considered

and  $\gamma$  = solar elevation angle

Using the terms defined in previous sections, Equation (3-6) can be rewritten as

$$D_{\text{SKY}}(\lambda) = k * I_0 * TA * (1 - TS) * \sin \gamma$$

Thus,  $D_{\text{SKY}}$  is defined by variables already calculated for a given wavelength. Since emissivity is negligible,  $D_{\text{A1}}$  is simply equal to  $D_{\text{SKY}}$ .

#### 3.1.3.5. Backscatter

The other atmospheric luminosity term in the basic model is represented by the term  $D_{\text{A2}}$ . This term represents the radiation received by the sensor due to the luminosity of the atmospheric cone between the sensor and the

target scene. Since atmospheric emissivity is negligible, the luminosity is due entirely to the radiation scattered back into the camera's field of view and is therefore referred to as backscatter. Three sources of radiation exist which can contribute to the backscatter radiation: direct solar-irradiation of the atmospheric cone, skylight irradiation of the atmospheric cone and reflected irradiation from the ground. Of these three sources, only direct solar irradiation will be used in the model. This is because direct solar irradiation is the predominate source of the atmospheric cone illumination and that the other two sources are not calculable from the models so far developed. Neglecting these two sources will cause the calculated backscatter to be smaller than the actual backscatter. The size of the error will depend upon the extent to which the direct solar irradiance predominates. Since scattering is anisotropic, the distribution of the scattered radiation must be known in order to calculate the amount scattered in a particular direction. For the Rayleigh scattering phenomenon, the Rayleigh scattering coefficient at angle  $\theta$  and wavelength  $\lambda$ ,  $\beta(\theta, \lambda)$ , is given by the following formulation

$$\beta_R(\theta, \lambda) = \frac{2 * \pi^2}{N * \lambda^4} * (\mu(\lambda) - 1)^2 * (1 + \cos^2 \theta) \quad (3-7)$$

where  $N$  = number of scatters per unit volume  
 $\mu(\lambda)$  = wavelength-dependent index of refraction  
 $\lambda$  = wavelength of the radiation  
 and  $\theta$  = angle between the incident beam and the scattered radiation.



The problem of aerosol scattering is much more complex, since aerosols have a distribution of different sizes. For a given  $\lambda$ , the scattering pattern will vary tremendously due to changes in the size of the aerosol. The complications that this problem represents defy the use of a simple model dependent upon the aerosol density. Therefore, this model of backscattering will only include Rayleigh scattering, no aerosol scattering will be included.

Applying Equation (3-6) to the calculation of atmospheric backscatter is complicated by the fact that radiation in different parts of the FOV must be scattered through different  $\theta$ 's. The model used to calculate the backscatter consists of dividing up the cone into a series of layers, and computing the amount of radiation projected into the FOV from each layer. The calculation of this radiation involves the integration of Equation (3-6) over the area of the layer. This calculation (see Appendix B) is quite complicated due to the fact that  $\theta$  is a function of position within the area. Because of this complication, the integration was solved only for the simplest case, a circular FOV with a depression angle,  $\eta$ , equal to  $90^\circ$  (i.e., looking straight down). The irradiance from each layer, after being appropriately attenuated by intervening atmospheric layers, is added together to compute the final value of backscatter.

#### 3.1.3.6. Target Scene Reflectivity and System Geometry

The target scene reflects some of the incident solar irradiation into the remote aerial photographic sensor. This reflection into the sensor has

been modeled by two multiplicative terms: the target reflectivity,  $R_{TS}$ , and the scene geometry factor,  $Geom$ .

The complete description of the scene geometry would require that the topography of the target scene area be known. This information is not generally available, so the target scene is assumed to be a flat, horizontal plane. This assumption will generally be valid or only slightly in error for most target scenes. For large scale areas, the average topography is fairly flat despite local variations away from the horizontal.

The target reflectivity can be a complex function of many variables. First consider two types of ideal reflectors, the purely specular reflector and the purely diffuse reflector. The purely specular reflector is realized in a high-grade plane mirror. A beam of light incident on a mirror at angle  $\theta$ , will be completely reflected at an angle  $-\theta$ . All of the light will remain in the reflected beam. The purely diffuse reflector is approximated by a plane of white dust, such as fine chalk dust. The diffuse plane reflector reflects an incident beam throughout the entire half sphere above the reflector. For a perfectly diffuse plane reflector, the reflector appears as a uniform radiator. This type of reflector is called a Lambertian reflector.

Most materials fall between the extremes of a perfect specular and a perfect diffuse reflector, exhibiting features from both types. However, most materials, especially as viewed from an aerial platform, exhibit reflectivity which is nearly Lambertian in its angular distribution of radiation. Unlike the perfect reflectors, most materials will absorb some portion

of the incident radiation. Indeed, it is the unique pattern of absorption over wavelength which defines the spectral signature of a material. Therefore, the reflectivity of the target scene has been modeled as a spectrally flat, partially absorbing, Lambertian reflector.

The geometry of the aerial sensor in relation to the target determines what portion of the total radiation flux is captured by the sensor. This percentage of captured flux is represented by the term, Geom, in the basic model. The form which Geom takes depends upon the type of reflector modeled. Since a Lambertian reflector has been used in this model, Geom takes the form of

$$\text{Geom} = \frac{\text{AREA} * \sin \eta}{2 * \pi * P^2}$$

where      AREA =      the area of the target scene viewed by the photographic sensor

$\eta$  =      depression angle of the sensor

and              P =      length of the path from the target scene to the photographic sensor

The area viewed by the photographic sensor, AREA, is determined by the field of view (FOV) of the sensor and the height of the sensor above the target. The length of path, P, is determined by the depression angle and the height of the sensor above the target. The term,  $\sin \eta$ , accounts for the projection of the flat plane into angles other than the normal angle.



Including the reflection of the target scene,  $R_{TS}$ , the radiation projected into the sensor by the target scene,  $I_2$ , is given as

$$I_2 = \frac{\text{AREA} * \sin \eta}{2 * \pi * p^2} * R_{TS} * I_1$$

where  $I_1$  = the irradiation of the target scene.

#### 3.1.4. Astronomical and Geographical Factors

##### 3.1.4.1. Introduction

Since the sun is the source of the radiation reflected by the target scene, it is necessary that position and intensity of this solar radiation be known. The intensity of the solar radiation is represented in the basic remote sensing model by the term,  $I_o$ . This solar intensity,  $I_o$ , is the irradiation at the top of the atmosphere, and is a function of the wavelength of the radiation. The solar position is not directly represented in the basic model, but the solar elevation angle,  $\gamma$ , and the solar azimuth,  $A_o$ , are needed in the calculations of the other basic terms.

##### 3.1.4.2. Solar Intensity

The solar intensity at the top of the atmosphere integrated over all wavelengths is called the solar constant, and has a value of approximately

2.0 cal/cm<sup>2</sup>min. However, the requirements of the basic model dictate that the solar constant be known as a function of wavelength. This spectral solar irradiation,  $I_o(\lambda)$ , is approximated by a piecewise integrated function, such that the value of the radiation over some small interval of wavelengths is used. This piecewise function,  $I_o(\Delta\lambda)$ , has been measured and tabulated over the spectral region of interest in this model.

The spectral solar irradiation has two sources of variation. The first source of variation is due to the variation in the radiation output of the sun. The sun apparently goes through cycles of various periods during which the radiation output changes slightly. These changes are not accurately predictable. Fortunately, these changes are negligibly small within the .38 - 1.00  $\mu$  wavelength range of interest. The second source of variation of  $I_o$  is due to change in the earth-to-sun distance as the earth travels in its solar orbit. The tabulated values of  $I_o(\Delta\lambda)$  is for the mean radius of the earth-sun orbit. To correct  $I_o$ , simply multiply  $I_o$  by the square of the ratio of mean radius to the current radius, so that

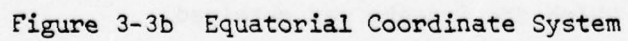
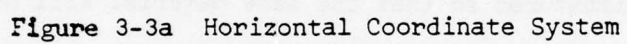
$$I_o(\Delta\lambda) = \left(\frac{R_o}{R}\right)^2 * I_o(\Delta\lambda)_{MEAN}.$$

This multiplication simply represents the inverse square law of EM radiation. The calculation of the current radius is done in Appendix C, and depends only on the angular position of the earth in its orbit.

#### 3.1.4.3. Solar Position

The solar position is, of course, a term relative to some coordinate system. The coordinate system of interest to the basic model is the target scene-centered (or horizontal) coordinate system. In the horizontal coordinate system, the zenith point (the point directly above the observer), the north-south line, and the horizon are the three reference axes. (See Figure 3-3a). The position of the sun on the celestial sphere is then determined by two angular variables: the solar elevation angle  $\gamma$ , and the solar azimuth,  $A_0$ . The solar elevation angle is the angular distance between the horizon and the solar position along the arc containing the zenith and the sun. The azimuth is the angular distance between the arc containing the zenith and the sun and south point along the horizon. The horizontal coordinate system is subjective; that is, dependent on the geographical position of the observer. The easiest means of calculating the solar position for such a coordinate system is to calculate the solar position in an objective coordinate system and then transform that position to the subjective system. Such an objective coordinate system is the equatorial coordinate system, in which the polar axis, the celestial equator and the orbital equinox points provide the reference axis (See Figure 3-3b). It is possible to locate the sun in the equatorial system by knowing the time and date for a given longitude. The solar position on the equatorial system and the geographic latitude and longitude of the target scene are then sufficient to calculate the solar elevation angle and the solar azimuth. The mathematics of these calculations are performed in Appendices D and E.





### 3.2. LIMITATIONS OF THE MODEL

The aerial remote sensing model developed has several simplifying assumptions, approximations, and restrictions included in it. The accuracy of the model will depend upon the validity of the assumptions and approximations, while the usefulness of the model will depend upon the restrictions. Some of these assumptions and restrictions have been mentioned previously, while others will be introduced here.

This model was developed for the purpose of normalizing multispectral photographic target signatures so that the same material will have the same signature under various circumstances. This particular model was designed as an a priori model; that is, it works independently of information contained in the imagery. Rather, information known prior to the development of the film, such as the time and date of the flight, is used to determine the parameters of the model. By using this ancillary data, it is possible to directly model effects that could be only indirectly modeled or in some cases not modeled at all without it.

The following eight data items were used as model parameters:

- 1) the geographic location of the target scene,
- 2) the elevation of the target scene,
- 3) the time at which the imagery was obtained,
- 4) the date on which the imagery was obtained,
- 5) the altitude of the sensor,

- 6) the field of view of the sensor,
- 7) the depression angle of the sensor and
- 8) the center wavelength and bandwidth of each multispectral band.

These data items are routinely available from aerial reconnaissance missions. No other data items pertinent to the model are commonly available.

As mentioned, an important restriction is that the wavelengths of all multispectral band lie within the .38 to 1.00  $\mu$  range. This restriction is compatible with the use of photographic sensors.

Another restriction is that the solar elevation angle should be greater than 5°. This is due to approximations becoming less valid at extremely low sun angles, such as negligible refraction of the incoming solar beam. However, at solar elevation angles this low, the scene illumination is very low and so aerial reconnaissance is rarely taken under these conditions.

The major restriction is that clear sky or nearly clear sky weather conditions must exist. Clouds are very difficult to model due to the variety of their types, sizes, shapes and locations. A thin, high altitude cirrus cloud will affect radiation much differently than a low altitude nimbus cloud. The internal structure of the aerosol distribution of each cloud would have to be known in order to calculate the effect of the cloud. Also, clouds are highly variable in position over time. The information needed to model the effect of clouds is simply not available, and since clouds can be



the dominant atmospheric effect, it is necessary to restrict the use of this model to cloud-free areas of the imagery.

A restriction imposed by the model is that the depression angle of the sensor be  $90^\circ$ . The integration needed to calculate the atmospheric backscatter has been solved for only a circular FOV. Because aerial reconnaissance photographs are often taken with a depression angle of  $90^\circ$ , this restriction does not severely limit the mode.

Related to the previous restriction is an approximation of the backscatter for rectangular FOV's. The backscatter for a rectangular FOV has been approximated as the backscatter for a circular FOV with an area equal to the area of the rectangle. As previously discussed, the total backscatter was approximated by only the Rayleigh scattering of the direct solar illumination of the cone. This approximation will cause the calculated backscatter term to be smaller than the actual value.

Two approximations related to the target scene are that the target scene is modeled by a horizontal plane and that the reflectivity of the scene is modeled by a Lambertian reflector.

The data items used as parameters did not include any information concerning the state of the atmosphere. The condition of the atmosphere has already been restricted to being essentially cloudless. However, the atmospheric number density, the aerosol number density, the ozone concentration and the water vapor concentration, all as a function of altitude, are

parameters needed by the model atmosphere. Therefore, these parameters have been tabulated for a normal, clear atmosphere and form the "standard" atmospheric model normally used by the program. Therefore, as the condition of the atmosphere deviated from this standard, the effects predicted by the model will deviate from the actual effects. If the deviation of the predicted effects compared to the actual effects is small, then the model is still valid for those atmospheric conditions. In addition to the standard model, the simulation program allows the user to supply the values over altitude of any of the four other model atmosphere parameters, allowing for a more accurate model, when such variables are known about the actual atmosphere.

Both the atmosphere and the solar irradiation are continuous functions, but these functions are expressions of a physical phenomenon which are measured in discrete samples. Inclusion of these data in a data file allows both for the convenience of changing models and easy utilization of measured data.

### 3.3. COMPUTER PROGRAM

#### Basic Structure

The computer program of the aerial remote sensing model was implemented in FORTRAN on the DEC 11-20 RADC Image Processing System. Implementation of the various mathematical models is quite straightforward in FORTRAN. Summations are easily implemented through DO loops, and other basic arithmetic and

trigonometric functions are part of the FORTRAN language. The basic structure of the program consists of a main program, a chain of nested subroutines, and data files. The basic structure of this program is shown in Figure 3-4. Each subroutine performs some specific function, with information being passed either through subroutine parameter lists or through the common block. Description of the function each routine performs is provided in Table 3-1. By structuring the program in this manner, changes or improvements are much easier to make since each subroutine is an independent module.

#### File Structure

The data files are the manner in which the tabulated data concerning the atmospheric condition, scattering and absorption coefficients, and the solar irradiation are input into the program. The main program, ATMCOR, reads in these files and puts them into the common storage area. These files must be stored on the RP02 disk if the program is to operate. A separate FORTRAN user routine, APFWRT, will write out these standard atmospheric parameter files onto the disk. If nonstandard parameter files on the condition of the atmosphere are to be used, they must be on the RP02 disk in the correct format. These nonstandard files can be selected as an option of the main program.

The structure of these atmospheric data files consists of a one-dimensional paired array. For atmospheric number density, aerosol number density and ozone concentration files, the first part of the pair is an altitude above sea level and the second part is the value of the variable at that



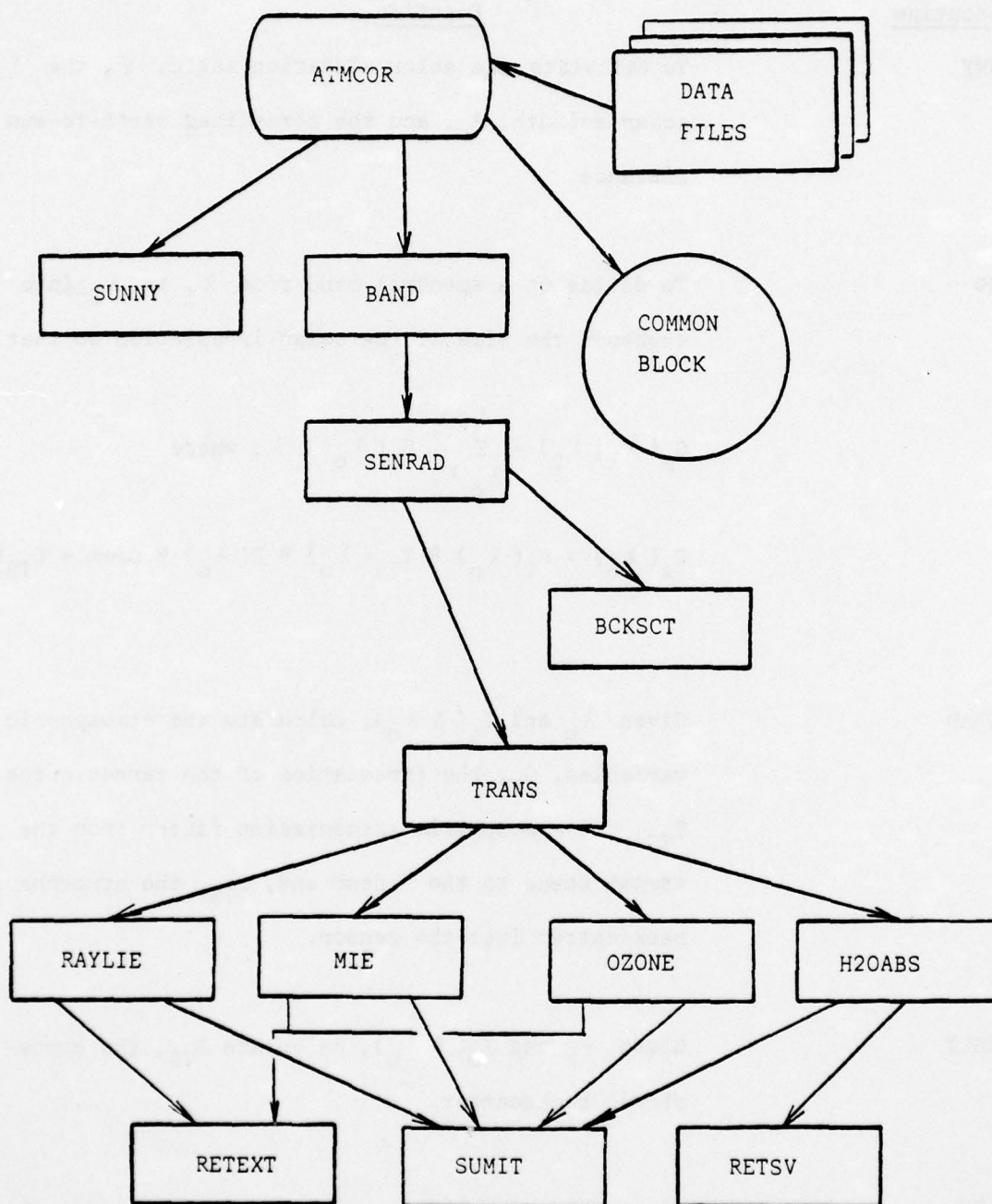


Figure 3-4 Program Structure

Table 3-1

<u>Subroutine</u>	<u>Function</u>
SUNNY	To calculate the solar elevation angle, $\gamma$ , the solar azimuth, $A_o$ , and the normalized earth-to-sun distance.
BAND	To divide up a spectral band from $\lambda_1$ to $\lambda_2$ into subbands the size of the solar irradiation so that $G_s(\lambda_1, \lambda_2) = \sum_{\lambda_o = \lambda_1}^{\lambda_2} G_s(\lambda_o) \Delta \lambda; \text{ where}$ $G_s(\lambda_o) = G_T(\lambda_o) * T_{TS}(\lambda_o) * R(\lambda_o) * \text{Geom} + D_{TS}(\lambda)_o$
SENRAD	Given $\lambda_o$ and $I_o(\Delta \lambda_o)$ , calculate the atmospheric variables, $G_T$ , the irradiation of the target scene, $T_{TS}$ , the atmospheric transmission factor from the target scene to the sensor and, $D_{TS}$ , the atmospheric backscatter into the sensor.
BCKSCT	Given $\lambda_o$ and $I_o(\Delta \lambda_o)$ , calculate $D_{TS}$ , the atmospheric backscatter.
TRANS	Given $\lambda_o$ , high and low altitude limits, and path slant angle, calculate the atmospheric attenuation

coefficient due to scattering, TS, and the atmospheric attenuation coefficient due to absorption, TA.

RAYLIE

Given  $\lambda_0$ , high and low altitude limits, and path slant angle, calculate the Rayleigh scattering extinction coefficient  $\tau_R$ .

MIE

Given  $\lambda_0$ , high and low altitude limits, and path slant angle, calculate the aerosol (Mie) scattering extinction coefficient,  $\tau_M$ .

OZONE

Given  $\lambda_0$ , high and low altitude limits, and path slant angle, calculate the ozone absorption extinction coefficient,  $\tau_{O3}$ .

H2OABS

Given  $\lambda_0$ , high and low altitude limits, and path slant angle, calculate the attenuation coefficient due to water vapor, TW.

SUMIT

Given high and low limits, and the name of an atmospheric 1-D paired data file, compute the summation from the low limit to the high limit on the atmospheric parameter in the specified file.

RETEXT

Given the name of an atmospheric 1-D paired data file and a value for the independent variable,



retrieve an extrapolated value for the dependent variable.

RETSV

Given the name of an atmospheric 1-D index file and a parameter value, find the index with the largest value which is still less than the parameter value.

altitude. All of the altitudes are sequentially ordered in increasing altitude first, then followed by the values of the variable.

The water vapor concentration file is constructed in the same manner with the following exception: the value of the variable is for the amount of the precipital water (in cm) between its paired altitude and the next higher altitude in the list.

It should be noted that no constraint is placed on the number of different altitudes or the spacing between the altitudes listed in the data.

#### 3.4. TESTS ON ATMOSPHERIC CORRECTION PROGRAM

Naturally, extensive tests on the output of individual modules were conducted while the atmospheric correction program was being written. Still, it was felt necessary to compare the output of the program with typical measured values of atmospheric extinction.

The altitude of the test scene is placed at 1.742 km because some of the data to which the computed values are to be compared was taken at observatories at this elevation. The camera is placed at an altitude of 2 km to make atmospheric extinction negligible along the path from scene to camera. This also served to facilitate comparison with astronomical data.

The first test consisted of a direct check of the values of solar radiation being used by the program against values tabulated in Allen [13], for

AD-A040 769

PATTERN ANALYSIS AND RECOGNITION CORP ROME N Y  
ADVANCED DIGITAL EXPLOITATION TECHNIQUES (ADET). (U)

F/G 15/4

APR 77 G E FORSEN, F H FENG, M J GILLOTTE

F30602-75-C-0141

UNCLASSIFIED

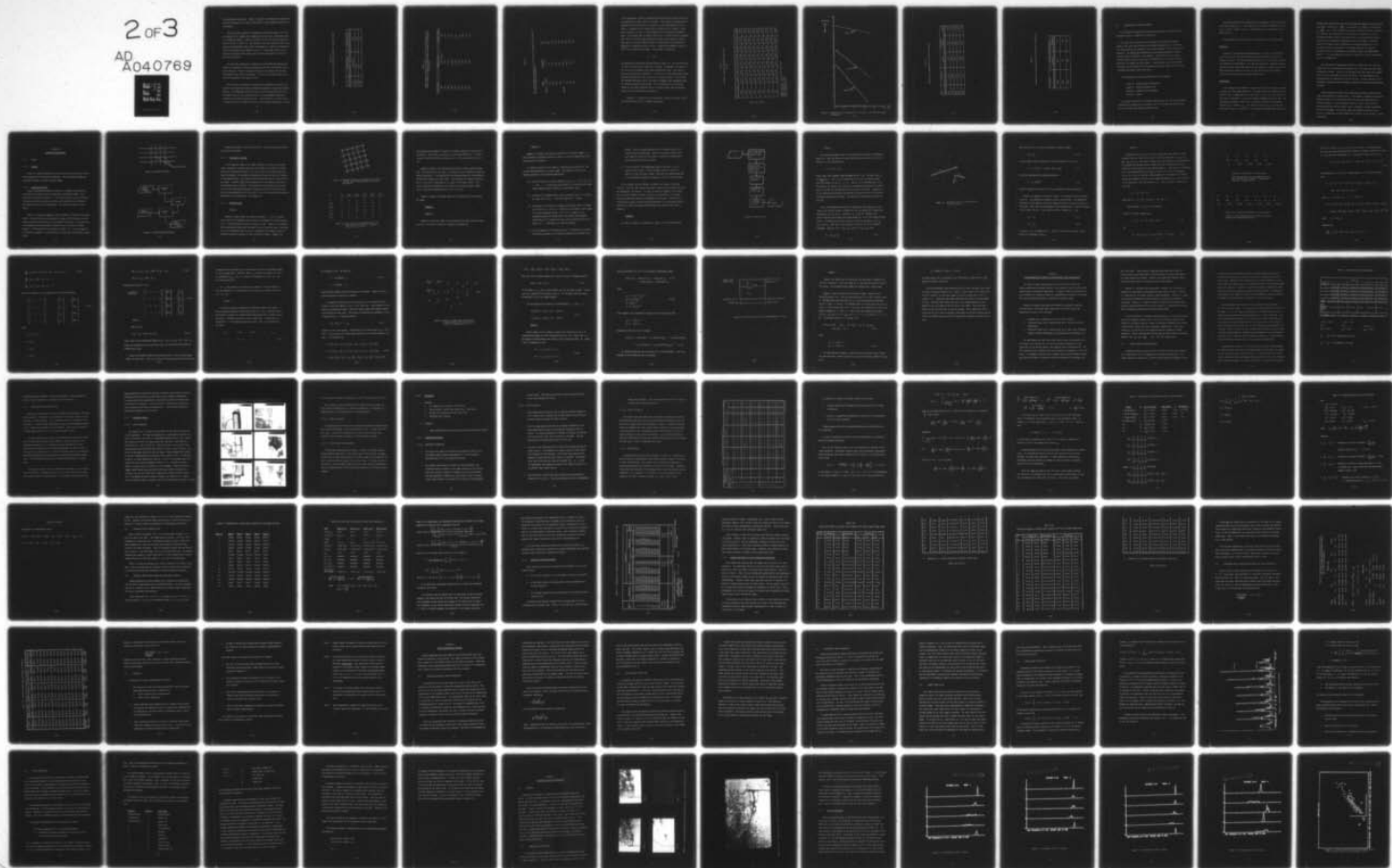
PAR-77-3

RADC-TR-77-145

NL

2 of 3

AD  
A040769





three different wavelengths. Table 3-2 presents this comparison showing that the power impinging on the earth's atmosphere is being computed correctly by the program.

The second test consisted of comparing the elevation angles of the sun as computed by the program with angles computed from solar coordinates given in the Nautical Almanac. Table 3-3 presents the data for various times on 2 Aug 1974 at 90° W. and 40° N. The computed values are symmetrical about noon because an approximation made within the program is to ignore the Equation of Time in computing the hour angle of the sun. A more recent version of the program has corrected this problem and the small discrepancies of Table 3-3 have been eliminated.

The third test consisted of computing the total radiation reaching the camera at a sequence of times and longitudes such that the elevation of the sun is constant. Table 3-4 presents this data. The entries show another approximation made within the program. The sun is held fixed during the day and moved discretely upon change of date.

The fourth test consisted of comparing the atmospheric extinction computed by the program with typical extinctions measured at astronomical observatories. The wavelengths of  $\lambda 3850$ ,  $\lambda 4200$ , and  $\lambda 7000$  were chosen for study. The camera was only 250 m above the scene, so the atmospheric extinction computed will be one way extinction only. The altitude of the target scene is taken to be 1742 m, equal to that of the Mount Wilson Observatory. Options

ter

Table 3-2  
Computed Values of Solar Radiation Compared to Tabulated Values

$\lambda$	Computed Values	Tabulated Values
	//////	//////
3850	.1189 W/m <sup>2</sup> Å	.118
4200	.1903	.189
7000	.1444	.149

Table 3-3  
 Computed Solar Elevation on 2Aug74 at 90° W and 40° N Compared to  
 Values Computed by Hand from Solar Right Ascension and Declination  
 on That Date

Local Time	/	Computed Values	/	Almanac Values
800		.5962 radians		.578
900		.7931		.774
1000		.9763		.961
1100		1.1226		1.10
1200		1.1839		1.18
1300		1.1226		1.14
1400		.9763		.998
1500		.7931		.818
1600		.5962		.620



Table 3-4

The scene radiation (arbitrary units) reaching the camera for latitude  $53^{\circ}$  at various times and longitudes:

<u>Time</u>		<u>Longitude</u>	<u>GT</u>
13Nov74	930 GMT	$0^{\circ}$ E	.952
	1230	$45^{\circ}$	.952
	1530	$90^{\circ}$	.952
	1830	$135^{\circ}$	.952
	2130	$180^{\circ}$	.952
14Nov74	30	$135^{\circ}$ W	.928
	330	$90^{\circ}$ W	.928
	630	$45^{\circ}$ W	.928
	930	$0^{\circ}$ E	.928

in the atmospheric correction program were exercised which allowed the radiation reaching the target scene to be output. This number is computed by the program as the flux falling on an element of surface perpendicular to the zenith. Consequently, the number must be divided by  $\cos \gamma$ , where  $\gamma$  is the solar elevation, in order to obtain effects due to atmospheric extinction alone. The computed data is given in Table 3-5, in which we see, for example, that .4673 of the total light available at 3825° A would reach the ground. From Table 3-5 we can construct Figure 3-5, which gives the extinction in magnitudes (a logarithmic scale in which 1 magnitude represents a factor of  $100^{1/5}$ ) as a function of air-mass. The air-mass  $x$  is given by

$$x = \csc \gamma.$$

The magnitudes of extinction are also shown in Table 3-6. We see from Figure 3-5 that the extinction is linear with air-mass. Furthermore, the slope of the curves can be compared with typical astronomical data. This slope is known as the extinction coefficient. In Table 3-7 we show measurements taken from Basic Astronomical Data along with our computed values. We note that the standard atmosphere used in the model is somewhat less transparent than the corresponding astronomical data. This is probably due to an aerosol content of the model atmosphere which is slightly higher than the aerosol content near the Mount Wilson Observatory.

In general, it appears that the atmospheric correction program is working satisfactorily within its design constraints.

Table 3-5

Fraction of Sunlight Reaching Target Scene

 $\lambda_o (\text{\AA})$ 

$T_{\text{sun to target}}$	3825	3875	4175	4225	6975	7025	$\gamma$ (Rad)
0800	.4673	.4852	.5770	.5898	.8642	.8670	.5962
0900	.5493	.5656	.6483	.6597	.8914	.8936	.7931
1000	.5973	.6125	.6888	.6992	.9058	.9078	.9763
1100	.6227	.6373	.7099	.7197	.9131	.9149	1.1226
1200	.6306	.6450	.7165	.7261	.9153	.9171	1.1839
1300	.6227	.6373	.7099	.7197	.9131	.9149	1.1226
1400	.5973	.6125	.6888	.6992	.9058	.9078	.9763
1500	.5493	.5656	.6483	.6597	.8914	.8936	.7931
1600	.4675	.4852	.5770	.5898	.8642	.8670	.5962

Time of Day (CST)

Target Altitude = 1742 m above sea level

Target Latitude =  $40^{\circ}$  NTarget Longitude =  $90^{\circ}$  W

Date = August 2, 1974



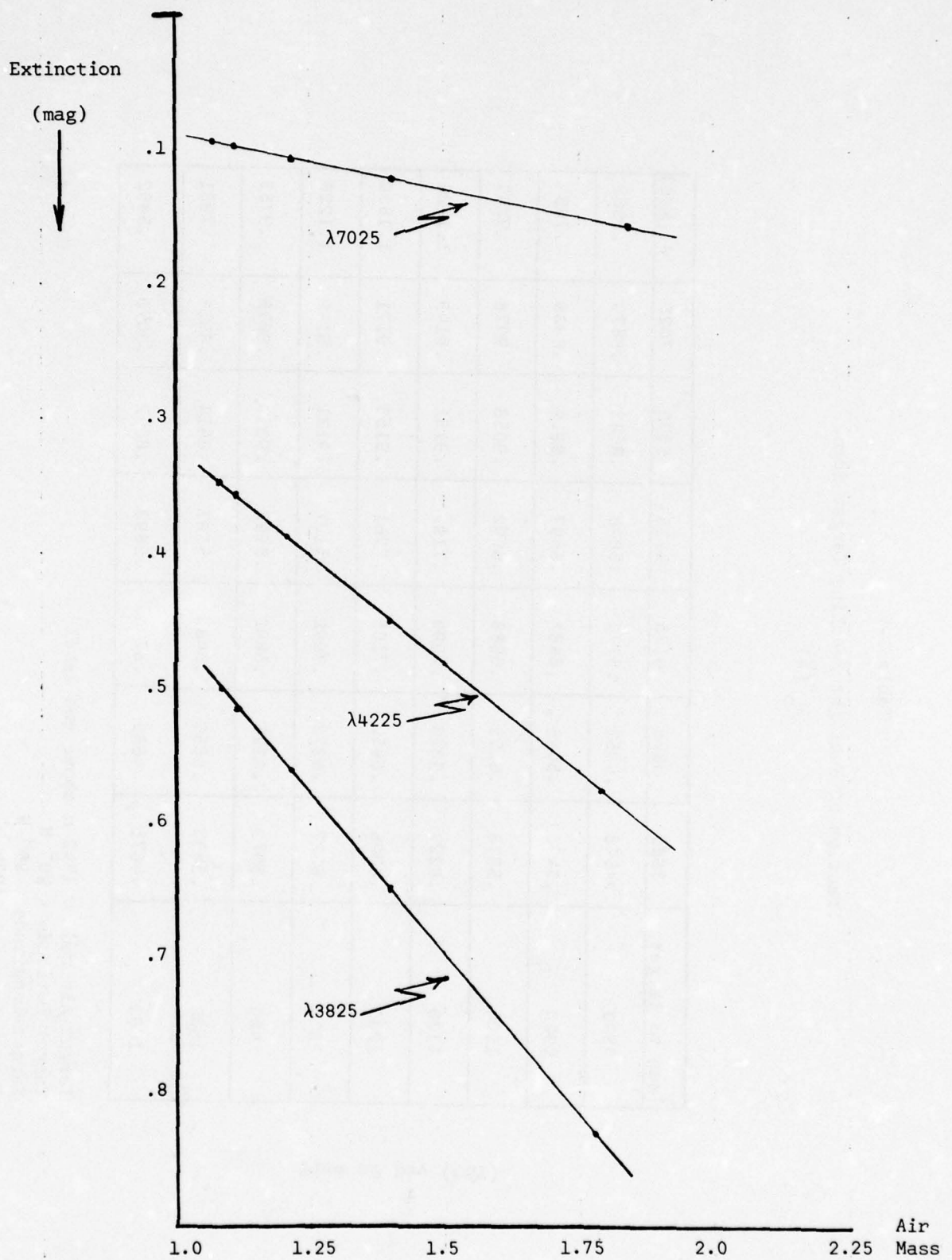


Figure 3-5 Computed Values of Extinction as a Function of Air Mass for Several Wavelengths

Table 3-6  
Extinction in Magnitudes for Various Air Masses

Time	Air Mass	Extinction		
		$\lambda 3825$	$\lambda 4225$	$\lambda 7025$
800	1.781	.8260	.5732	.1550
900	1.403	.6505	.4516	.1221
1000	1.207	.5595	.3885	.1050
1100	1.110	.5143	.3571	.0966
1200	1.080	.5006	.3475	.0940

Table 3-7  
Comparison of Computed and Measured Extinction Coefficients

Wavelength	Extinction Coefficient	
	Computed	Measured
λ3825	.464	.42
λ4225	.322	.305
λ7025	.087	.07



### 3.5. APPLICATION TO DIGITIZED IMAGERY

The procedure recommended for applying the parameters, derived from the atmospheric model, to image data is given here.

The image data is assumed to be multispectral consisting of several images of the same scene recorded over different spectral bands. Each band is characterized by two parameters; the center wavelength of the band and the bandwidth. The appropriate parameters are calculated according to the formulation already presented in this section. Descriptions as to how these data are output for the on-line user of DICIFER and as to how they should be applied to the imagery are given below. A more detailed account of program structure will be available in the corresponding user's manual which is to be a separate publication under this effort.

The following four output options exist for this program:

- Option #1 - Between Scene Normalization
- Option #2 - Maximum Radiation Flux
- Option #3 - Radiation Flux Components
- Option #4 - Debug

The output from Option #2, Maximum Radiation Flux, is just the calculated radiation flux incident upon the sensor,  $G_S(\lambda)$ , with the scene reflectivity set to 1 for each user specified spectral band.

The output from Option #3, Radiation Flux Components, is the two additive terms which compose  $G_S(\lambda)$ . The first term, the reflected radiation flux, is  $(G_T(\lambda) * R_T(\lambda) * \text{Geom} * T_{TS}(\lambda))$ . The second term is just the path luminance term,  $D_{TS}$ .

The reflectivity of the scene is a user-defined input for this option.

#### Option #1

Option #1, the Between Scene Normalization, is simply the output from Option #2 for a set of several different scenes normalized to one of the scenes in the set. The user has three suboptions as to which scene to use as the standard for normalization. The user can specify the "standard" scene or the user can have the routine search for the highest (or lowest) value for  $G_S$  among the various scenes of the set and use that scene for the standard. This would be done for each specified spectral band.

#### Application:

As an example of the manner in which this output could be used, consider the case of a three image scene set. Let image scene #1 be recorded at 1200 hours on June 1, image scene #2 at 1400 hours on June 1 and image scene #3 at 1200 hours on September 1, with other mission parameters being the same. For illustration purposes, suppose that the program calculates the following values for  $G_S$ : Scene #1,  $G_{S1} = 8.0 \text{ watt/m}^2$ ; Scene #2,  $G_{S2} = 6.0 \text{ watts/m}^2$ ; and Scene #3,  $G_{S3} = 5.0 \text{ watts/m}^2$ . If the user had selected Scene #2 as the

standard for normalization, then the following normalization factors would be calculated: Scene #1,  $N_1 = \frac{6.0}{8.0} = .75$ ; Scene #2,  $N_2 = \frac{6.0}{6.0} = 1$ ; and Scene #3,  $N_3 = \frac{6.0}{5.0} = 1.25$ . These normalization factors can then be used as multiplication factors. By multiplying all of the pixels in Scene #1 by .75, the differences between Scene #1 and Scene #2 due to the differences in scene illumination and atmospheric attenuation will be eliminated. Similarly, Scene #3 and Scene #2 can be normalized by multiplying Scene #3 by 1.25. The pixel-by-pixel multiplication of the gray values of an image by a constant value can be performed by the DICIFER routine FILE COMBINATIONS, Frame 18. It is anticipated that round off errors due to these calculations will not be significant.

When applying the normalization factors to image files, the user must remain alert to the restrictions imposed by the 8 bit/pixel gray level range available on DICIFER. That is, if an adjusted pixel gray value ever exceeds 255, it will be truncated to 255 for that pixel. The responsibility for preventing such an occurrence is left to the user. Careful selection of the "standard" scenes will yield successful completion of the scene normalization operation.

Certain approaches toward scene normalization may yield similar inter-scene normalization for special cases. As an example, histogram matching for different images of the same scene within the same time frame may yield acceptable results. Such an approach, however, does not lend itself to generalization over time and space, since a commonality of scene information may not be available. On the other hand, the approach described in this section is independent of scene content and, as such, is not subject to local constraints.



SECTION 4  
COMPUTER EYE CALIBRATION

4.1. EYECAL

4.1.1. Purpose

EYECAL is a FORTRAN program which is used to remove the geometric distortions produced by the Computer Eye digitizer. Raw, uncorrected images are processed by EYECAL to create corrected images.

4.1.2. Operating Procedure

During a digitization session the operator calibrates the geometrical distortion of the Computer Eye by digitizing a calibration reseau. This reseau is illustrated in Figure 4-1. The "fiducial points" are the points on the reseau which will actually be utilized for determining the distortion. The fiducial points lie on a square grid. This digitized image is named IMAGE0.

IMAGE0 is processed by segments A and B of EYECAL to produce a file named CALMAP. For each pixel in the Computer Eye images, CALMAP contains two real numbers which give the distortion in the image at that pixel. Any image which was digitized in the same session as IMAGE0 may be corrected with EYECAL segment C. This procedure is illustrated in Figure 4-2. The input image to be corrected by segment C is named IMAGE1, the corrected output image is named IMAGE2.

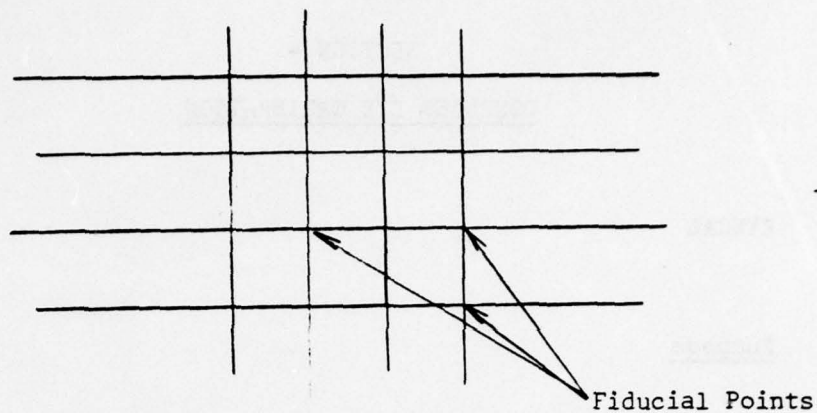


Figure 4-1 Calibration Reseau

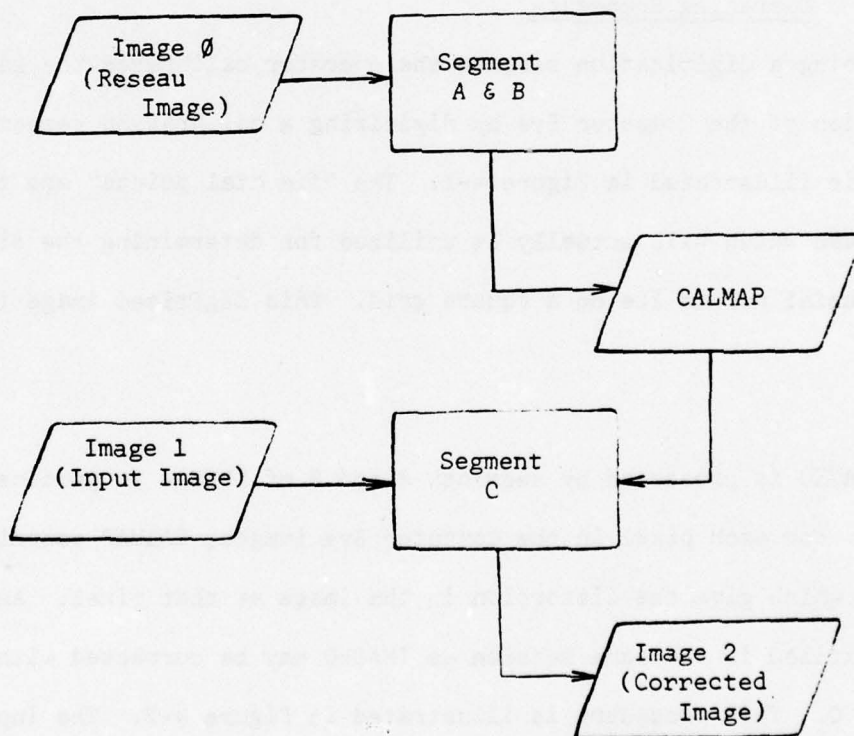


Figure 4-2 EYECAL Program Structure

EYECAL was written to run on the PDP 11/45. Two tape drives and an RP04 disk drive are utilized.

#### 4.1.3. Calibration Strategy

In the digitized image of the reseau (IMAGE0), the grid may have arbitrary translation, rotation, and scale with respect to the pixels of IMAGE0 because the orientation depends on the way in which the operator happens to place the reseau on the Computer Eye stage and because the scale will depend on the magnification. Thus, EYECAL makes no assumption about the position of the reseau. Instead, EYECAL fits a square grid to the apparent positions of the fiducial points in IMAGE0. The calibration then proceeds on the assumption that the discrepancy between the apparent position of a fiducial point and its corresponding best-fit grid point is due to the geometrical distortion introduced by the Computer Eye. See Figure 4-3.

#### 4.1.4. Program Details

##### Overview

Segment A accepts IMAGE0 and outputs the array  $v$ .  $v(k)$  is a complex number whose real (imaginary) part is the  $x(y)$  coordinate of the  $k$ th fiducial point. Complex numbers are used for economy of code. Figure 4-4 illustrates hypothetical gray values about the image of the  $k$ th fiducial point. Note that  $v(k)$  is the centroid of the  $k$ th point. Indexing of the fiducial points is arbitrary and has no relation to their location in IMAGE0. Segment A is



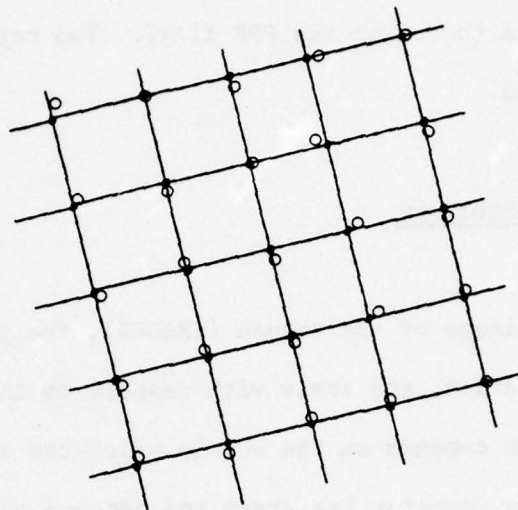


Figure 4-3 Apparent Positions of Fiducial Points (open circles) and Corresponding Best-Fit Square Grid (dots).

$I \quad J$	$J_0$	$J_0+1$	$J_0+2$	$J_0+3$	$J_0+4$	$J_0+5$
$I_0$	0	0	0	0	0	0
$I_0+1$	0	7	19	23	5	0
$I_0+2$	0	31	45	61	18	0
$I_0+3$	0	4	18	30	11	0
$I_0+4$	0	0	1	12	0	0
$I_0+5$	0	0	0	0	0	0

Figure 4-4 Gray Values in the Neighborhood of the Image of Fiducial Point K. Centroid =  $(I_0 + 2.12, J_0 + 2.53)$ .

distinguished from segment B, because A is highly dependent on the nature of the reseau. The values  $v$  are output to a file named VECTRZ.DAT. The first element of VECTRZ is NPOINT, the number of  $v$ 's, the second element is  $v(1)$ , etc.

Segment B accepts  $v$  and calculates the best-fit (least squares) square grid. The distortion at the point  $v$  is taken to be the difference between the best-fit grid and  $v$ . The distortion at the fiducial points is interpolated to estimate the distortion at each pixel. The distortion is defined as follows. Let  $z = (x,y)$  be the distortion at  $I,J$  pixel of the image, IMAGE2. Then  $I+x,J+y$  gives the coordinates of the pixel in the distorted image, IMAGE1, which is carried by distortion from  $(I,J)$  to  $(I+x,J+y)$ .

Segment C accepts a distorted image and a calibration map and corrects the image.

#### Segment A

##### Segment A1

Segment A1 copies the image of the calibration grid from IPS format tape into disk. The file so created is designated DB:PHOLES.IMG.

## Segment A2

Segment A2 of EYECAL calculates the centers of the pinhole images. It first identifies individual pinholes by means of a cluster algorithm and then calculates their centroids.

To identify clusters, use is made of a temporary file called MAP. MAP has the same dimensions as the input image. The elements of MAP are  $I \times J$  defined according to the following prescription:

- (1) Scan the pixels of the input image for  $I=1, J=1, \dots, 512$ ;  $I=2, J=1, \dots, 512, \dots$ . If the input pixel  $GRAY(I,J)$  is less than the noise cutoff threshold  $GRACUT$ ,  $MAP(I,J)$  is set equal to zero.
- (2) If  $GRAY(I,J)$  is greater than or equal to  $GRACUT$ , find  $J'$ , the smallest value of  $J+1, J+2, \dots$  for which  $GRAY(I,J') < GRACUT$ .
- (3) The length of the string of contiguous gray levels above the threshold is then  $J'-J$ . If  $J'-J = 1$ ,  $MAP(I,J)$  is set equal to zero, again as a noise suppression device. If  $J'-J = 2$ , search all the neighboring points of the MAP which have already been assigned. Since  $MAP(I,J-1)$  is known to be zero, only the points  $MAP(I-1,J-1)$ ,  $MAP(I-1,J)$ ,  $\dots$ , and  $MAP(I-1,J')$  need be examined.
- (4) If all neighbors of the string are zero, the elements of the array MAP which correspond to the string are assigned the integer value



NBLOBS. Since all upper neighbors of the string are zero, a new cluster has been encountered. NBLOBS is the unique integer which will index the points of the cluster, so NBLOBS is incremented to await detection of the next cluster.

- (5) If one or more of the neighboring points is non-zero, let the minimum value be KMIN. Then the elements MAP(I,J), MAP(I,J+1), ..., MAP(I,J'-1) are set equal to KMIN. Note that this abbreviated form of the clustering algorithm is designed to work on circular blobs.

Let the largest value of NBLOBS-1 be NPOINT, the number of clusters detected. Then the size, weight, and center of mass of each cluster are found and displayed on the console. The user is queried in regard to the minimum size (number of pixels) he wants to accept in his definition of "cluster." Spurious clusters can usually be eliminated at this point. The final list containing the number of points and the coordinates of the centers of mass is written into a disk file named DBO:VECTRZ.DAT to be used as input data to Segment B.

#### Segment B

The steps of Segment B illustrated in Figure 4-5 are discussed below.

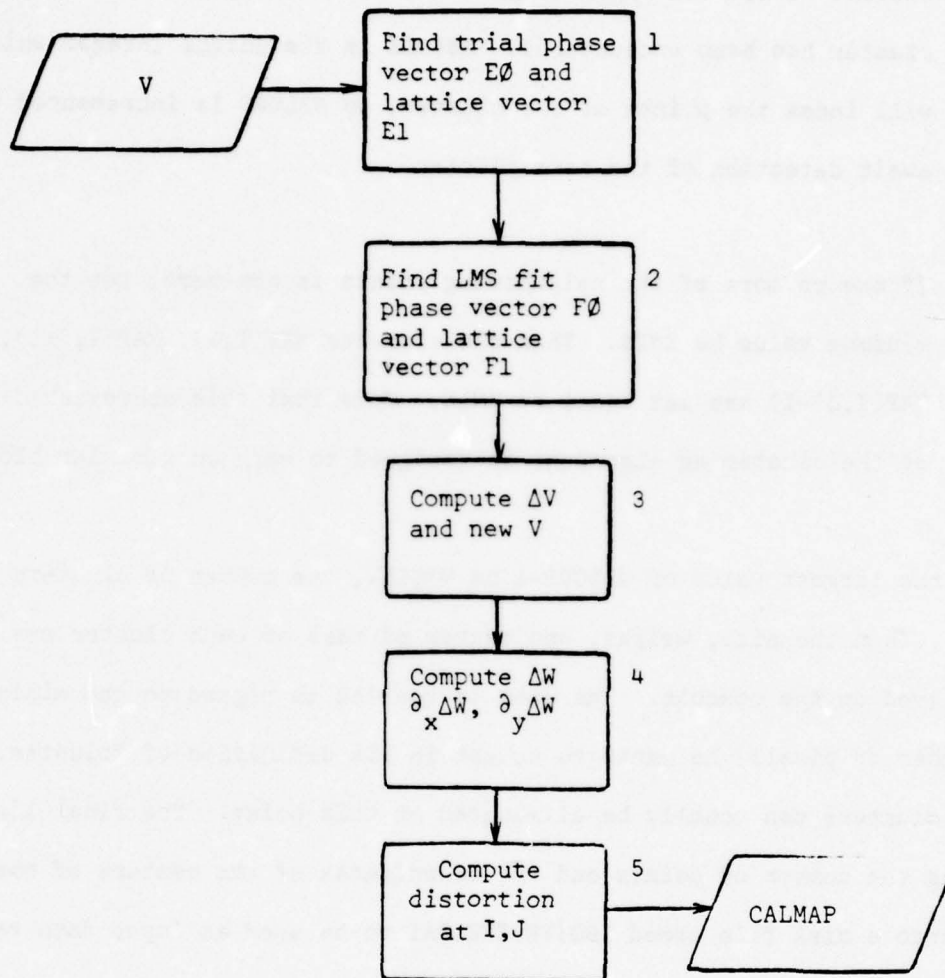


Figure 4-5 Steps of SEGB

## Module 1

The lattice and phase vector of a square grid are vectors illustrated in Figure 4-6. They are defined as those vectors which allow any point of the lattice,  $z$ , to be represented as

$$z = f_0 + mf_1 + nf_2 ,$$

where  $m$  and  $n$  are suitably chosen integers and  $f_2 = if_1$ . The pair  $(m,n)$  is the cycle of  $z$ . Let  $f_0$  be the "phase" and  $f_1$  (or  $f_2$ ) the lattice vector. Note from Figure 4-6 that  $f_1 \cdot f_2 = 0$ . That is,  $f_1$  is perpendicular to  $f_2$ . The phase of the lattice,  $f_0$ , defines the translational position of the grid, and it is simply the coordinates of any one point of the grid. Therefore,  $f_1$  (or  $f_2$ ) defines the rotational orientation of the grid, and it is the vector joining two adjacent grid points. The length of  $f_1$  determines the scale of the grid.

Due to the geometrical distortion introduced by the Computer Eye, the image of the fiducial points in IMAGE0 will not lie exactly on a square grid described by  $f_0$ ,  $f_1$ , and  $f_2$ . Define  $f_0$ ,  $f_1$ , and  $f_2$  for IMAGE0 as the lattice vectors which provide the least-squares best fit to the imaged fiducial points. To compute the vectors  $f_0$  and  $f_1$ , utilize an estimate,  $e_1$  for  $f_1$  and  $e_0$  for  $f_0$ . Note that  $f_2$  can always be found from  $f_1$  and is therefore redundant. That is, if  $f_1 = (f_{1x}, f_{1y})$  and  $f_2 = (f_{2x}, f_{2y})$ , then

$$f_2 = (-f_{1y}, f_{1x}) \quad (4.1)$$



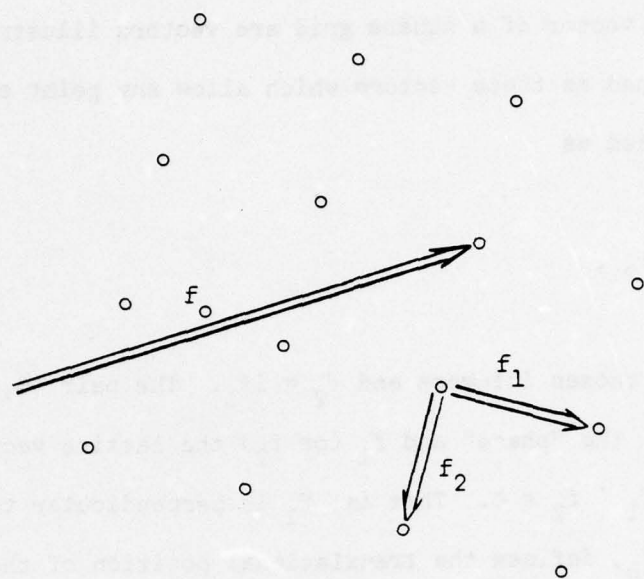


Figure 4-6 The Phase Vector  $f_0$  and the Lattice Vectors  $f_1$  and  $f_2$

Also note that, if  $f_1$  and  $f_2$  are treated as complex numbers,

$$f_2 = if_1. \quad (4.2)$$

In fact, given a pair of vectors  $P, Q$ , the dot product of  $P$  and  $Q$  is

$$P \cdot Q = (P_x, P_y) \cdot (Q_x, Q_y) = P_x Q_x + P_y Q_y \quad (4.3)$$

and may be represented in complex notation as

$$P \cdot Q = \text{Re}(P\bar{Q}), \quad (4.4)$$

where  $\text{Re}$  represents real part and the bar represents complex conjugation.

Module 1 of segment B as given in Figure 4-5 is concerned with estimating  $f_0$  and  $f_1$ . The estimates are denoted  $e_0$  and  $e_1$  respectively. The assumption employed in the estimation is that the image of the grid is least distorted at the center. Thus, find the coordinates of the fiducial point  $k'$  which is nearest to the point (256,256). Also, find the point  $k''$  nearest  $v_k$ . Then

$$e_0 \equiv v_{k'} \quad (4.5)$$

$$e_1 \equiv v_{k''} \quad (4.6)$$

In module 1,  $v_k$  is swapped with  $v_1$ . Module 1 echoes all the input  $v$ 's and prints the estimates  $e_0$  and  $e_1$ .

## Module 2

Suppose that the error in our trial lattice and phase vectors is small enough so that the cycle of any point  $z$  is the same for both  $\{e_0, e_1, \bar{e}_2\}$  and  $\{f_0, f_1, f_2\}$ . Any error in phase vector will appear as a constant error in locating the fiducial points, whereas any error in lattice vector will appear as a linear function of the distance from  $v_1$ . This point is illustrated for a one-dimensional array in Figure 4-7a and 4-7b. Thus, to determine  $\{f_0, f_1, f_2\}$  which is the best least-squares fit to the data, fit a linear (slope and constant) function to the differences between the  $v_k$  and the point of the trial grid which lies nearest to  $v_k$ . That is, given  $v_k$ , find  $(I, J)$  such that

$$v_k \approx e_0 + Ie_1 + Je_2. \quad (4.7)$$

Note that  $(v_k - e_0) / \bar{e}_1 = I$  and  $(v_k - e_0) / \bar{e}_2 = J$ .

Then determine  $f_0, f_1, f_2$  as follows:

Define  $M$ , the least squares sum.

$$M \equiv \sum_k |v_k - (f_0 + If_1 + Jf_2)|^2 \quad (4.8)$$

Let

$$f_0 = (C_x, C_y), f_1 = (A_x, A_y), \text{ and } f_2 = (-A_y, A_x). \quad (4.9)$$

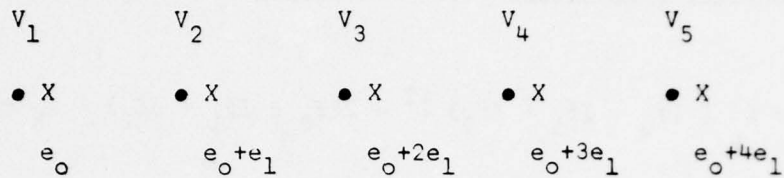


Figure 4-7a Phase Error in Trial Vectors

(The fiducial points are represented by dots. The trial points by crosses. A phase error produces a constant error.)

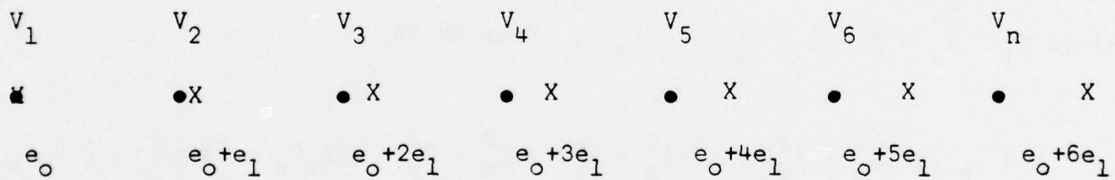


Figure 4-7b Lattice Vector Error in Trial Vectors

(A lattice vector error produces an error which grows linearly with displacement from  $V_1$ .)



Now, try to choose  $C_x, C_y, A_x, A_y$  so as to minimize  $M$ . Parenthetically, note that any square lattice has four degrees of freedom, position (2), scale (1), and rotational orientation (1). Evaluating  $M$  through use of (4.9),

$$M = \sum_k | (f_0 + If_1 + Jf_2) |^2 - 2(f_0 + If_1 + Jf_2) \cdot v_k + |v_k|^2 \quad (4.10)$$

The dependence of  $I$  and  $J$  on  $k$  through Equation 4.7 has been suppressed.

Then

$$M = \sum_k |f_0|^2 + (I^2 + J^2) |f_1|^2 + 2If_1 \cdot f_0 + 2Jf_2 \cdot f_0 - 2(f_0 + If_1 + Jf_2) \cdot v_k + |v_k|^2,$$

since  $f_1 \cdot f_2 = 0$  and  $f_1 = f_2$ . From (4.9)

$$M = \sum_k I^2(A_x^2 + A_y^2) + J^2(A_x^2 + A_y^2) + C_x^2 + C_y^2 + 2IA_x C_x + 2IA_y C_y - 2JC_x A_y + 2JA_x C_y - 2\sum_k Iv_x A_x + Iv_y A_y - Jv_x A_y + Jv_y A_x + v_x^2 + v_y^2 + v_x^2 + v_y^2,$$

where  $v_k = (v_x, v_y)$

Minimizing  $M$ ,

$$\frac{\partial M}{\partial A_x} \sum_k A_x I^2 + A_x J^2 + IC_x + JC_y - Iv_x - Jv_y = 0$$

$$\frac{\partial M}{\partial A_y} \sum_k A_y I^2 + A_y J^2 + I C_y - J C_x - I v_y + J v_x = 0 \quad (4.11)$$

$$\frac{\partial M}{\partial C_x} \sum_k C_x + I A_x - J A_y - v_x = 0$$

$$\frac{\partial M}{\partial C_y} \sum_k C_y + I A_y + J A_x - v_y = 0$$

The set of equations 4.11 are equivalent to the matrix equation

$$\begin{bmatrix} \alpha & 0 & \beta & \gamma \\ 0 & \alpha & -\gamma & \beta \\ \beta & -\gamma & \delta & 0 \\ \gamma & \beta & 0 & \delta \end{bmatrix} \begin{bmatrix} A_x \\ A_y \\ C_x \\ C_y \end{bmatrix} = \begin{bmatrix} \text{VEC1} \\ \text{VEC2} \\ \text{VEC3} \\ \text{VEC4} \end{bmatrix}, \quad (4.12)$$

where

$$\alpha = \sum_k I^2 + J^2,$$

$$\beta = \sum_k I,$$

$$\gamma = \sum_k J,$$

$$\delta = \sum_k 1,$$

$$\text{VEC1} = \sum_k I v_x + J v_y, \quad \text{VEC2} = \sum_k I v_y - J v_x, \quad (4.13)$$

$$\text{VEC3} = \sum_k v_x, \quad \text{VEC4} = \sum_k v_y.$$

Inverting the matrix in 4.12,

$$\frac{1}{(\beta^2 + \gamma^2 - \alpha\delta)} \begin{bmatrix} -\delta & 0 & \beta & \gamma \\ 0 & -\delta & -\gamma & \beta \\ \beta & -\gamma & -\alpha & 0 \\ \gamma & \beta & 0 & -\alpha \end{bmatrix} \begin{bmatrix} \text{VEC1} \\ \text{VEC2} \\ \text{VEC3} \\ \text{VEC4} \end{bmatrix} = \begin{bmatrix} A_x \\ A_y \\ C_x \\ C_y \end{bmatrix}. \quad (4.14)$$

Module 3

Define  $\Delta v_k$  as

$$\Delta v_k = f_k - (If_1 + Jf_2 + f_o). \quad (4.15)$$

Given a pixel of the undistorted image at  $If_1 + Jf_2 + f_o$ ,  $\Delta v_R = If_1 + Jf_2 + f_o$  yields the coordinates of the pixel into which the distortion has carried the original gray value.

During the correction stage, the calculations fill in the corrected image (IMAGE2) at each point. This is a function of the gray value at each point, and

consequently the algorithm needs to know where to look in the distorted image to find the gray value. Therefore, after  $v_k$  has been calculated, all the  $v_k$  are replaced by  $I_k f_1 + J_k f_2 + f_0$ , where the dependence of I and J on k has been denoted explicitly.

The  $v_k$  are precisely the correction we require. The only problem is that the correction  $v$  is known only at the points  $v_k$  (now equal, recall, to  $I f_1 + J f_2 + f_0$ ).

#### Module 4

In order to extend the distortion to arbitrary points of the image, simply extrapolate between the few known points  $v_k$ . The  $v_k$ , however, are not particularly convenient for extrapolation because they may be rotated or even incomplete. Therefore, calculate a set of corrections  $w$ , essentially an estimation of  $v$  at regularly spaced grid points. The  $w$ 's are defined at the pixels

$$\begin{array}{ccccccc}
 1,1 & 1, +1 & 1,2 +1 & \dots & 1, & & \\
 & & & & & & \\
 1+ , 1 & 1+ , 1+ & \dots & & & & (4.15) \\
 & & & & & & \\
 , 1 & \dots & & & & & , .
 \end{array}$$



The integers  $\mu$  and  $\nu$  are given by

$$\nu = 512./NSIDE + .5 \quad (4.16)$$

$$\mu = 512./MSIDE + 1.5 ,$$

where FORTRAN integer round-off conventions are assumed. Figure 4-8 illustrates the points at which  $\Delta w$  is defined.

To estimate the distortion  $\Delta w$  at the pixel  $(I,J)$  we locate the three vectors  $v$  which are nearest to  $(I,J)$ ,  $v(k_1)$ , and  $v(k_3)$ . These values of  $k$  are found by an exhaustive search. There is a unique plane which passes through the distortion at each point. This plane is determined and evaluated at  $(I,J)$  to obtain  $\Delta w(I,J)$ . In complex rotation,

$$av_k + b\bar{v}_k + c = \Delta v_k, \quad (4.17)$$

where  $a$ ,  $b$ , and  $c$  are complex. Substitution of the three pairs  $v(k_i)$ ,  $v(k_i)$  for  $i = 1,2,3$  into (4.17) yields three equations for the three unknowns  $a$ ,  $b$ , and  $c$ . The solutions are

$$\begin{aligned} a &= [\bar{v}_1 (\Delta v_3 - \Delta v_2) + \bar{v}_2 (\Delta v_1 - \Delta v_3) + \bar{v}_3 (\Delta v_2 - \Delta v_1)] / \det \\ b &= [v_1 (\Delta v_2 - \Delta v_3) + v_2 (\Delta v_3 - \Delta v_1) + v_3 (\Delta v_1 - \Delta v_2)] / \det \quad (4.18) \\ c &= [\Delta v_1 (v_2 \bar{v}_3 - \bar{v}_2 v) + \Delta v_2 (v_3 \bar{v}_1 - \bar{v}_3 v_1) + \Delta v_3 (v_1 \bar{v}_2 - \bar{v}_1 v_2)] / \det \end{aligned}$$

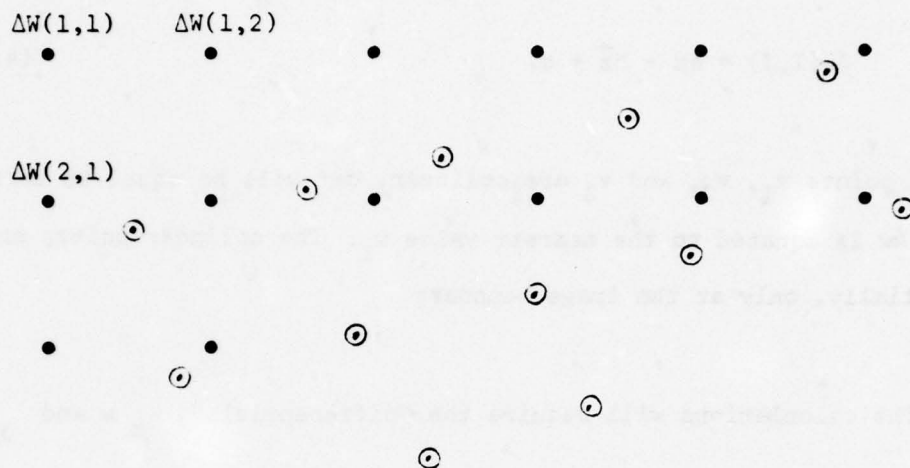


Figure 4-8 Points of Image where Distortion  $\Delta V$  (open circles) and  $\Delta W$  (dots) are Defined for a Typical Set of V's.

$$\det = (v_1 \bar{v}_2 - \bar{v}_1 v_2) + (v_2 \bar{v}_3 - \bar{v}_2 v_3) + (v_3 \bar{v}_1 - \bar{v}_3 v_1)$$

Then, if  $z$  is the complex number with  $I$  and  $J$  its real and imaginary parts,

$$\Delta w(I, J) = az + b\bar{z} + c. \quad (4.19)$$

If the points  $v_1$ ,  $v_2$ , and  $v_3$  are colinear,  $\det$  will be equal to zero. In this case,  $\Delta w$  is equated to the nearest value  $v_1$ . The colinear points are found, essentially, only at the image boundary.

The calculations will require the "differentials",  $\partial_x w$  and  $\partial_y w$ ,

$$\partial_x \Delta w(I, J) \equiv \Delta w(I + 1, J) - \Delta w(I, J) \quad (4.20)$$

$$\partial_y \Delta w(I, J) \equiv \Delta w(I, J + 1) - \Delta w(I, J)$$

#### Module 5

Given a pixel at  $(I, J)$ , Module 5 computes the distortion at  $(I, J)$  by interpolating between the four surrounding values of  $\Delta w$ . Recall that  $v$  is the number of pixels between the entries in the calibration table  $\Delta w$ . Define  $M$  and  $N$ , integers such that

$$Mv + 1 \leq I \leq (M + 1)v + 1 \quad (4.21)$$

$$Nv + 1 \leq J \leq (N + 1)v + 1.$$

Then the distortion at (I,J) is the linearly interpolated number

$$\begin{aligned} \text{dist}(I,J) = & \Delta w(M+1,N+1) C_1 + \Delta w(M+1,N+2) C_2 \\ & + \Delta w(M+2,N+2) C_3 + \Delta w(M+2,N+1) C_4 \end{aligned} \quad (4.22)$$

where

$$\begin{aligned} C_1 &= (v - l_x)(v - l_y)/v^2 \\ C_2 &= l_x(v - l_y)/v^2 \\ C_3 &= l_x l_y / v^2 \\ C_4 &= (v - l_x) l_y / v^2 \end{aligned} \quad (4.23)$$

These weights C are illustrated in Figure 4-9 which also shows that

$$\begin{aligned} l_x &= I - (Mv + 1) \\ l_y &= J - (Nv + 1) \end{aligned}$$

Inserting (4.23) into (4.22) we obtain

$$\begin{aligned} \text{dist}(I,J) = & \Delta w(M+1,N+1) + \partial_x \Delta w(M+1,N+1) l_x / v + \partial_y \Delta w(M+1,N+1) l_y / v \\ & + [ \partial_y \Delta w(M+1,N+1) + \partial_y \Delta w(M+2,N+1) ] l_x l_y / v^2 \end{aligned} \quad (4.24)$$

The 512x512 distortion map is written onto a file DBØ:CALMAP. Also, the diagonal of this distortion map is displayed.



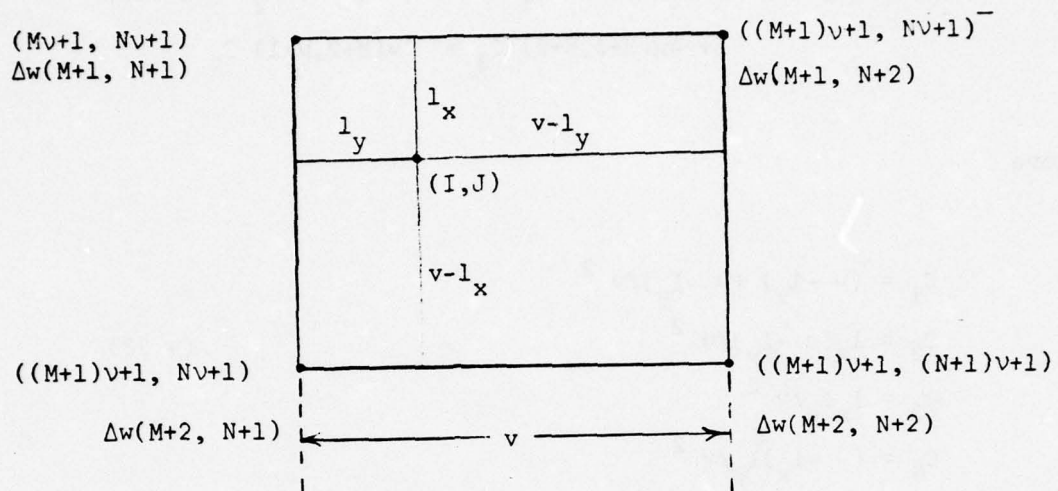


Figure 4-9 The Points  $\Delta w$  Used in the Interpolation to  $(I,J)$

## SEGMENT C

Segment C of EYECAL uses the distortion map calculated by Segment B to perform a correction. The input images to be corrected are stored on tape in IPS format. The corrected output images are written onto a second tape.

Segment C fills in pixels of the corrected image. Suppose we are correcting pixel (I,J). Then the distortion map at (I,J) has a complex value  $z$ . The gray level which should be at (I,J) has been carried by distortion onto  $(I + \text{Re}(z), J + \text{Im}(z))$ . We therefore want to move the gray level at  $(I + \text{Re}(z), J + \text{Im}(z))$  into pixel (I,J). Naturally, the components of  $z$  are not in general integers so  $(I + \text{Re}(z), J + \text{Im}(z))$  will fall between four pixels,  $g(I', J') = g_1$ ,  $g(I', J' + 1) = g_2$ ,  $g(I' + 1, J' + 1) = g_3$ , and  $g(I' + 1, J') = g_4$ . The new gray level at I,J is taken to be

$$g'(I,J) = g_1(1 - \partial_x)(1 - \partial_y) + g_2(1 - \partial_x) \partial_y + g_3 \partial_x \partial_y + g_4 \partial_x(1 - \partial_y), \quad (4.25)$$

where

$$\begin{aligned} \partial_x &= I + \text{Re}(z) - I' \\ \partial_y &= J + \text{Im}(z) - J' \end{aligned} \quad (4.26)$$

The main section of Segment C positions input and output tapes, copies the input file into a direct access file, and calls subroutine NEWPIX for each point,

$$g' = \text{NEWPIX} (I + \text{Re}(z), J + \text{Im}(z)).$$

The main section also is responsible for formatting of output and all other general job control functions. -

The function NEWPIX calls subroutine FIND to locate the gray levels which it needs to evaluate Equation 4.25. FIND(I',J',g,g') sets g to the gray level at row I' column J' in the input image; g' is set to gray level at row I', column J' + 1. Subroutine FIND always maintains ten rows of the input image in core. The array NROW denotes the rows of the image presently in core. NROW(K) is the row number of the Kth line in the buffer. FIND also keeps track of which line has been in core the longest. When a gray level from a line which is not in core is required, FIND reads in the line, storing the new line in the buffer position which had theretofore contained the oldest line in core.

## SECTION 5

### ERROR ESTIMATION AND REMOVAL IN MULTISPECTRAL IMAGE REGISTRATION

The result of image band registration, which directly affects the target classification, depends greatly on the operator's visual control point identification in different image bands. In order to learn how accurate such point transfer (PT) operations might be, experiments were designed to estimate the error introduced during point transfer with digital images.

Because our digital image data were prepared by separately scanning positive films of individual image bands, error introduced during band registration was due to the following:

1. Hardware error, especially due to the cursor control,
2. Intra-band visual point transfer error due to orientation and/or translation,
3. Inter-band visual point transfer error due to grey level difference caused by sensor differences, film developing and processing, etc.

The experiments here show that cursor control error was estimated to be 0.46 pixel in the vertical and 0.58 in the horizontal directions in the center part of the monitor screen, with different error characteristics. Median intra-band point transfer error was estimated to be between 1.11 and 1.22 pixels. The largest inter-band point transfer error occurred between visible bands and the IR band, the median of which was estimated to be between 2.26



and 2.98 pixels. Cursor control, intra-band and inter-band PT error in visible bands can be eliminated by local correlation techniques provided by the image registration routine. However, inter-band error between visible band and IR band cannot be eliminated without preprocessing. -

Section 5.1. estimates the cursor error. Section 5.2. is devoted to describe our experiment in estimating intra-band visual PT error. Section 5.3. describes the inter-band visual PT error estimation. Section 5.4. shows the cursor and intra-band PT error reduction by using local correlation techniques. Section 5.5. shows the result of using local correlation techniques to reduce inter-band PT error and Section 5.6. concludes the findings with a recommended registration procedure under DICIFER.

To avoid confusion in notation, capital letters X, Y, R are used in this section to represent random errors in the row (or vertical direction with respect to the monitor screen), column (or horizontal direction with respect to the monitor screen) and radial directions, respectively. Greek small letters  $\mu_x$ ,  $\sigma_x^2$  are used for the population mean and variance of random variable X. Random variables  $\bar{X}$  and  $S_x^2$  are used for sample mean and variance, where  $\bar{X} = \frac{1}{n} \sum X_i$ ,  $S_x^2 = \frac{1}{n-1} \sum (X_i - \bar{X})^2$ , with sample size n.

#### 5.1. CURSOR CONTROL ERROR ESTIMATION

DICIFER interfaces a cursor control box (made by Spatial Data Systems, Inc., Model 804-2) to a 12" diagonal Sony Trinitron color monitor. The cursor control box consists of a joystick which enables the operator to move

a bright point on the monitor screen and an enable/disable switch which interrupts the computer to accept the (row, column) location value of the bright point. Because of the instability of the cursor (visually, one can see a bright spot joggling around the selected location), the location repeatability is very poor. Therefore, software was designed to accept the first interrupted location value and to ignore the following ones. An additional shortcoming of this cursor is that it is very difficult to pin down points at the edges of the monitor screen, especially at the four corners.

Error estimation was based on the data collected from the central part of the monitor screen. It is expected that larger errors will occur at the edges. A 200 x 200 image was displayed on the central part of the 12" diagonal monitor screen occupying approximately 5" in both directions. Six points were selected randomly on the image, one at a time. After one point was selected, the enable/disable switch was turned on and off four times to accept location values of this point at time intervals of approximately 3 to 5 seconds. Table 5-1 lists the four recorded (row, column) values per point; 0.46 pixel average absolute difference was encountered in row (the vertical) direction and 0.58 pixel in column (horizontal) direction. Further analysis shown in the Table indicates that the two errors are uncorrelated.

Examining these numbers, it was found that no even row values appeared. The absence of even row values was confirmed after we re-examined the recorded (row, column) values in the other tasks. On the other hand, the cursor control changes the pixel coordinates more frequently in the column direction than in the row direction, as shown in the Table. This indicates that error

Table 5-1 Cursor/Control Error Estimation

Point ID						
Value ID	1	2	3	4	5	6
1	(149,67)	(57,52)	(17,17)	(41,223)	(81,25)	(163,147)
2	(147,66)	(57,51)	(17,18)	(41,222)	(81,23)	(163,148)
3	(147,67)	(57,52)	(17,16)	(41,222)	(79,24)	(161,147)
4	(147,66)	(57,51)	(17,18)	(41,223)	(79,23)	(161,148)
Mean	(147.5,66.5)	(57,51.5)	(17,17.25)	(41,222.5)	(80,23.75)	(162,147.5)
Mean Absolute Differ- ence x , 4	(0.75,0.5)	(0,0.5)	(0,0.75)	(0,0.5)	(1,0.75)	(1,0.5)
# Changes	(1,3)	(0,3)	(0,3)	(0,2)	(1,3)	(1,3)

$$\Sigma |x| = 2.75$$

$$\Sigma |y| = 3.5$$

$$\bar{x} = 0$$

$$\bar{y} = 0$$

$$\Sigma x_i y_i = 2.0$$

$$S_x^2 = 0.478$$

$$S_y^2 = 0.370$$

$$S_{xy} = 0.198$$

$$H_0: \sigma_x^2 = \sigma_y^2 \text{ is accepted at 5\% level}$$

$$H_0: \rho_{xy} = 0 \text{ is accepted at 5\% level}$$

characteristics are different in these two directions. More quantitative analysis would be required to completely model this function.

#### 5.2. INTRA-BAND POINT TRANSFER ERROR

Digital data was obtained by (LIPS) scanning transparencies of individual bands separately. Therefore, the orientation of the digital images were not identical in different bands. It was estimated that a  $10^\circ$  difference would be maximum. To perform image registration, visual point identification error due to orientation difference must be considered. This error was estimated by using images generated by a multi-channel scanning system.

The major concern of the study is to quantitatively estimate the radial error during visual intra-band point transfer. However, because of the operational procedure, it is interesting to know qualitatively whether radial error is affected by the relative orientation, the order of point selection and the image nature. To serve the latter purpose, a non-additive three-factor repeated model was used and an experiment was designed accordingly. The data obtained were used to quantitatively estimate the radial error.

One image of 10 bands over the Griffiss Air Force Base, NY, was used to conduct this study. Subimages of size  $150 \times 150$  were taken from the image and rotated  $5^\circ$  and  $10^\circ$  counterclockwise. Six subjects experienced with the



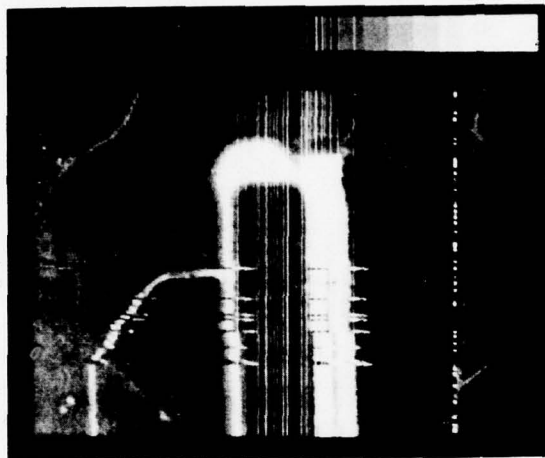
image registration routine were selected to identify three control points in subimage pairs which are of the same band but with different orientation. The results show that quantitatively, median radial error (including cursor control error) is between 1.11 and 1.22 pixels. Qualitatively, image relative orientation does affect the radial error. The following subsections describe the experiment in more detail.

#### 5.2.1. Experiment Design

##### 5.2.1.1. Data Preparation

One image of ten (10) bands over the GAFB, NY, was used as the subject of this experiment. The image was generated by a multispectral scanner with  $100^\circ \pm 10^\circ$  field of view and 2.5. milliradians instant field of view. Therefore, there are at most 767 usable pixels per scan line. Four bands (B3:  $5150 \pm 500 \text{ \AA}$ , B4:  $5600 \pm 500 \text{ \AA}$ , B7:  $6800 \pm 400 \text{ \AA}$ , B9:  $8150 \pm 900 \text{ \AA}$ ) were chosen because their bandwidths are closest to those of the P1 filters. Six  $200 \times 200$  subimages were taken from the image. These subimages were rotated  $5^\circ$  and  $10^\circ$  counterclockwise, pivoting at (row, column) = (100, 1), using one option in the image registration routine. The  $150 \times 150$  subimages were then taken from these rotated subimages to form a  $6 \times 3 = 18$  image data bank. Figure 5-1 shows one set of these  $150 \times 150$  subimages. Three of these subimages contain mainly man-made objects with high contrast (Figures 5-1a through 5-1c), and the other three contain mainly rivers, cultural fields, etc., with generally poorer contrast (Figures 5-1d through 5-1f). Figure 5-1a was taken from Band 3, Figures 5-1b and 5-1d were taken from Band 7, Figure

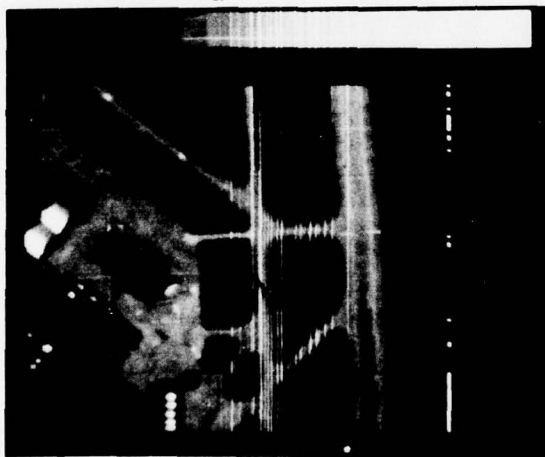
Figure 5-1 Digital Images Used for Visual Intra-band PT Error Study  
(600 x 600 pixels)



a



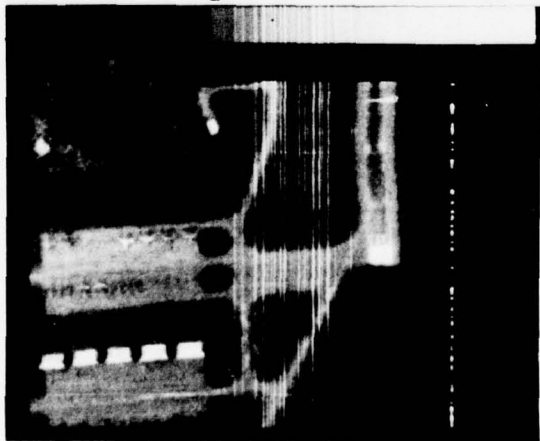
d



b



e



c



f

5-1c was taken from Band 4 and Figures 5-1e and 5-1f were taken from Band 9.

The 18 images in the data bank formed 90 image pairs with respect to their relative orientation (i.e., identical orientation, 5° clockwise, 5° counterclockwise, 10° clockwise and 10° counterclockwise).

#### 5.2.1.2. Subject Selection

Six experienced DICIFER users were selected to perform the digital image point transfer experiment. Four were employees of PAR. The other two were RADC staff. They are all familiar with the registration routine under DICIFER and have extensive experience in digital image processing.

#### 5.2.1.3. Subject-Image Pair Assignment

Subjects were divided into two groups. Subjects in different groups viewed different image pairs. Each subject was to view 15 pairs of images. Subjects were to select three points in the first image of the image pair and then to identify the same points on the second image. The image pairs were randomized so that the subject would not see the same relative orientation in any two successive pairs, or four different orientations of the same image in sequence.

### 5.2.2. Equipments

#### 1. Hardware

- o 12" diagonal Sony Trinitron Color Monitor
- o Cursor Control, Spatial Data Systems Inc., Model 804-2
- o DEC PDP 11/20 computer with RP02 Disk Drive
- o Tektronix 4010-1 Console

#### 2. Software

- o Image Registration Routine and some display routines under DICIFER.

### 5.2.3. Experiment Procedure

#### 5.2.3.1. Experiment Preparation

- o The size of the image on the monitor was adjusted so that a 150 x 150 digital image occupied approximately 3.7" in the vertical direction and 3.8" in the horizontal direction.
- o The subjects were allowed to adjust the viewing distance, the brightness and the contrast of the image appearing on the monitor. They were allowed to examine the images as long as they desired, and were permitted to examine two images side by side (a display option under DICIFER) to determine the locations of corresponding



control points. They were also allowed to replace selected points by new, more satisfactory points.

#### 5.2.3.2. Data Collection

- o Image registration routine was used to display successive images on the TV monitor and to display (row, column) values on the Tektronix of points selected through the cursor control.
- o After the experimenter submitted the necessary information to the image registration routine, a new image was displayed on the TV monitor. It takes approximately 20 seconds to complete the display. The routine rings a bell when the display is finished. Time was recorded when the experimenter heard the bell ( $T_1$ ).
- o The subject then selected three (3) points on the image through the cursor control. The returned (row, column) values of these points were displayed on the Tektronix. The routine also rings the bell whenever a value from the cursor control is received. The approximate time of the last bell was also recorded ( $T_2$ ).  $T_2 - T_1$  was the approximate time duration required by the subject to select or to identify three control points.
- o The three (row, column) pairs were recorded by the experimenter, together with  $T_1$  and  $T_2$ . The process repeats until all predesignated

images were displayed. (In this experiment there were 30 images or 15 image pairs viewed per subject.)

#### 5.2.3.3. Error Calculation

The subject name, experiment date, approximate experiment starting and finishing time, image ID, point selection starting and finishing time, and point (row, column) values were keypunched on cards. A FORTRAN program was written to transform the (row, column) values of points in the second image of the image pair to the corresponding (row, column) values in the first image according to their relative orientation. The Euclidean distance between the transformed values and the subject-identified values was calculated for each point. Table 5-2 summarizes the result.

#### 5.2.3.4. Data Analysis

Euclidean distance errors were summarized in Table 5-2. Several huge errors, enclosed in parentheses, were probably caused by subjects' confusion in point identification. These errors can be practically eliminated by recording approximate point positions on sketches of the images. Therefore, these errors were replaced by the average error in the same image nature and orientation. For instance, 7.38 in image 2, 5° CCW was replaced by the average of the other 26 errors in images 1, 2, and 3, with 5° CCW.

Table 5-2 Euclidean Distance Error Summary ( $e_i$ )

Image Nature	Orientation Point Order Subject Image ID			0°			5° CW			5° CCW			10° CW			10° CCW			Σe <sub>i</sub>	Σe <sub>i</sub> .2
				1 2 3			1 2 3			1 2 3			1 2 3			1 2 3				
				1	2	3	1	2	3	1	2	3	1	2	3	1	2	3		
H I C H  C O N T R A S T	1	2.00	1.00	1.00	2.61	2.77	1.16	1.39	1.81	0.92	2.11	0.47	1.07	2.11	1.85	1.52	23.79	43.888		
		0.0	1.0	0.0	0.49	1.99	0.93	1.38	0.94	1.02	1.26	0.88	1.52	1.00	1.72	0.76	14.89	19.102		
		2.0	2.0	0.0	0.41	1.39	0.37	1.25	0.87	0.82	1.42	1.00	1.27	1.23	1.51	0.43	15.97	21.836		
	2	2.24	2.24	0.0	0.87	1.29	3.64	1.36	1.29	2.56	1.92	0.64	3.00	0.70	1.33	1.97	25.05	55.009		
		0.0	1.0	1.0	1.11	1.39	0.34	1.38	0.87	1.90	0.97	1.51	0.52	1.33	0.84	0.99	15.21	18.563		
		0.0	0.0	1.0	1.64	1.63	1.71	0.73	1.46	1.03	1.30	1.34	1.13	1.19	2.39	2.08	18.63	29.213		
	3	1.00	2.00	0.00	0.86	1.11	1.74	2.05	0.97	1.31	0.76	1.09	2.60	0.68	1.45	2.66	20.28	35.025		
		0.00	1.00	0.00	1.11	0.58	0.90	1.49	2.72	1.53	0.89	0.52	0.35	0.74	0.41	2.13	14.37	21.776		
		1.00	2.24	0.00	2.24	0.86	1.90	0.65	3.22	0.40	1.78	1.61	1.64	0.95	0.51	1.42	20.42	37.965		
L O W  C O N T R A S T	4	1.0	1.0	1.0	1.68	0.85	0.61	1.29	1.56	1.64	0.96	2.32	1.97	3.87	2.17	2.10	24.02	47.985		
		0.0	2.0	1.0	0.55	2.41	1.56	0.54	0.61	0.62	0.90	0.76	0.27	1.52	0.76	2.20	15.70	23.781		
		0.0	1.0	0.0	0.67	0.53	1.23	0.39	0.53	1.23	1.32	1.58	0.64	0.32	1.72	0.47	11.63	13.119		
	5	2.0	1.0	1.0	1.63	0.72	0.55	2.35	1.33	1.06	0.92	1.21	0.35	0.90	0.33	0.61	16.04	21.767		
		1.0	2.24	1.0	0.72	0.12	0.87	0.08	1.20	0.51	2.84	0.95	1.38	1.18	0.45	3.92	18.46	37.848		
		0.0	0.0	2.0	0.72	0.10	0.40	0.76	2.26	1.42	0.92	0.60	0.25	0.92	1.92	0.95	13.22	19.094		
	6	0.0	1.0	2.0	2.69	1.74	2.45	0.62	2.39	0.95	0.61	1.14	0.94	1.45	0.40	0.78	19.17	33.711		
		0.0	2.0	1.0	0.53	1.23	1.93	1.08	1.83	0.59	1.90	1.37	0.48	1.41	1.38	0.48	17.21	25.222		
		0.0	0.0	0.0	0.60	0.99	1.51	0.61	1.15	0.53	0.57	0.98	2.77	2.05	2.13	2.77	16.66	30.966		
																		320.72	535.87	

The results of analysis of variance (Table 5-3) show that:

1. There is significant difference for distance errors due to image orientation.
2. There is no significant difference for errors due to image nature nor due to point ordering.

Further analysis show that interactions among these three factors are not significant.

In order to determine the radial PT error quantitatively, a probability model was proposed as follows:

Let  $X$  be the visual PT error in the row direction and  $Y$  be that in the column direction. Furthermore, assume  $X$  and  $Y$  are statistically independent random variables, with normal distribution  $N(0, \sigma_x^2)$ ,  $N(0, \sigma_y^2)$  respectively. Then we have

$$f(x,y) = \frac{1}{2\pi\sigma_x\sigma_y} \exp \left\{ -\frac{1}{2} \left( \frac{x^2}{\sigma_x^2} + \frac{y^2}{\sigma_y^2} \right) \right\}, \quad -\infty < x,y < \infty.$$

By defining  $x = r \cos\theta$ ,  $y = r \sin\theta$   $0 \leq \theta < 2\pi$ ,  $0 \leq r < \infty$ , the probability of the random variable  $R < r$  where  $R$  is the error in the radius direction is



$$\Pr(R < r) = \int_0^r f_r(r) dr, \quad \text{where}$$

$$f_r(r) = \int_0^{2\pi} \frac{r}{2\pi \sigma_x \sigma_y} \exp \left\{ -\frac{r^2}{2} \left( \frac{\cos^2 \theta}{\sigma_x^2} + \frac{\sin^2 \theta}{\sigma_y^2} \right) \right\} d\theta.$$

There is no closed form for  $f_r(r)$ . Without loss of generality, by assuming

$\sigma_y^2 < \sigma_x^2$ , we have

$$\frac{r}{\sigma_x \sigma_y} \exp \left\{ -\frac{r^2}{2 \sigma_y^2} \right\} < f_r(r) < \frac{r}{\sigma_x \sigma_y} \exp \left\{ -\frac{r^2}{2 \sigma_x^2} \right\}$$

Therefore

$$\int_0^r \frac{r}{\sigma_x \sigma_y} \exp \left\{ -\frac{r^2}{2 \sigma_y^2} \right\} dr < \Pr(R < r) < \int_0^r \frac{r}{\sigma_x \sigma_y} \exp \left\{ -\frac{r^2}{2 \sigma_x^2} \right\} dr$$

$$\text{or} \quad \frac{\sigma_y}{\sigma_x} \left\{ 1 - \exp \left( -\frac{r^2}{2 \sigma_y^2} \right) \right\} < \Pr(R < r) < \frac{\sigma_x}{\sigma_y} \left\{ 1 - \exp \left( -\frac{r^2}{2 \sigma_x^2} \right) \right\}$$

Let  $\Pr(R < r\alpha) = \alpha < 1$ , we have

$$\frac{\sigma_y}{\sigma_x} \left\{ 1 - \exp \left( -\frac{r^2 \alpha}{2 \sigma_y^2} \right) \right\} < \alpha < \frac{\sigma_x}{\sigma_y} \left\{ 1 - \exp \left( -\frac{r^2 \alpha}{2 \sigma_x^2} \right) \right\}$$

$$\text{or} \\ \sqrt{2} \sigma_x \sqrt{\ln \left( \frac{\sigma_x}{\sigma_x - \alpha \sigma_y} \right)} < r_\alpha < \sqrt{2} \sigma_y \sqrt{\ln \left( \frac{\sigma_y}{\sigma_y - \alpha \sigma_x} \right)} \quad \text{if } \alpha < \frac{\sigma_y}{\sigma_x} \\ \sqrt{2} \sigma_x \sqrt{\ln \frac{\sigma_x}{\sigma_x - \alpha \sigma_y}} < r_\alpha < \infty \quad \text{if } \frac{\sigma_y}{\sigma_x} \leq \alpha \leq 1$$

To use this result, first we have to check if  $x$  and  $y$  are correlated. Table 5-4 summarizes the calculations based on our experimental data. By taking  $\alpha = 0.5$ , (the median error),  $\sigma_x = S_x = 1.0838$ ,  $\sigma_y = S_y = 0.8849$ , we have

$$1.11 \text{ pixels} < r_{0.5} < 1.22 \text{ pixels}$$

In other words, we estimated that there is a 50% chance an operator can identify a point in two images within error  $r_{0.5}$ .

Further analysis shows that the inter-subject error difference is significant. The experimenter observed that the more time spent for the point transfer, the less error introduced. It seems desirable to provide pre-processing tools and operation procedures to assist the user in obtaining minimum error with least effort.

Since the image was taken at 9000' AGL with 6" focal length, maximum 110° FOV and 2.5 milliradian IFOV, the estimated ground median error, at 50%, will be between 11.27 meters and 12.39 meters. This result is slightly

Table 5-3 ANOVA Table for Intra-band Visual PT Error Analysis

<u>Source</u>	<u>DF</u>	<u>Sum of Squares</u>	<u>Mean Square</u>	<u>F</u>	<u>Probability</u>
O (Orientation)	4	$SS_o = 7.9568$	1.9892	4.918	0.01 Sig.
P (Point Ordering)	2	$SS_p = 1.2429$	0.6214	1.052	N.S
I (Image Nature)	1	$SS_i = 1.0084$	1.0084	2.002	N.S
W (Within Cell)	8	$SS_w = 11.0699$	1.3837	-	-
OW	32	$SS_{ow} = 12.9431$	0.4045	-	-
PW	16	$SS_{pw} = 9.4534$	0.5908	-	-
IW	8	$SS_{iw} = 6.0306$	0.5038	-	-

$$SS_o = \sum_{o=1}^5 \left( \sum_{p=1}^3 \sum_{i=1}^2 \sum_{j=1}^9 x \right)^2 / 3*2*9 - C$$

$$SS_p = \sum_{p=1}^3 \left( \sum_{o=1}^5 \sum_{i=1}^2 \sum_{j=1}^9 x \right)^2 / 5*2*9 - C$$

$$SS_i = \sum_{i=1}^2 \left( \sum_{o=1}^5 \sum_{p=1}^3 \sum_{j=1}^9 x \right)^2 / 5*3*9 - C$$

$$SS_w = \sum_{i=1}^9 \left( \sum_{o=1}^5 \sum_{p=1}^3 \sum_{i=1}^2 x \right)^2 / 5*3*2 - C$$

$$\text{where } C = \left( \sum_{o=1}^5 \sum_{p=1}^3 \sum_{i=1}^2 \sum_{j=1}^9 x \right)^2 / 5*3*2*9$$

$$SS_{ow} = \sum_{o=1}^5 \sum_{j=1}^9 \left( \sum_{p=1}^3 \sum_{i=1}^2 x \right)^2 / 3*2 - SS_o - SS_w - C$$

$$SS_{pw} = \sum_{p=1}^3 \sum_{j=1}^9 \left( \sum_{o=1}^5 \sum_{i=1}^2 x \right)^2 / 5*2 - SS_p - SS_w - C$$

Table 5-3 (Cont'd)

$$SS_{iw} = \sum_{i=1}^2 \sum_{j=1}^9 \left( \sum_{o=1}^5 \sum_{p=1}^3 x \right)^2 / 5 \cdot 3 - SS_i - SS_w - C$$

$$F_o = MS_o / MS_{ow}$$

$$F_p = MS_p / MS_{pw}$$

$$F_i = MS_i / MS_{iw}$$



Table 5-4 Intra-band Visual PT Error Estimation

Data:

$$\begin{aligned}
 n_x &= n_y = 270 \\
 \sum x_i &= -5.78 & \sum y_i &= -3.72 & \sum x_i y_i &= -19.4707 \\
 \sum x_i^2 &= 316.0894 & \sum y_i^2 &= 210.7176 \\
 \bar{x} &= -0.02141 & \bar{y} &= -0.01378 \\
 S_x^2 &= 1.1746 & S_y^2 &= 0.7831 \\
 S_x &= 1.0838 & S_y &= 0.8849 & S_{xy} &= -0.0755
 \end{aligned}$$

where 
$$S_x = \frac{1}{n-1} \{ \sum x_i^2 - n\bar{x}^2 \} \quad S_{xy} = \frac{1}{n} \frac{\sum x_i y_i - n\bar{x}\bar{y}}{S_x S_y}$$

Analysis:

1.  $H_0: \mu_x = 0$  Accepted at 5% level by testing  $t = \frac{\bar{x} - \mu_x}{S_x / \sqrt{n}}$

Student t with n-1 d.f.  $t = -0.3246$

2.  $H_0: \mu_y = 0$  Accepted at 5% level by testing  $t = \frac{\bar{y} - \mu_y}{S_y / \sqrt{n}} = -0.2558$

3.  $H_0: \rho_{xy} = 0$  Accepted at 5% level by consulting Table X, p. 498,  
N. Johnson and F. Leone, Statistics and Experimental  
Design, Volume I, 1964

4.  $H_0: \sigma_x^2 = \sigma_y^2$  Rejected at 5% level by testing  $F = S_x^2 / S_y^2$  :  
F - distribution with  $n_x - 1, n_y - 1$  d.f. ( $F = 1.50$ )

Table 5-4 (Cont'd)

Estimation at 5% significance level:

$$-0.151 < \mu_x < 0.108 \quad -0.107 < \mu_y < 0.080 \quad -0.23 < \rho_{xy} < 0.03$$

$$2.44 < \sigma_x^2 < 4.26 \quad 1.63 < \sigma_y^2 < 2.84$$

larger than that reported as 9 meters in [14], in a study reported by Raytheon in 1974. However, with limited sample size and lack of their raw data, it is difficult to justify whether the difference is statistically significant.

### 5.3. INTER-BAND POINT TRANSFER ERROR

Band 11 (sensor wavelength = 800 - 1300 nm) was added to Bands 3, 4, 7 and 9 to conduct this study. The images were not rotated. Six (150 x 150) subimages of a scene were used. One analyst selected 3 points in Band 3 of each subimage (for a total of 18 points) and attempted to identify these points in the other four bands. Three of the total 18 points were unidentifiable in Band 11. For this reason, only 15 test points were used. An analysis comparing the original 15 points (from Band 3) to the corresponding 15 points selected from each of the other bands (4, 7, 9, and 11) was performed.

Table 5-5 shows the recorded (row, column) locations of 15 points in each band. Table 5-6 summarizes the inter-band visual PT radial error estimation. It is obvious that the error increases as the band difference increases.

### 5.4. REMOVING CURSOR CONTROL ERROR AND INTRA-BAND PT ERROR

Image registration routine provides local correlation to mechanically find the best corresponding points in different images. Our study indicates that it is a powerful tool to remove error due to cursor control instability and visual intra-band point ambiguity.

Given window size  $(2n + 1) \times (2m + 1)$ , region size  $(2N + 1) \times (2M + 1)$ , pixel location  $P = (P_r, P_c)$  in the reference image  $F$ ,  $Q = (Q_r, Q_c)$  in the

Table 5-5 Recorded (Row, Column) Point Locations in Inter-Band PT Study

<u>Point ID</u>	<u>Band 3</u>	<u>Band 4</u>	<u>Band 7</u>	<u>Band 9</u>	<u>Band 11</u>
1	160,62	160,61	160,61	156,62	158,62
2	48,118	48,118	48,118	48,117	48,117
3	180,111	180,111	180,111	180,110	180,112
4	104,61	104,60	104,62	104,60	104,60
5	62,90	62,89	62,90	62,88	62,90
6	140,100	140,100	140,100	138,101	142,99
7	38,19	38,19	38,18	38,18	38,24
8	138,74	136,73	136,74	136,73	138,76
9	102,61	102,61	104,61	104,62	100,62
10	134,77	136,77	136,76	134,76	142,79
11	112,138	114,139	114,138	114,141	116,139
12	104,58	104,57	102,58	104,58	104,57
13	128,132	128,134	128,134	126,133	126,133
14	98,27	98,27	98,27	100,29	98,26
15	180,66	180,65	178,66	180,67	182,67



Table 5-6 Inter-Band Point Transfer Radial Error Estimation

Item	Bands (3,4)	Bands (3,7)	Bands (3,8)	Bands (3,11)
$\Sigma (x_i, y_i)$	(6,0)	(0,0)	(-4,1)	(10,9)
$\Sigma (x_i^2, y_i^2)$	(12,12)	(24,8)	(40,27)	(100,43)
$\Sigma x_i y_i$	2	-2	10	16
$(\bar{x}, \bar{y})$	(0.4,0)	(0,0)	(0.267,0.067)	(0.67,0.6)
$(S_x^2, S_y^2)$	(.686,.857)	(1.714,.571)	(2.781,1.924)	(6.667,2.686)
$(S_x, S_y)$	(.828,.926)	(1.309,.756)	(1.668,1.387)	(2.582,1.639)
$S_{xy}$	0.174	0.135	0.280	0.157
$H_0: \mu_x = 0$	Accepted	Accepted	Accepted	Accepted
$H_0: \mu_y = 0$	Accepted	Accepted	Accepted	Accepted
$H_0: \rho_{xy} = 0$	Accepted	Accepted	Accepted	Accepted
$H_0: \sigma_x^2 = \sigma_y^2$	Accepted	Rejected	Accepted	Rejected
50% radial* Error Range	(0.89,1.06)	(1.08,1.51)	(1.73,1.88)	(2.26,2.98)

$$* \sqrt{2 \sigma_2^2 \ln \frac{\sigma_2}{2 - .5 \sigma_1}} < \gamma_{.50} < \sqrt{2 \sigma_1^2 \ln \frac{\sigma_1}{\sigma_1 - .5 \sigma_2}}$$

where  $\sigma_1^2 = \min\{\sigma_x^2, \sigma_y^2\}$ ,  $\sigma_2^2 = \max\{\sigma_x^2, \sigma_y^2\}$   
and  $0.5 < \frac{\sigma_1}{\sigma_2}$

image G to be registered, two correlation formulas were provided by the image registration routine to find correlation values of

$$C_1(F(P), G(Q')) = \frac{\left\{ \sum_{i=-n}^n \sum_{j=-m}^m F(P_r + i, P_c + j) G(Q'_r + i, Q'_c + j) \right\}^2}{\left[ \sum_{i=-n}^n \sum_{j=-m}^m F(P_r + i, P_c + j)^2 \right] \left[ \sum_{i=-n}^n \sum_{j=-m}^m G(Q'_r + i, Q'_c + j)^2 \right]}$$

$$C_2(F(P), G(Q')) = \frac{\left\{ \sum_{i=-n}^n \sum_{j=-m}^m (F(P_r + i, P_c + j) - \bar{F})(G(Q'_r + i, Q'_c + j) - \bar{G}) \right\}^2}{S_F^2 S_G^2}$$

where  $F(i,j)$  is the grey level at point  $(i,j)$  in image F,

$$\bar{F} = \frac{1}{(2n+1)(2m+1)} \sum_{i=-n}^n \sum_{j=-m}^m F(P_r + i, P_c + j)$$

$$S_F^2 = \sum_{i=-n}^n \sum_{j=-m}^m (F(P_r + i, P_c + j) - \bar{F})^2$$

for all  $Q' = (Q'_r, Q'_c)$  in  $\left\{ Q_r - N, \dots, Q_r + N \right\} \times \left\{ Q_c - M, \dots, Q_c + M \right\}$ .

$C_1$  is called the unnormalized version and  $C_2$  is called the normalized version by the routine.

It is obvious from the formula that the correlation values calculated depend on the window size and the formula used. The highest correlation value obtained in each formula also depends on the region size in image G and, therefore, on the initial disposition between the pixel locations P and Q. With no a priori knowledge, the location  $Q'$  with highest correlation

value should be accepted as the transferred point P of image F in image G. The confidence of selecting this Q' depends on the correlation values returned for other points in the neighborhood region. We define the "sensitivity" of a correlation technique to be the ratio of the highest correlation value to the second highest correlation values. This intuitively suggests that the lower the ratio, the lower the confidence in selecting the point location with highest correlation value as the corresponding point.

To see how these parameters (window size, formula used) affect the resulting point selection and sensitivity, several experiments were performed. The next several subsections summarize the results.

#### 5.4.1. Correlation Formula Selection

Three questions arose when we compared the "performance" of the correlation formula.

1. Will the same location (Q') in the image G always be calculated?
2. If the same locations are always given, how can performance be further evaluated?
3. If the same locations are not always given, which ones are better than the rest?

Five points were randomly selected from the images used for visual intra-band point transfer study. Table 5-7 lists the (row, column) values

Table 5-7 Unnormalized vs. Normalized Correlation in Machine Point Transfer (PT)

Point Id	Machine PT					
	Visual PT		Unnormalized			Window Size
	(r,c)F	(r,c)G	(r,c)best	(r,c)2nd	Normalized (r,c)best (r,c)2nd	
1	(24,82)	(24,82)	(24,82)	(25,82)	(24,82)	5x5
2	(24,82)	(24,82)	(24,82)	(25,82)	(24,82)	7x7
3	(24,82)	(24,82)	(24,82)	(25,82)	(24,82)	9x9
4	(114,22)	(116,22)	(114,22)	(128,16)	(114,22)	5x5
5	(114,22)	(116,22)	(114,22)	(115,22)	(114,22)	7x7
6	(114,22)	(116,22)	(114,22)	(115,22)	(114,22)	9x9
7	(134,48)	(134,48)	(134,48)	(133,48)	(134,48)	5x5
8*	(64,59)	(78,61)	(78,61)	(78,62)	(78,61)	5x5
9	(56,12)	(56,12)	(56,12)	(59,11)	(56,12)	3x3
10	(56,12)	(56,12)	(56,12)	(68,6)	(56,12)	5x5
11	(56,12)	(56,12)	(56,12)	(67,6)	(56,12)	7x7
12	(56,12)	(56,12)	(56,12)	(67,6)	(56,12)	9x9
13	(56,12)	(53,12)	(56,12)	(67,6)	(56,12)	7x7
14	(56,12)	(53,12)	(56,12)	(66,6)	(56,12)	5x5
$\Sigma \text{ratio}$			14.134		18.07	
$\Sigma \text{ratio}^2$			14.27		24.77	
mean ratio			1.009		1.291	
$S_x$			0.00895		0.32155	

H<sub>0</sub>: No difference between techniques used

\*

There is 10° orientation between the two images.

reject

:

2.16

>

3.27

=

1.291 - 1.009

t =

$\sqrt{\frac{0.00895^2 + 0.32115^2}{14}}$



visually selected in image F, approximate (row, column) values visually selected in image G, (row, column) values and correlation ratio of the highest two points by using unnormalized and normalized formulas. Window sizes were 3x3, 5x5, 7x7, and 9x9, with sufficient region size.

From the table, we see that two methods give identical highest correlation points. However, there is significant difference between the sensitivity. (A t-test was used to test the difference, although the ratio may not be normal distribution.) Lower ratio intuitively refers to higher ambiguity in point identification in the other image. Therefore, the normalized correlation version was used to conduct our succeeding experiments.

#### 5.4.2. Window Size Effect in Local Correlation Calculation

Sixty points were selected from the images used for visual point identification. The normalized version was used with sufficient region sizes to examine the window size effect on machine point identification. Table 5-8 shows the result. Since the (r,c) values were rounded off by the registration routine to the nearest integer values, the machine outperformed visual point identification. However, visual point selection does help in reducing the machine's searching process for the "best" point. From the Table, almost all (r,c) values were picked up consistently regardless of window sizes. Those inconsistent ones could be the result of the grey level interpretation during image rotation, which smoothes the image.

The calculated (r,c)G values listed in Table 5-8 were derived as follows. The points selected by the test subjects from image F, were mathematically transformed using the known rotation transformation in order to obtain the "calculated" (r,c)G values.

Table 5-8a

Window Size Effect on Machine Point Transfer (PT) High Contrast Image Group

PT ID	Visual PT		Calculated	Machine PT		
i	(r,c)F	(r,c)G	(r,c)G	5x5	7x7	9x9
1	24,82	24,82	24,82	24,82	24,82	24,82
2	114,22	116,22	114,22	114,22	114,22	114,22
3	70,60	70,60	70,60	70,60	70,60	70,60
4	134,48	134,48	134,48	134,48	134,48	134,48
5	34,40	34,40	34,40	34,40	34,40	34,40
6	26,10	30,15	33.07,19.32	33,19	33,19	33,19
7	4,137	16,143	17.80,143.12	18,143	18,143	18,143
8	134,50	140,46	139.72,45.12	140,45	140,45	140,45
9	8,15	10,22	11.15,21.24	11,21	11,21	11,21
10	18,95	28,100	28.08,100.06	28,100	28,100	28,100
11	118,9	122,3	120.21,5.67	120,6	120,6	120,6
12*	16,54	22,59	22.52,59.39	23,59	23,60	23,60
13	66,115	78,116	77.65,115.80	78,116	78,116	77,116
14	120,13	124,9	122.55,9.48	122,10	122,10	122,10
15	70,5	70,6	72.05,5.87	72,6	72,6	72,6
16	18,104	28,110	28.87,109.03	29,109	29,109	29,109
17	16,75	34,84	33.14,84.87	33,85	33,85	33,85
18	112,26	118,19	119.17,19.95	119,20	119,20	119,20
19	64,59	78,61	77.63,60.78	78,61	78,61	78,61
20	128,51	140,42	139.77,41.79	140,42	140,42	140,42

21*	10,89	28,101	29.66,99.70	30,100	29,100	29,99
22*	24,5	30,16	28.86,14.55	29,15	29,14	29,15
23	30,37	40,44	433,45.02	40,45	40,45	40,45
24*	12,49	24,60	24.68,59.96	25,60	26,60	25,61
25	104,116	128,109	126.92,109.97	127,110	127,110	127,110
26	96,9	98,7	100.46,5.99	101,6	101,6	101,6
27	62,30	70,33	70.62,32.57	71,33	70,33	71,33
28	56,113	80,116	79.13,115.35	79,116	79,116	79,116
29*	116,21	122,14	122.24,14.33	122,15	123,15	123,15
30	38,36	46,42	48.03,42.65	48,43	48,43	48,43

\* Different (r,c) values returned by different window sizes.

Table 5-8a (Cont'd)



Table 5-8b

Window Size Effect on Machine Point Transfer (PT) Poor Contrast Image Group

PT	Visual PT		Calculated	Machine PT		
ID	(r,c)F	(r,c)G	(r,c)G	5x5	7x7	9x9
1	128,95	128,94	128,95	128,95	128,95	128,95
2	52,86	52,85	52,86	52,86	52,86	52,86
3	98,21	98,20	98,21	98,21	98,21	98,21
4	82,119	82,120	82,119	82,119	82,119	82,119
5	122,46	122,46	122,46	122,46	122,46	122,46
6	98,30	102,29	102.12,28.24	102,28	102,28	102,28
7	128,96	138,91	137.76,91.47	138,91	138,91	138,91
8	78,43	84,42	83.33,43.05	83,43	83,43	83,43
9	82,120	96,118	94.02,119.39	94,119	94,119	94,119
10	124,72	130,68	131.68,67.91	132,68	132,68	132,68
11	96,21	100,19	99.34,19.54	99,19	99,19	99,19
12	12,18	16,24	15.40,23.88	15,24	15,24	15,24
13	90,15	94,12	90.84,14.09	93,14	93,14	93,14
14	86,145	100,143	100.19,143.94	100,144	100,144	100,144
15	66,117	76,118	77.82,117.79	78,118	78,118	78,118
16	109,19	112,17	112.12,16.42	112,16	112,16	112,16
17	120,98	136,91	139.55,89.47	140,90	140,90	140,90
18	112,42	124,35	121.95,35.71	122,36	122,36	122,36
19	20,28	28,36	28.95,37.89	29,38	29,38	29,38
20	58,19	64,23	64.77,22.43	65,22	65,23	65,23



21*	24,115	46,123	47.96,122.88	48,123	48,123	46,123
22	94,22	100,19	100.75,19.13	101,19	101,19	101,19
23	70,119	96,118	93.96,118.83	94,119	94,119	94,119
24	128,29	136,20	135.45,20.12	136,20	136,20	136,20
25	18,28	26,38	26.94,38.24	27,38	27,38	27,38
26	28,120	50,127	52.77,127.11	53,127	53,127	53,127
27*	88,12	94,12	93.10,10.33	93,10	93,10	93,11
28*	28,134	56,142	55.20,140.89	55,141	55,141	54,141
29*	88,142	116,138	115.68,138.35	116,138	116,138	115,138
30*	36,137	64,142	63.60,142.46	64,143	64,142	64,142

\* Different (r,c) values returned by different window size.

Table 5-8b (Cont'd)

By defining the "sensitivity of correlation" as the ratio of the highest correlation value to the second highest value, Table 5-9 shows that qualitatively there is no significant sensitivity difference among different window sizes. We did not examine the 3x3 window size simply because of its small sample size. Table 5-9 also shows that there is no significant difference due to image quality.

From the above experiments, we see that cursor control error and intra-band visual point transfer error can be greatly reduced by using local correlation techniques. As a matter of fact, using local correlation can practically reduce identity points identification error to zero.

#### 5.5. INTER-BAND POINT TRANSFER ERROR REMOVAL BY LOCAL CORRELATION

Table 5-6 shows visual inter-band point transfer error defined by  $R = X^2 + Y^2$ . These points were submitted to a normalized correlation technique with window size 5x5. Table 5-10 shows the result. From the table, it is clear that the visual inter-band point transfer error was removed for band pairs (3,4) and (3,7), and was significantly reduced between bands 3 and 9 (2-tail test at 5% significance level indicates that

$$\frac{1.79 - 0.44}{\frac{67.1114 + 22}{15 \times 15}} = 2.15 > 1.96).$$

Table 5-9 Window Size Effect to Machine Point Transfer  
(x: ratio of the highest correlation value to  
that of the second highest)

Image	Window Size					
	5x5	7x7	9x9	Total		
Quality	$x_i$	$x_i^2$	$x_i$	$x_i^2$	$x_i$	$x_i^2$
High Contrast	39.07	53.6451	38.19	50.8736	38.19	51.9261
Poor Contrast	42.68	63.9940	43.78	69.9744	40.70	58.5911
Total	81.75	117.6391	81.97	120.8480	78.89	110.5170
					115.45	156.4448
					127.16	192.5595
					242.61	349.0043

Model:  $x_{ijk} = A + W_i + Q_j + (WQ)_{ij} + ijk$

$i = 1, 2, 3; \quad j = 1, 2 \quad k = 1, \dots, 30$

ANOVA Table

Source	d.f.	SS	MS	F
W(window size)	2	0.0984	0.0492	0.13 N.S.
Q(image quality)	1	0.7618	0.7618	2.01 N.S.
WQ	2	0.0812	0.0406	0.11 N.S.
Residual	174	66.0651	0.3797	
Total	179	67.0065	0.3743	

Table 5-10 Intra-Band Error Removal By Local Correlation

PT ID	Band 3 (r,c)F	Band 4 (r,c)G		Band 7 (r,c)G		Band 9 (r,c)G		Band 11 (r,c)G	
		Visual	Machine	Visual	Machine	Visual	Machine	Visual	Machine
1	160,62	160,61	160,62	160,61	160,62	156,62	*160,59	158,62	157,64
2	48,118	48,118	48,118	48,118	48,118	48,117	* 50,115	48,117	49,115
3	180,111	180,111	180,111	180,111	180,111	180,110	180,111	180,111	180,112
4	104,61	104,60	104,61	104,62	104,61	104,60	104,61	104,60	107,58
5	62,90	62,89	62,90	62,90	62,90	62,88	62,90	62,90	62,92
6	140,100	140,100	140,100	140,100	140,100	138,101	140,100	142,99	139,101
7	38,19	38,19	38,19	38,18	38,19	38,18	38,19	38,24	36,21
8	138,74	136,73	138,74	136,74	138,74	136,73	138,74	138,76	137,74
9	102,61	102,61	102,61	104,61	102,61	104,62	102,61	100,62	102,61
10	134,77	136,77	134,77	136,76	134,77	134,76	134,77	142,79	145,76
11	112,138	114,139	112,138	114,138	112,138	118,139	112,138	116,139	119,138
12	104,58	104,57	104,58	102,58	104,58	104,58	104,58	104,57	105,61
13	128,132	128,134	128,132	128,134	128,132	126,133	128,132	126,133	126,133
14	98,27	98,27	98,27	98,27	98,27	100,29	98,27	98,26	98,27
15	180,66	180,65	180,66	178,66	180,66	180,67	180,66	182,67	185,72
Mean Error	0.90	0.00	0.00	1.15	0.00	1.79	0.44	2.42	3.37
Sum	23.0352	0.00	0.00	32.0176	0.00	67.1114	22.00	118.1073	304.00
Error Square									



However, no significant error reduction occurs between bands 3 and 11 by using local correlation (2-tail test at 5%:

$$\frac{3.37 - 2.42}{\frac{118 + 304}{15 \times 15}} = 0.69 < 1.96).$$

Therefore, we cannot expect error reduction in image registration between Band 3 (visible blue) and Band 11 (near IR) by using local correlation without further preprocessing.

#### 5.6. CONCLUSION

We summarize the result qualitatively as follows:

1. The precision of inter-band image registration, under the current image registration routine, is affected by:
  - a. Visual inter-band point transfer error
  - b. Cursor control instability
2. Visual intra-band point transfer error is related to the orientation between the images and there is no significant difference due to image quality, as long as there is sufficient visual clue for point identification.
3. Local correlation technique is helpful in reducing visual intra-band point transfer and cursor control error. It can also be used selectively to reduce inter-band point transfer error.

4. In order to reduce point transfer error between visible bands and the IR band by the local correlation technique, preprocessing is required.

There are a number of questions that remain to be answered:

1. What will be the intra-band point transfer error due to image resolution, ground resolution, image nature due to seasonal change, atmospheric change, etc.?
2. Can parameters be changed to design new local correlation techniques for reducing inter-band point transfer error between visible and IR bands?
3. What kind of preprocessing is most efficient to transform the images so that local correlation techniques can be applied to reduced inter-band point transfer error?
4. How can these error estimations be applied to evaluate the performance of target classification?

As a result of this study, an inter-band image registration procedure under DICIFER is recommended as follows:

Step 1: "Range change" the images to enhance the image contrast so that control points can be visually detected more easily and more accurately.

Step 2: Use normalized version of the correlation option provided by the image registration routine to identify control points in different visual bands. This correlation option should be operated on the original image, instead of the range-changed version, to avoid distortion introduced during range-change. Window sizes 5 x 5 or 7 x 7, with a scanning range of 11 x 11 to 21 x 21 (depending on the local image complexity) are recommended.

Step 3: To register the IR band against the visual band, carefully examine the corresponding control points because there is no alternative to recommend at the present time for reducing the error.

Step 4: After registration, display the image bands one by one to visually examine the performance. If not satisfied, go to Step 2.

## SECTION 6

### SPECIAL PROGRAMS FOR DICIFER

Several algorithms which were added to the DICIFER system under this effort are described in this section. The reader is referred to the DICIFER user's manual [3,4] for further details of the system structures. Additional information on the algorithms presented here is to be found in a corresponding user's manual to be published separately from this document.

#### 6.1. CORRELATION-ASSISTED IMAGE REGISTRATION

The capabilities of the image registration light button option were expanded to aid the analyst in selecting registration control points. This aid is in the form of area correlation which is performed between data in the neighborhood of the reference image control point and data in the neighborhood of the input image control point. The neighborhood region on the input image is moved about so a set of correlation coefficients are computed for the corresponding pair of control points. The analyst is presented with a list of correlation coefficients along with their respective row, column position. With this information, the analyst can elect to retain the point originally selected, or replace it with a position having a higher correlation.

Since the correlations are performed in rectangular regions and since the images are not registered, there may be some question whether the area correlation coefficients would be misleading. Two methods of performing the



correlations are available. The first method uses the images as they are (or some appropriate substitutes), assuming that the rotational and scale misregistrations are minor; that is, the small rectangular regions around the control point pair are similar. The rotational and scale effects are a global problem rather than a local one. The other method assumes that the complete set of control points are reasonably accurate and registration is performed only on the neighborhoods of the control points. These neighborhoods are nearly in registration since the local effects of rotation and scale have been minimized. Then the correlations are performed and the positions converted back to the original image. A new set of control points then permits the analyst to continue as though the analyst had actually selected the points.

There is an option concerning which correlation coefficient the user wants to be computed. The two available options are the unnormalized cross correlation coefficient

$$\frac{(\underline{x} \cdot \underline{r})^2}{(\underline{x} \cdot \underline{x})(\underline{r} \cdot \underline{r})}$$

and the normalized cross correlation coefficient

$$\frac{(\underline{x}' \cdot \underline{r}')^2}{(\underline{x}' \cdot \underline{x}')(\underline{r}' \cdot \underline{r}')}$$

where  $\cdot$  represents vector dot product,  $\underline{x}$  and  $\underline{r}$  are the one-dimensional vector representations of the rectangular neighborhoods;  $\underline{x}'$  and  $\underline{r}'$  are simply a

shift of the x and r vector such that the mean of the components of both x' and r' are zero. The routine (ASCORL), used to compute these functions, was coded in assembly language in such a manner that the input data, x and r, may be either unsigned bytes or signed integer values. Several entry points were provided to also allow for FORTRAN compatibility, re-entry as required by core limitations on the data buffer, and for multiple correlations using a given reference vector, r.

## 6.2.       MODIFY DESIGN VECTOR FILE

An algorithm was added to DICIFER to enable the user to conveniently add vectors to a design vector file and to edit decision images. This algorithm is used after classification logic has been applied to an image and a decision image has been generated. In the event misclassifications have occurred, it may be desirable to incorporate representatives of the misclassified samples into the design set and to redesign the classification logic. The program described here provides the capability for the on-line analyst to perform this task conveniently and efficiently.

The program allows the analyst to specify the desired class-code symbol simultaneously to all pixels satisfying the following rule. Assign class code A to pixel p if, and only if, p is contained within the boundary of area file, F, and the classifier logic had previously labelled it as belonging to class B. Class symbols A and B, as well as the area file name F, are entered by the analyst at run time.

A light button option on DICIFER was created to enable the user to code a decision image file so that specific grey levels represent class symbols. This "class" image file is then used by another light button option to create a new vector file using a design and a test vector file as the source for the vector data. The design vector file is copied into the output vector file with a possible change in the class symbol (if the grey level is non-zero for the row, column associated with the vector, then it is used as the new class symbol). The grey level in the class image is zeroed as it is used. Any remaining non-zero elements in the "class" image are then used to identify those vectors from the test vector file to be included in the output vector file with the class symbol defined by the grey level. The resulting vector file is then available for further processing. Essentially, this program provides the capability to either change class symbols of specified vectors or to increase the size of the design vector file to include more samples and/or classes.

In addition to the above capability, the analyst may also edit a decision image in the interior of regions defined by area files. This editing is identical to that of the "element change" light button except that only the area file regions are affected (the analyst may zero the exterior of the area files if desired). The analyst would use this routine after he had decided not to pursue automatic classification further for that image.



### 6.3. RADIOMETRIC IMAGE CALIBRATION

Methods for calibrating images digitized by the Computer Eye device were investigated during this effort. In order to calibrate the Computer Eye System, the light intensity variation as a function of position over the light table would have to be identified.

There are too many variables to consider for radiometric calibration of the Computer Eye, both accidental and natural in nature, to determine the calibration parameters once and only once. Thus, it was recommended that the following procedure be set up to provide for the radiometric calibration.

Several calibration images are obtained at the same scanning session with all variables constant, including that portion of the light table to be used. Each of these images represents an image of the light table as imaged through different neutral density filters. These images are intended to be a sampling of the grey level transfer function applicable at each picture location at the time of digitization. As such, it can be assumed that absolute film density can be recovered from recorded intensity at any pixel position, since the responses due to different density filters have been measured.

An image generated from a neutral density filter is to have a theoretically expected grey level which is constant throughout the image. The calibration images then form a set of piecewise linear intensity functions; one function for each picture element in the image. Since the calibration images are to define piecewise linear functions, the expected grey level needs to be entered at run time. To minimize analyst interaction, the images must be



named in sequence (i.e., the 5th and 6th character must be numeric and in numerical sequence). Also, the actual grey levels of the calibrating images must be nondecreasing (relative to the naming sequence) at every picture element. Now, for a given image of film scanned during the session each grey level is compared with the actual grey levels of the calibrating images to determine which part of the piecewise linear function to use for the interpolation; the function values at the end points are the expected grey levels. The result of the interpolation is then stored as the calibrated grey level at that picture element. To minimize disk storage requirements, it is advised that the radiometric corrections be performed immediately following image scanning so the calibration images can be deleted as soon as possible.

#### 6.4. CHANGE IMAGE SCALE

This light button option provides the analyst with the ability to change the scale of an image utilizing noninteger scale transformations. Since the factor may have a fractional component, there is not an exact mapping from a picture position on the output image to a picture position on the input image. Thus, grey level interpolation or weighting is necessary. For a given grey level position for the output image, the corresponding picture element on the input image is computed. The grey levels of the four nearest picture elements are used to compute the grey level for the output image. It is noted that if a scale factor of .5 or less is used, then interpolation involving all the input image pixels are not used; in fact, a scale factor of .5 will just capture every other row and column. Also, a scale factor of 2 will not double the dimensions of the image, but rather be one

pixel less in each direction. This is because there is no image data available to perform the interpolation required to determine the grey levels for that last row or column.

#### 6.5. LINEAR IMAGE RESTORATION

Restoration techniques are methods which attempt the inversion of the degrading process of the object experienced in being imaged. It is clear that the success of the restoration attempt depends on the degree of degradation, the feasibility of the model and/or parameters proposed, and the effectiveness of the algorithm used. Details regarding an approach investigated during this study are presented here.

Let  $g(x,y)$  be the image of the object  $f(\zeta, \eta)$  which has been degraded by the linear operator  $h(x,y, \zeta, \eta)$  and with additive noise  $n(x,y)$  such that

$$g(x,y) = \iint_{-\infty}^{\infty} f(\zeta, \eta) h(x,y, \zeta, \eta) d\zeta d\eta + n(x,y)$$

If the impulse response of the point-spread function  $h(.)$  is spatially invariant, then we have

$$g(x,y) = \iint_{-\infty}^{\infty} f(\zeta, \eta) h(x-\zeta, y-\eta) d\zeta d\eta + n(x,y) \quad (6-1)$$

By taking the Fourier transform on both sides of Equation (6-1), one can apply the inverse filtering techniques to estimate  $f(\zeta, \eta)$  in the spatial frequency domain. The alternative is through an iterative deconvolution

process. In discrete form, the formula to estimate the k-th value of  $f(i,j)$  can be derived as

$$f^k(i,j) = f^{k-1}(i,j) - \beta \sum_{m,n=-W}^W h(m,n) f^{k-1}(i-m,j-n) - f^0(i,j) \quad (6-2)$$

subject to  $f^k(i,j) \geq 0$ ,  $h(m,n) \geq 0$ , where  $\beta$  is a proportional constant and  $f^0(i,j) = g(i,j) - n(i,j)$ , the original image intensity at pixel  $(i,j)$  with noise.

A more efficient one-dimensional implementation of Equation (6-2) was developed by P. Jansson [8] which adjusted  $\beta$  adaptively according to the behavior of  $f^{k-1}$  so that the convergence becomes faster. A copy of the program was purchased from the Quantum Chemistry Program Exchange at Indiana University. The program was converted from the IBMF codes to IBMEL codes to be accepted by PDP 11/45. Several coding bugs were removed and the program was applied to 9 consecutive rows (95 pixels per row) of a reconnaissance image of an airplane. Figure 6-1 shows the result after two iterations. Thus,  $h(m)$  was assumed to be a Gaussian distribution of 5 points (i.e.,  $W=2$ ). Because the algorithm uses a "smooth-deconvolution" technique, the head and the tail portions of the waveform are not significantly improved.

Finding the result from the one-dimensional version encouraging, a two-dimensional version was implemented for Equation (6-2). Two numbers are used to stop the iteration:

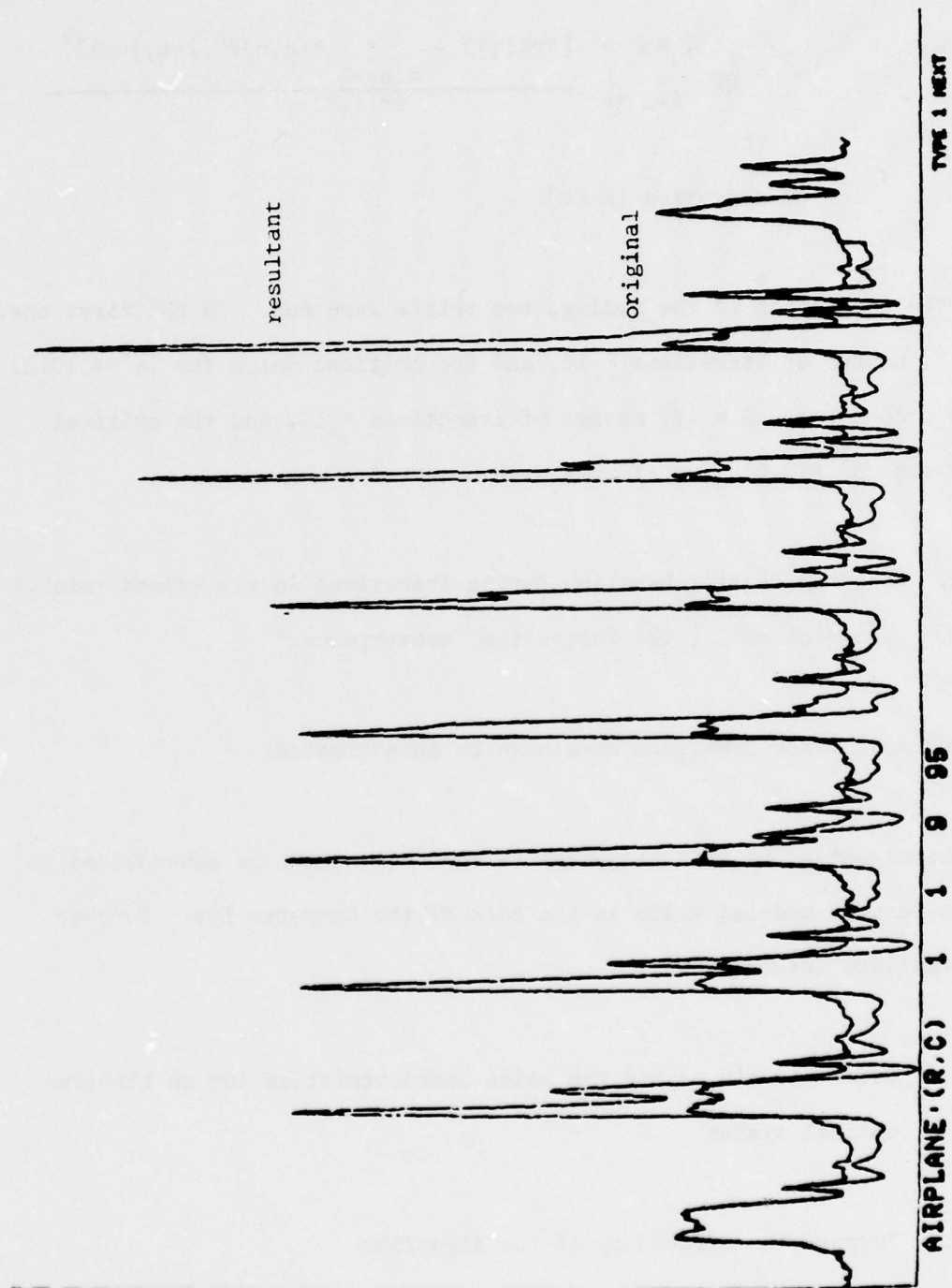


Figure 6-1 Results of Deconvolution Processing.



- (1) maximum number of iterations, and
- (2) critical value for the error norm

$$\sigma^2 = \frac{1}{MN} \sum_{i=1}^M \sum_{j=1}^N \frac{[f^0(i,j) - \sum_{m,n=-3}^3 h(m,n)f^k(i-m,j-n)]^2}{f^0(i,j)}$$

as suggested in [9].

After the completion of the coding, two trials were run. In the first one,  $\beta = .2$ , number of iterations = 10, and the critical value for  $\sigma^2 = 10.0$ . In the second one,  $\beta = .9$ , number of iterations = 10, and the critical values for  $\sigma^2 = 2.0$ . Two effects were observed:

1. The oscillating behavior during iterations in the second trial.
2. The smaller  $\beta$ , the faster the "convergence."

The causes of these behaviors remain to be investigated.

The advantage of this technique is that  $h(m,n)$  can be generalized to spatial variant models, which is the case of the Computer Eye. Further investigations are required to

1. Determine  $h(m,n)$  and the noise characteristics for an Electro-optical system
2. Improve the efficiency of the algorithm
3. Evaluate the performances of different restoration algorithms.

#### 6.6. IMAGE COMBINATIONS

This routine allows files to be combined on an element by element basis in a user-specified manner. Since this routine does not reject any data types, it is the user's responsibility to ensure that the files can meaningfully be combined. The acceptable file types are those which contain data in raster format such as image or Hadamard transform files. Also to be considered is the fact that image files are assumed to be in byte format while non-image files are assumed to be in word format.

The combination procedure is specified by the user via a set of "FORTRAN like" statements. For each element position in the file, the statements are applied. Therefore, an implied loop exists which encloses the statements entered. This loop is terminated when all file elements have been processed.

The acceptable statements are of the following two types:

IF (logical expression) IO = (arithmetic expression)

IO = (arithmetic expression) specifying the output grey level  
as a function of input grey levels.

The IF statement is identical in function to its FORTRAN counterpart except that when the logical expression is true the accompanying statement is executed and all ensuing statements are skipped for that element position in the

file. Also, the accompanying statement must be an assignment statement as shown. Several IF statements may appear.

The second statement type is the assignment statement which is identical to its FORTRAN counterpart. This statement type can only appear once, however, and it must be the final statement. When a statement of this type is entered, no further statements are accepted. Also, if a set of statements is entered which does not contain a final assignment statement, the statement  $IO=\emptyset$  is automatically appended.

The operators that are available for forming the logical and arithmetic expressions along with their order of execution are given in the following list:

<u>Operator</u>	<u>Priority</u>	<u>Description</u>
EXP(expression)	7	Exponentiation
LN(expression)	7	Natural log
LOG(expression)	7	Common log
-	6	Unary minus
*	5	Multiplication
/	5	Division
+	4	Addition
-	4	Subtraction
=	3	Equality test
<	3	Less than test
>	3	Greater than test

<= or =<	3	Less than or equal test
>= or =>	3	Greater than or equal test
<> or ><	3	Not equal test
	1	Logical AND
	0	Logical OR

The expressions indicated for the first three unary operators can be any legal arithmetic expression.

Arithmetic operations may be performed in fixed point (integer) or floating point mode. This should be considered when constructing the statements since fixed point operations execute considerably faster. The final compiled code performs the operations according to the operands involved. That is, for each operation performed in a statement, its mode (fixed or floating) is determined by the operand or operands involved. If at least one operand is real, the operation is performed in floating point mode. Any integer operands are converted to real prior to the operation. If all operands involved are integer, the operation is performed in fixed point. In many instances, floating point operations may be limited considerably by carefully ordering the sequence of operations. It should be noted that the unary operations EXP, LN and LOG are all performed in floating point. However, the expression upon which they operate is evaluated by the previously discussed procedure. If this expression yields an integer result, it is converted to real prior to application of the unary operator.



The order of operations is dictated by their priority. Higher priority operations are performed first in a left to right scan of the statement. This order can be altered through the use of parentheses. Up to 64 levels of parentheses are allowed.

Arithmetic operands specified in a statement can be either constants or file elements. Constants are entered as signed numbers (no sign is assumed positive). The type is assumed to be integer unless a decimal point is included in which case it is stored in real format. File elements are specified by the file from which they are to be taken. The files are referenced via the symbol I0, I1, I2, etc. Actual files are assigned to each symbol by the user at execution time. The first file should be referenced as I0 and each ensuing file by the next symbol in sequence. Symbols in the sequence should not be skipped.

The value returned by the statements is given by the symbol IO. This symbol must always appear in the statements as shown previously.

The following example is offered as an aid in understanding statement specification:

```
IF(I0 < I1)IO = EXP(I1 - I0)
```

```
IF(I0 > I1)IO = EXP(I0 - I1)
```

```
IO = 1
```

The effect of these statements is to compute the exponential of the absolute value of the difference between two files. The final statement handles the trivial case of exponentiating 0. In detail, for each element position within the files, the first is compared to the second. If the first is less than the second, the exponential of the second minus the first is computed and returned as the output value. If the first is not less than the second, the next statement is executed in a similar manner. In that statement, the file order is reversed. Only if the elements in the two files are equal, will the final statement be executed which forces the output to 1.

## SECTION 7

### PATTERN RECOGNITION EXPERIMENTS

#### 7.1. OVERVIEW

Experiments for automatic classification were initiated under this effort. The data utilized here was the 4-band multispectral photography over Stockbridge, New York. In particular, frame #125 from mission GR-74-58 was the subject of the experimentation. Figure 7-1 shows the four bands over this area. Figure 7-2 shows an enlargement of band 1 with Areas "1" and "2" outlined. Classification logic was designed on samples from Area 1 and tested against the remaining portions of that area. Once satisfactory performance was achieved the logic was further evaluated against Area 2. Good classification results were achieved on this data set as detailed below. Unfortunately, this work was completed at the end of the effort and we were not able to extend the results to a more diverse data set. Actually, attempts to do so were adversely affected by significant differences in intensity induced by atmospheric haze. Corrections for haze conditions were not performed during this effort.

#### 7.2. INTERACTIVE LOGIC DESIGN

The objective of this experiment was to design a classification logic which would separate camouflaged vehicles from the terrain background (medium to dense vegetation). Bare soil also covered a significant portion of the



Band 1



Band 2



Band 3



Band 4

Figure 7-1 Four band photography over Stockbridge Test Site. Frame #125 from Mission GR-74-58.



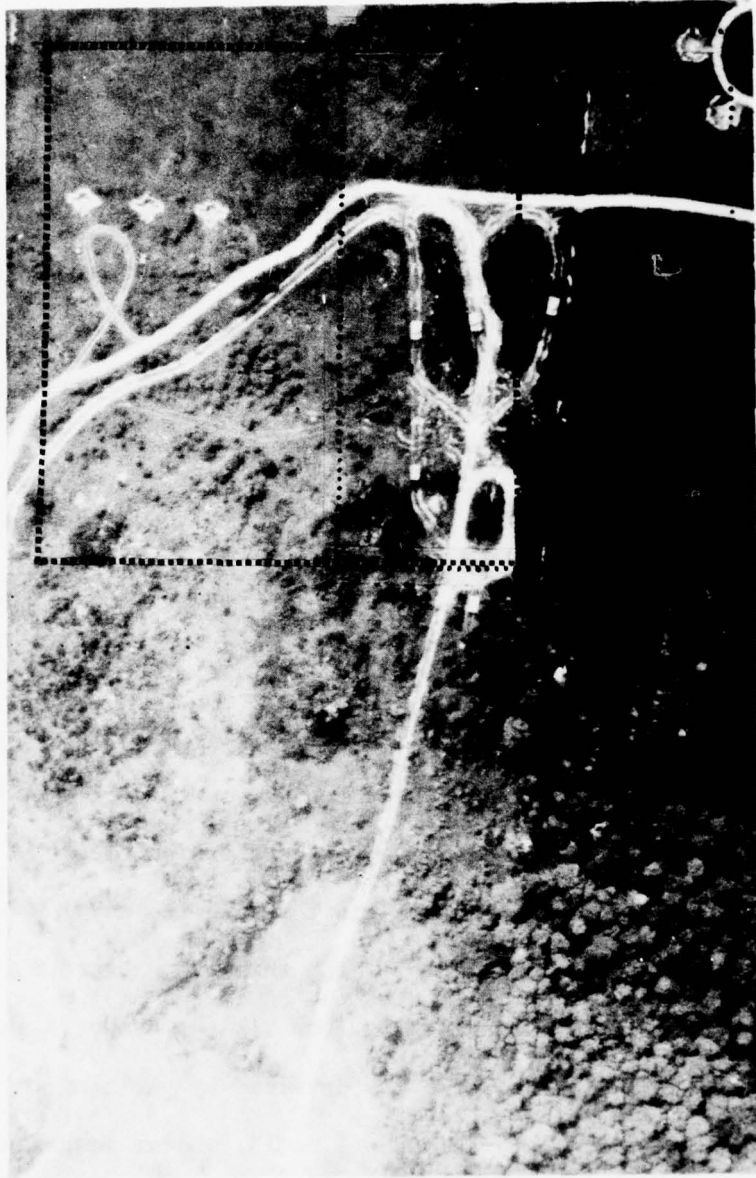


Figure 7-2 Band 1 Enlarged with Area 1 (Blocked Outline) and Area 2 (Dotted Outline) as Indicated.

area immediately surrounding certain of the tactical targets. The camouflaged (painted) targets included five M-48 tanks and three 3/4-ton trucks. Additionally, one of the 3/4-ton trucks was covered by camouflage netting.

Initially a five class problem was considered with samples taken of those types of vegetation with symbols U, V, and W, soil samples (S), and camouflaged vehicle samples (T). Also, a sample of coniferous vegetation was selected from Area "2". Figures 7-3 through 7-6 give the histograms (frequency of occurrence vs. grey level) for each class and each measurement. Plots such as these were utilized for vector data analysis.

#### 7.2.1. Structure Analysis

After analyzing the data, it was decided that some restructuring of the data would be helpful. In particular, on certain displays the T's would essentially cluster into two groups and, furthermore, certain of these were more likely to be confused with the coniferous vegetation samples (W). For these reasons it was decided to restructure the T's into two subclasses which were then labelled T and Q. The display on which this was performed is shown in Figure 7-7, with the boundary defining Q's from T's (as shown in large print) as illustrated. The display shown was obtained by plotting the vector on the Optimal Discriminant Plane for classes T and W. Later image analysis revealed that those vectors relabelled as Q corresponded to all the picture samples taken from the 3/4-ton truck which was covered by camouflage netting.

BEST AVAILABLE COPY

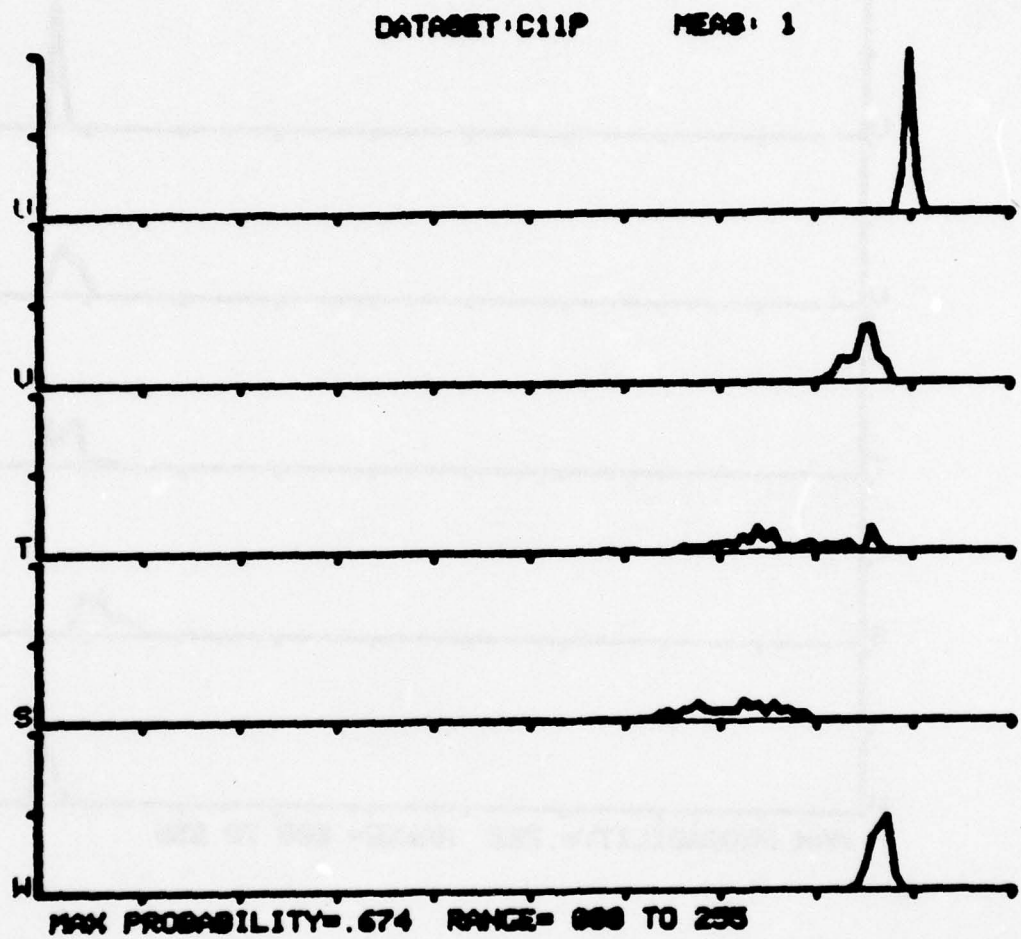


Figure 7-3 Histograms for Band 1 Samples.

BEST AVAILABLE COPY

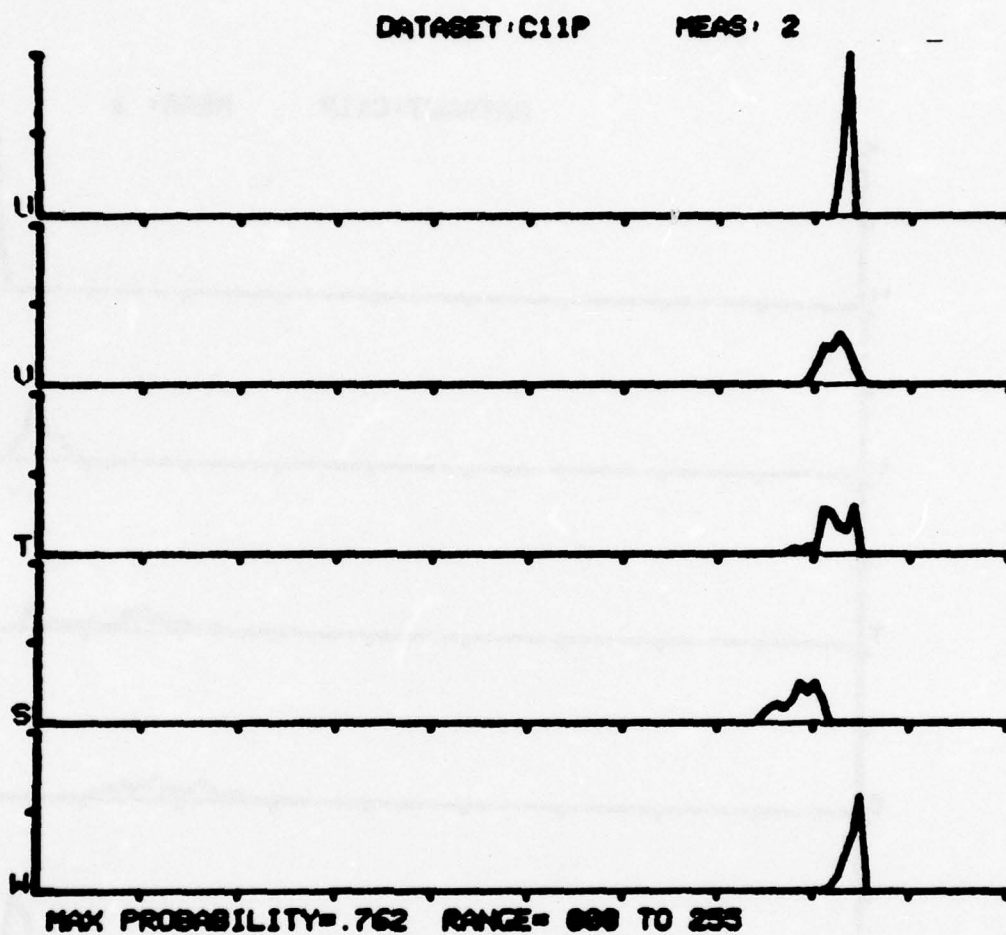


Figure 7-4 Histograms for Band 2 Samples.



BEST AVAILABLE COPY

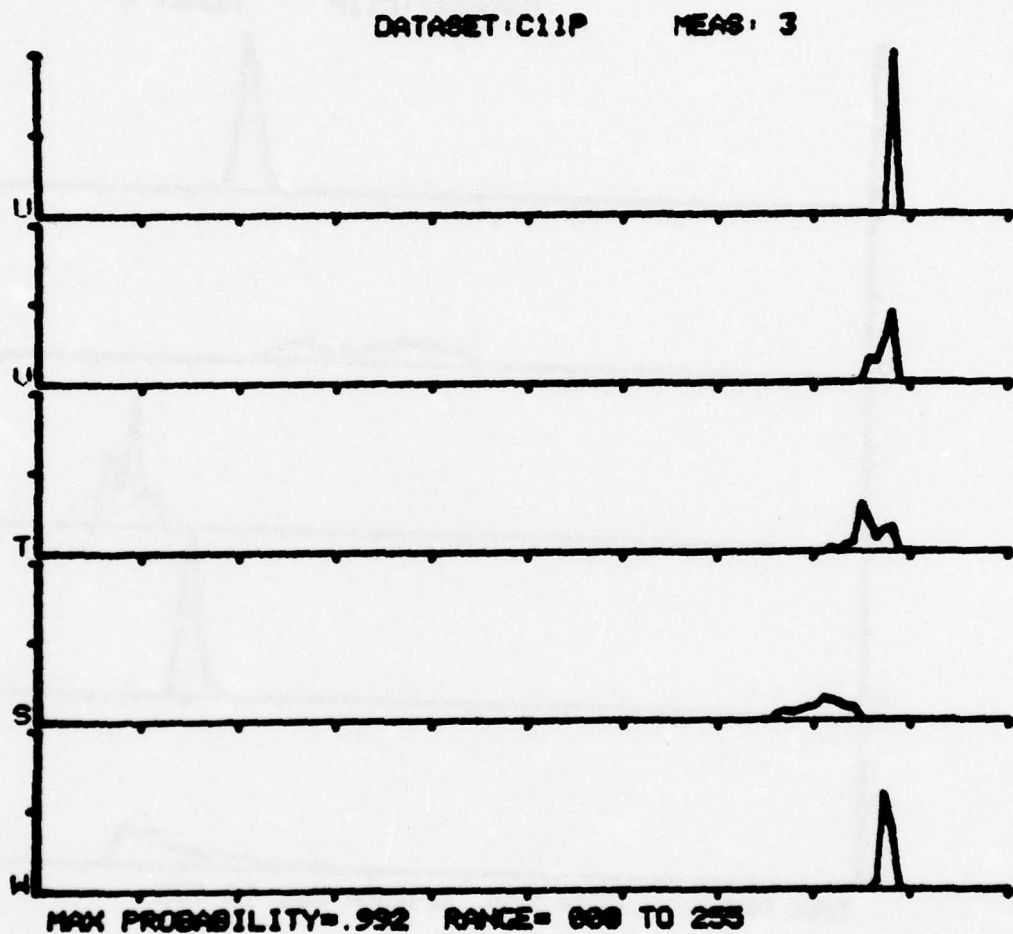


Figure 7-5 Histograms for Band 3 Samples.

BEST AVAILABLE COPY

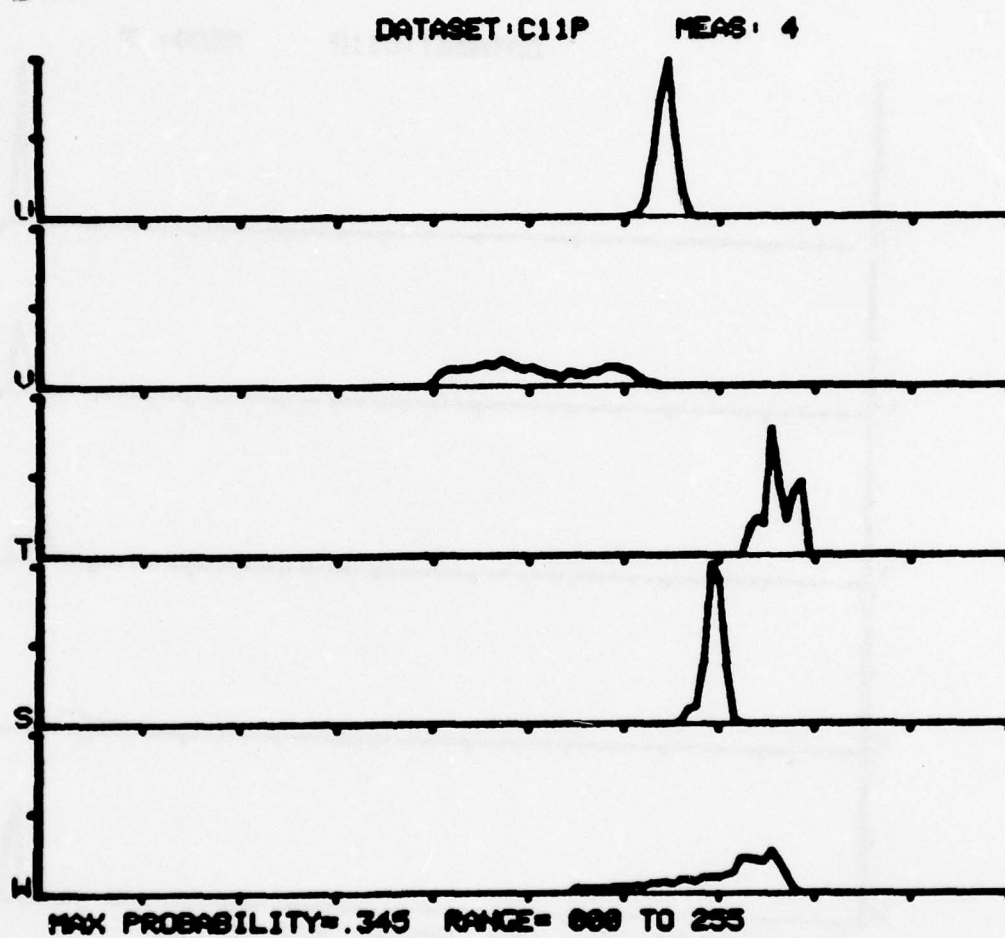


Figure 7-6 Histograms for Band 4 Samples.

BEST AVAILABLE COPY

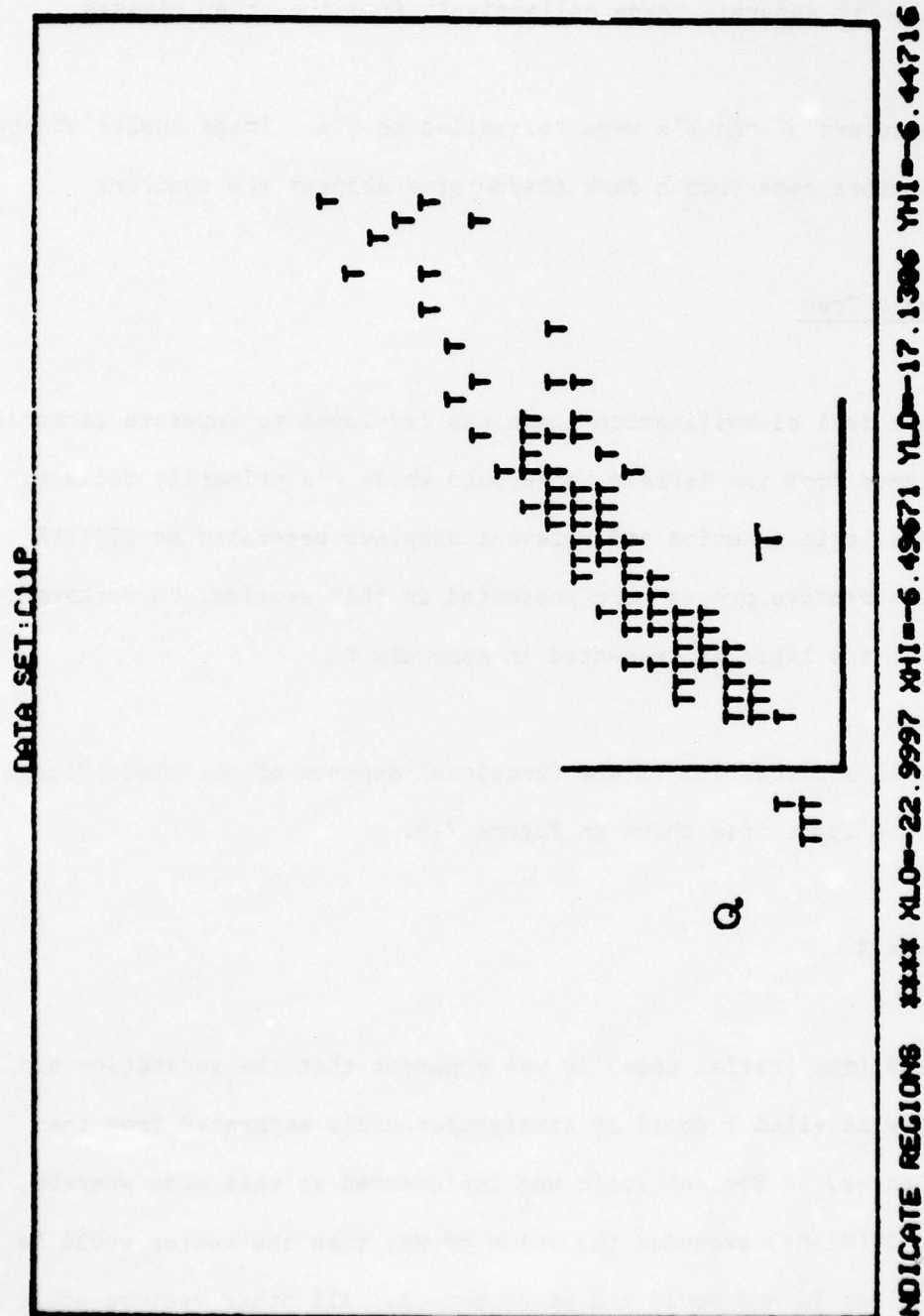


Figure 7-7 Optimal Discriminant Plane for Classes T and W  
Used for Restructuring T into Subclasses T and Q.

AD-A040 769

PATTERN ANALYSIS AND RECOGNITION CORP ROME N Y  
ADVANCED DIGITAL EXPLOITATION TECHNIQUES (ADET). (U)  
APR 77 G E FORSEN, F H FENG, M J GILLOTTE

F/G 15/4

UNCLASSIFIED

PAR-77-3

RADC-TR-77-145

F30602-75-C-0141

NL

3 OF 3

AD  
A040769



END

DATE  
FILMED  
7-77



Additional restructuring involved changing all the U's to V's, as it seemed possible to separate these collectively from the other classes.

Also, a subset of the W's were relabelled as X's. Image analysis showed that the X-vectors came from a dark shadow area amongst the conifers.

#### 7.2.2. Logic Tree

A hierarchical classification logic was developed to separate camouflaged tactical targets from the terrain background which was primarily foliage. An outline of the logic creation and relevant displays generated on DICIFER during the interactive process are presented in this section. A mathematical description of the logic is presented in Appendix F.

An overall appreciation of the functional aspects of the classification is given by the logic tree shown in Figure 7-8.

##### 7.2.2.1. Node $\emptyset$

At node  $\emptyset$  (the initial node) it was apparent that the vegetation samples which were now labelled V could be straightforwardly separated from the remaining classes. A Boolean logic was implemented at this node whereby, if the quantity  $5*(M1-M4)$  exceeded the value of  $M4$ , then the vector would be assigned to class V, and would end up at node 1. All other vectors would be passed to node 2. Here  $M_n$  is the grey value associated with band  $n$  ( $n = 1, 2, 3, 4$ ).

BEST AVAILABLE COPY

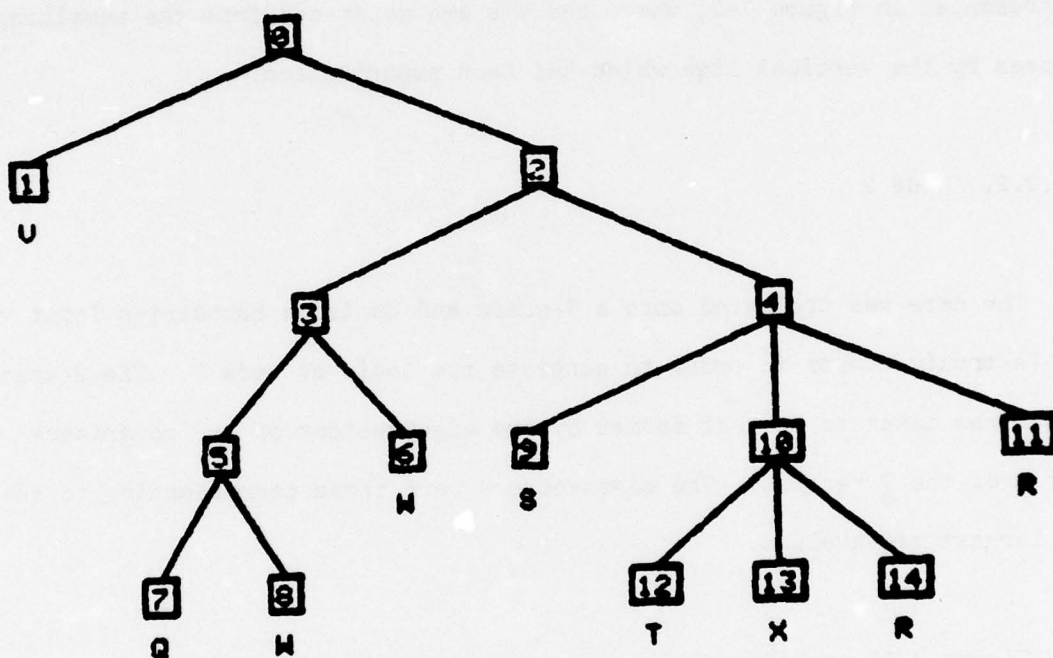


Figure 7-8 Logic Tree Showing Functional Description of the Hierarchical Classification Logic.

2, 3, 4). A representation of the distribution of all the samples with respect to the statement

$$5*(M1 - M4) > M4$$

is presented in Figure 7-9, where the V's are separated from the remaining classes by the vertical line which has been superimposed.

#### 7.2.2.2. Node 2

The data was projected onto a 2-space and decision boundaries input via the Tektronix cursor in order to generate the logic at node 2. The 2-space chosen was taken to be that formed by two eigenvectors of the covariance matrix of the T vectors. The eigenvectors were those corresponding to the two largest eigenvalues.

Figure 7-10 provides an illustration of the DICIFER display. The decision boundary is that indicated - one boundary containing two lines to separate the Q and W samples from the remaining samples. This process has created nodes 3 and 4 in the logic tree.

#### 7.2.2.3. Nodes 3 and 5

The Q samples were generally difficult to separate from the W samples, which would indicate that the additional camouflage netting was quite successful. At node 3 a two-space projection was created using two eigen-

BEST AVAILABLE COPY

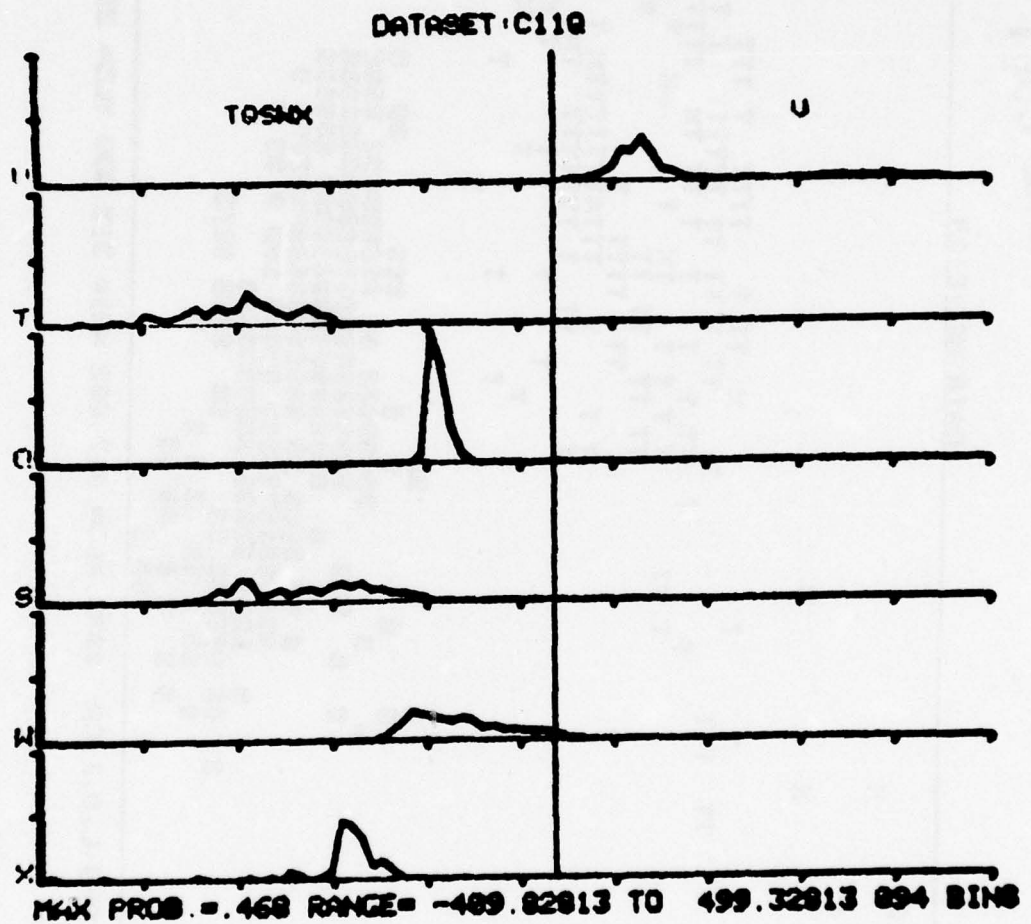
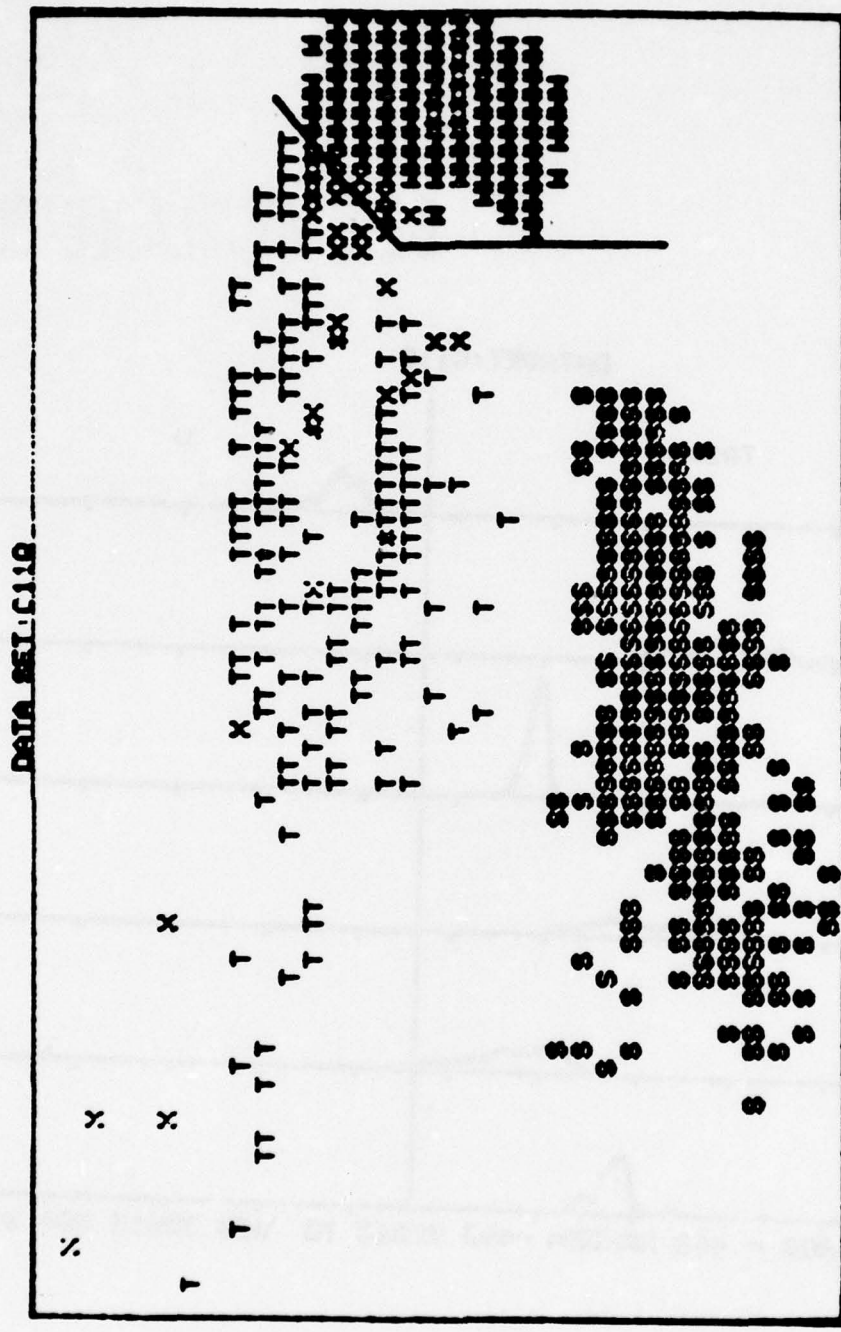


Figure 7-9 Node 0 Logic: Projection of Data to Illustrate Distribution of Samples with Respect to the Boolean Logic Statement.



BEST AVAILABLE COPY



OPTIONS: L.B.F.CR HHI= 217.662 MHI= 313.300 YLO= 250.941 YHI= 307.293

Figure 7-10 Node 2 Logic: Two-Space Eigenvector Projection of All Data at Node 2.

vectors of the Q-covariance matrix. The eigenvectors were those corresponding to the two largest eigenvalues. The decision boundaries are indicated in Figure 7-11. Notice that at node 3 we are only separating the Q samples and certain W's from the bulk of the W samples. This process created nodes 5 and 6 in the logic tree.

Further separation of the Q's from the W's at node 5 was attempted by performing a similar operation by projecting the data on an eigenvector plot corresponding to the 3rd and 4th largest eigenvalues of the Q-covariance matrix. This plot is shown in Figure 7-12. Decision boundaries were generated to enclose the Q vectors, although these also included certain W's (i.e., some false alarms were admitted). This created nodes 7 and 8 in the logic tree.

#### 7.2.2.4. Node 4 Logic

The classes remaining at node 4 include soil (S), target (T), and shadow area (X). Here, again, logic was defined by drawing boundaries on a two-space projection. On this plot (Figure 7-13) the horizontal axis represents the Fisher direction for classes T and S. The vertical axis represents measurement 4.

At this point the decision boundaries were designed to separate S from T and X. The remaining area of this plane was assigned the symbol R (refuse to classify).

BEST AVAILABLE COPY

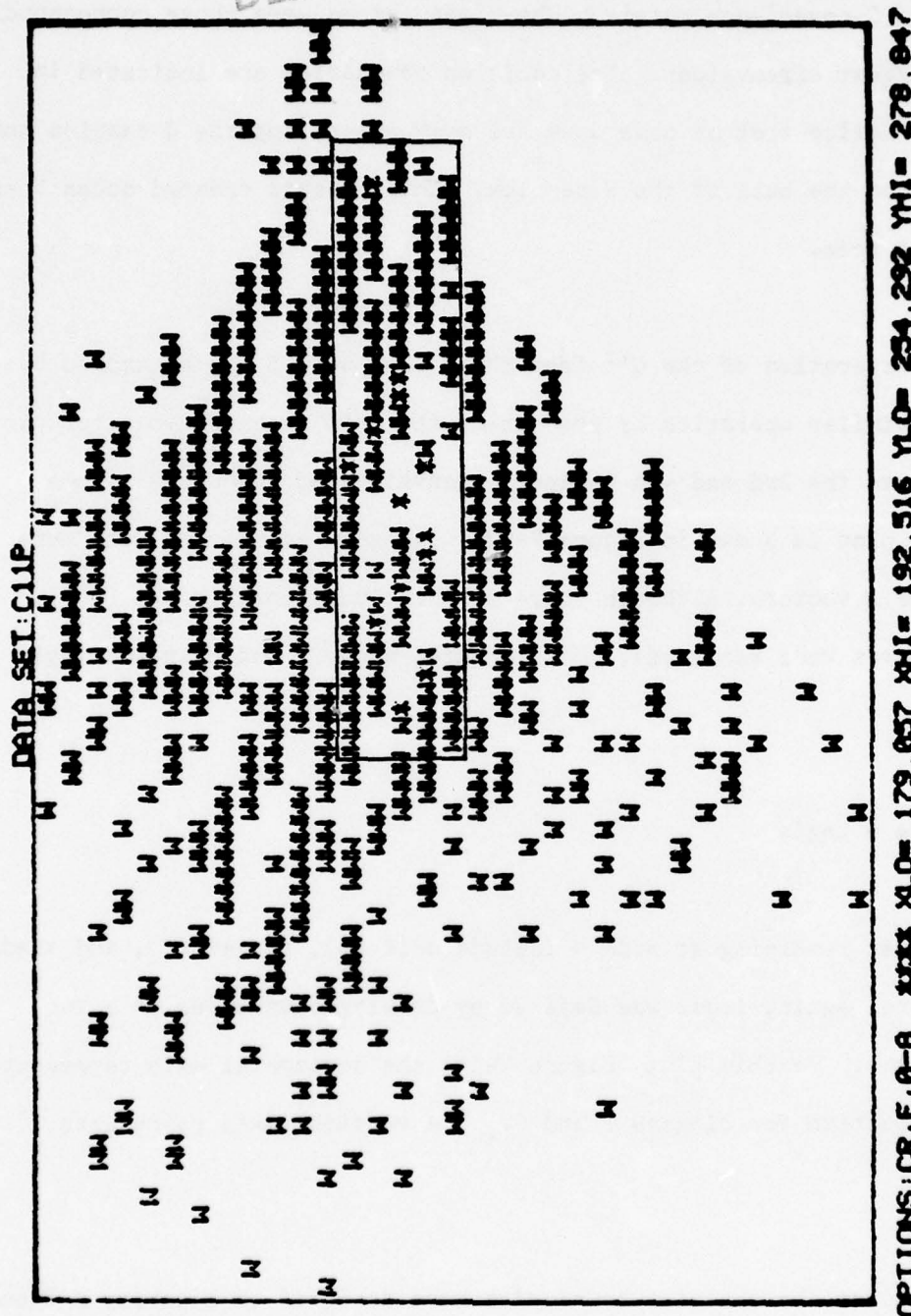


Figure 7-11 Node 3 Logic: Two-Space Eigenvector Projection of All Data at Node 3. \*'s Indicate Projection of Q and W Samples onto Same Coordinate.



DATA SET: C11P

INDICATE REGIONS

XLO= 189.172 XHI= 185.369 YLO= 191.877 YHI= 199.863

Figure 7-12 Node 5 Logic: Two-Space Eigenvector Project of all Data at Node 5.



BEST AVAILABLE COPY

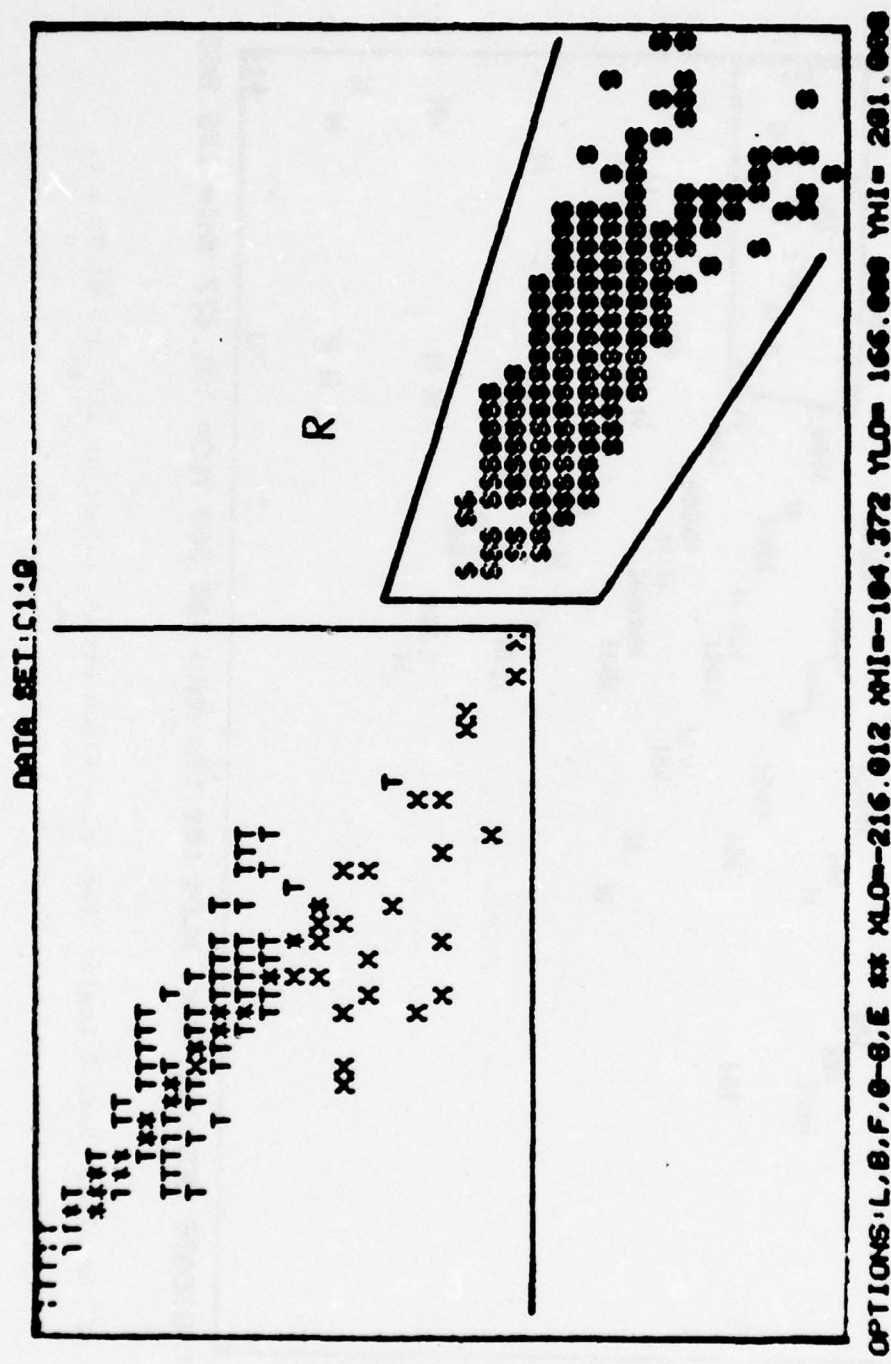


Figure 7-13 Two-Space Projection of Data at Node 4. The Horizontal Axis Represents the Fisher Direction for Classes T and S. The Vertical Axis Represents Measurement 4.

#### 7.2.2.5. Node 10 Logic

It remains to differentiate between T and X at node 10. The Optimal Discriminant Plane projection for classes T and X is shown in Figure 7-14. Decision boundaries were drawn to separate T from X with the remaining portion of the plane being assigned to R.

#### 7.3. LOGIC EVALUATION

The logic described above was evaluated against the design set, with the results as shown in Table 7-1. All but one of the T's have been correctly classified; the exception was assigned to the reject (R) category.

Also note that approximately 1/3 of the W samples were assigned to the vegetation category. No attempts were made to avoid this as the W corresponded to a "vegetation" category (coniferous).

Next the logic was applied to the images for Area "1" and Area "2". Good results were achieved as is evidenced by the decision images presented in Figures 7-15 and 7-16, respectively. The very bright points correspond to targets. The intermediate grey corresponds to soil and the darkest grey to vegetation. Black was assigned to the reject category but these are few and difficult to see in the photographs presented here.

Because of the great differences introduced by the atmospheric haze condition, we were not able to successfully apply this logic to other scenes.

BEST AVAILABLE COPY

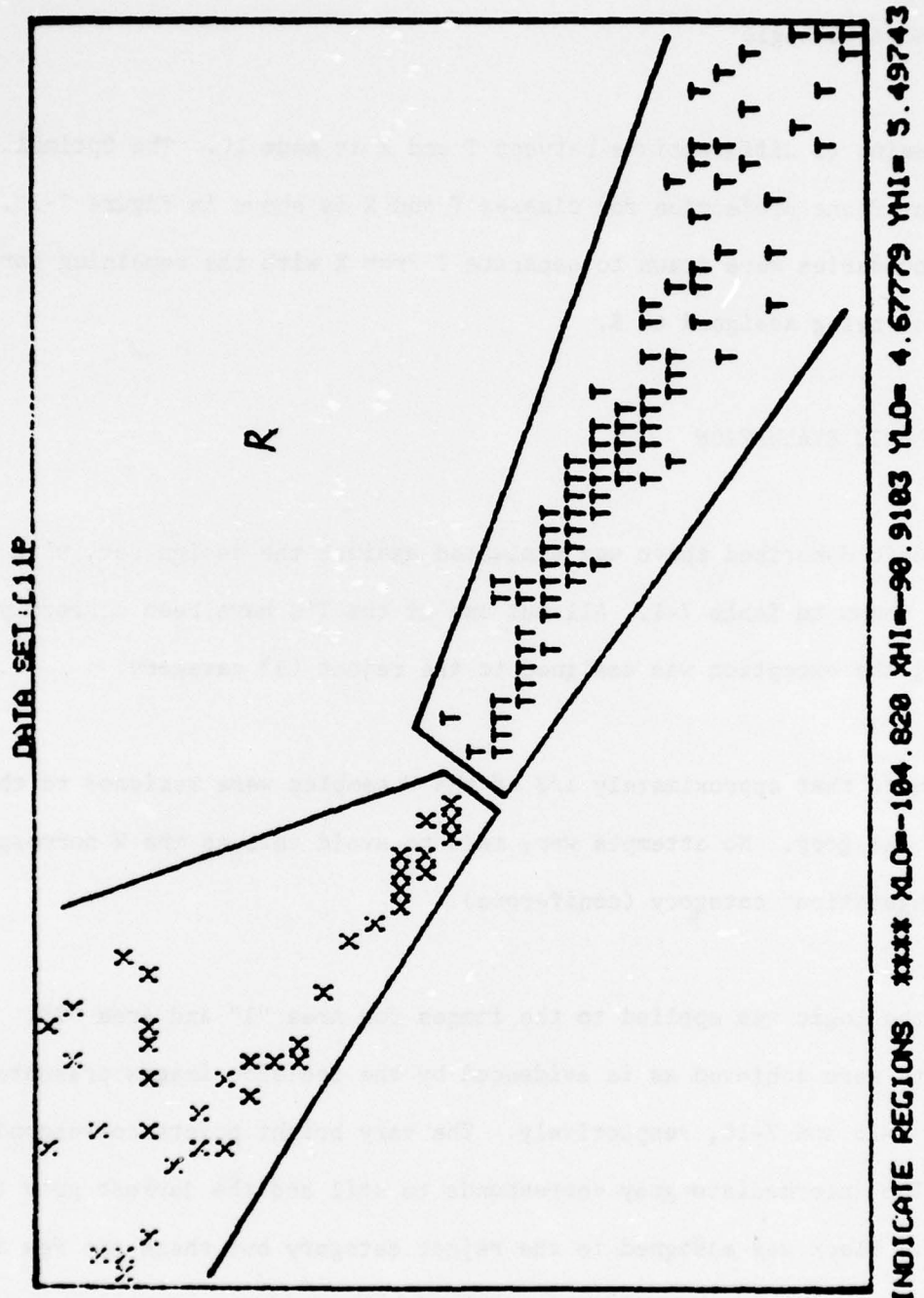


Figure 7-14 Node 10 Logic: Two-Space Projection (Optimal Discriminant Plane) for All Data at Node 10.

Assigned Classes (via Classification Logic)

	V	Q	W	S	T	X	R
V	10297	0	0	5	0	0	0
Q	0	31	1	0	0	0	0
W	1332	19	2510	0	0	1	0
S	0	0	0	611	0	0	0
T	0	0	0	0	221	0	1
X	0	0	0	0	0	53	9
R	0	0	0	0	0	0	0

Labelled Classes  
(Image Truth)

Table 7-1 Confusion Matrix for Design Set Vector File.





Figure 7-15 Decision Image for Area 1.

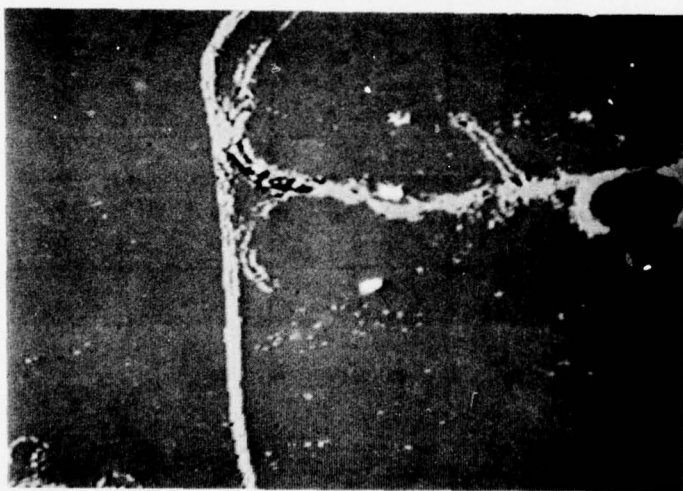


Figure 7-16 Decision Image for Area 2.

The extendability of the classification logic to other times and places remains untested. As an interesting by-product of this experimentation, it appears that the vector structure analysis capabilities of DICIFER provide an interesting approach toward analyzing the benefits of different types of camouflage techniques. That is, data samples from various camouflaged vehicles may be easily compared to samples of different types of vegetation. Determinations might then be made as to the best camouflage/vegetative background match.

#### REFERENCES

1. Trossbach, J., This reference will be made available to qualified military or government representatives on request from RADC/IRRE, GAFB, NY 13441.
2. Haynes, R., "Project Compass Trip," RADC-TR-74-176, August 1974.
3. Forsen, G.E.; Lietz, J.C.; et al., "Image Feature Extraction System (IFES)," RADC-TR-74-291, (A002878), November 1974.
4. Lietz, J.C.; et al., "Advanced Multispectral Descriptor System (AMIDS)," RADC-TR-74-346, 1975, Volume I, (A007007), Volume II, (A008196).
5. Zanon, A.; Gillotte, M.; and Zoracki, M., "Spectral Analysis," RADC-TR-75-302, March 1976, (A024209).
6. Zoracki, M.; Forsen, G.; "Digital Image Processing Techniques for Automatic Terrain Classification for Generating Reference Maps from B/W Aerial Photography," RADC-TR-76-196, June 1976, (ADB013135L).
7. Wenderoth, S.; Yost, E., Multispectral Photography for Earth Resources, West Hill Printing Co., Huntington, New York, 1972.
8. Jansson, P.; Hunt, R.; Plyler, E., "Resolution Enhancement of Spectra," JOSA, Vol. 60, No. 5, pp. 596-599, May 1970.

9. Pijev, S. and Vetter, G., "Processing Quantum Limited Images," Picture Processing and Psychopictorics, pp. 165-176, Editors B. Lipkin and A. Rosenfeld, Academic Press, New York, 1970.
10. Wasielewski, J., "Automatic Image Evaluation and Plotting System," Application of Reconnaissance Technology to Monitoring and Planning Environmental Change, June 1970.
11. Robinson, N., Solar Radiation, Elsevier Publishing Co., New York, 1966.
12. Valley, S.L., Handbook of Geophysics and Space Environments, Office of Aerospace Research, USAF, 1965.
13. Allen, C.W., Astrophysical Quantities, 2nd Edition, University of London, The Athlone Press, London, 1963.
14. Raytheon Co., "Mission/Data Base Imagery Correlation Technique," Final Report 74-1497, Raytheon Equipment Division, April 1974.



APPENDIX A  
BLACKBODY RADIATION

Blackbody radiation is the radiation emitted by a body due to the thermal energy that the body possesses. For a given temperature, Planck's Law defines the energy radiated from that body as

$$E_{\lambda} d\lambda = \frac{(hc^2/\lambda^5) \cos \theta d\lambda}{\exp (hc/k\lambda T) - 1}$$

where

h	=	Planck's constant	=	$6.626 \times 10^{-34}$	(joule sec)
k	=	Boltzman's constant	=	$1.381 \times 10^{-23}$	(joule/°K)
c	=	speed of light	=	$2.998 \times 10^8$	(m/sec)
$\theta$	=	angle with respect to normal			
T	=	temperature of the body (°K)			
$\lambda$	=	wavelength of the radiation (m)			

For a small band of wavelengths,  $\Delta\lambda$ , Planck's Law is approximately

$$E_{\lambda} \Delta\lambda = \frac{(hc^2/\lambda_0^5) \cos \theta \Delta\lambda}{\exp (hc/k \lambda_0 T) - 1}$$

where  $\lambda_0$  is the center wavelength of the small band.

As the temperature of a body is increased the peak energy output shifts to radiation of smaller wavelengths. The relationship between

the wavelength of the peak energy output,  $\lambda_{\max}$ , and the temperature is given by the Wien displacement law:

$$\lambda_{\max} = .0288/T \text{ (cm)}$$

The temperatures encountered in the atmosphere range from approximately 300°K to 190°K. At 300°K, the peak energy output occurs at approximately  $\lambda = 10\mu$ .

Applying Planck's law to a body of 300°K, at a wavelength of  $10\mu$ , for normal incidence

$$\begin{aligned} E \Delta\lambda &= \frac{(hc^2/(10^{-5})^5) \cos 0 \Delta\lambda}{\exp(hc/k(300)(10^{-5})) - 1} \\ &= \frac{(5.95 \times 10^{-17}) / 10^{-25} \Delta\lambda}{\exp(1.99 \times 10^{-25})/4.14 \times 10^{-26}) - 1} \\ &= \frac{5.95 \times 10^8 \Delta\lambda}{\exp(4.8) - 1} = \frac{5.95 \times 10^8 \Delta\lambda}{1.19 \times 10^2} \\ &= (4.97 \times 10^6 \Delta\lambda) \text{ (watts/m}^2\text{)} \end{aligned}$$

Repeating the same calculation with the wavelength of  $1\mu$ , the long wavelength limit of the photographic spectrum:

$$\begin{aligned}
E \Delta\lambda &= \frac{hc^2/(10^{-6})^5 \cos 0 \Delta\lambda}{\exp (hc/k (300) (10^{-6}) - 1)} \\
&= \frac{(5.95 \times 10^{-17})/10^{-30} \Delta\lambda}{\exp (1.99 \times 10^{-25}/4.14 \times 10^{-27}) - 1} \\
&= \frac{5.95 \times 10^{13} \Delta\lambda}{\exp (48) - 1} = \frac{5.95 \times 10^{13} \Delta\lambda}{7.51 \times 10^{20}} \\
&= 7.92 \times 10^{-8} \Delta\lambda \text{ (watts/m}^3\text{)}
\end{aligned}$$

As can be seen, the radiation emitted at  $1\mu$  is many orders of magnitude less than at  $10\mu$ . But how does this blackbody radiation at  $1.0\mu$  compare in intensity to the solar irradiation at the same wavelength. For a  $\Delta\lambda = .01\mu$ , the value of solar irradiation (without atmospheric attenuation) is  $7.19 \text{ watts/m}^2$  at  $1\mu$ . The value of the blackbody radiation over the same  $\Delta\lambda = .01\mu$ , is merely  $7.92 \times 10^{-16} \text{ watts/m}^2$ . The blackbody radiation is clearly negligible at this  $1\mu$  wavelength when compared to the solar radiation.

## APPENDIX B

### CALCULATION OF ATMOSPHERIC BACKSCATTER

The calculation of the atmospheric backscatter involves applying the Rayleigh molecular law of scattering to the atmospheric cone defined by the sensor's field of view and altitude. (See Figure B-1).

The Rayleigh law for molecular scattering is:

$$I_s = I_o * \beta$$

where

$I_s$  = scattered radiance/unit volume ( $w/m^3$ )

$I_o$  = incident irradiance/unit area ( $w/m^2$ )

and

$\beta$  = scattering function/unit length per steradian ( $m^{-1}$ )

The Rayleigh scattering function,  $\beta$ , is given by the following:

$$\beta = \left( \frac{2\pi^2 (\mu - 1)^2}{N(h)\lambda^4} \right) * (1 + \cos^2 \eta)$$



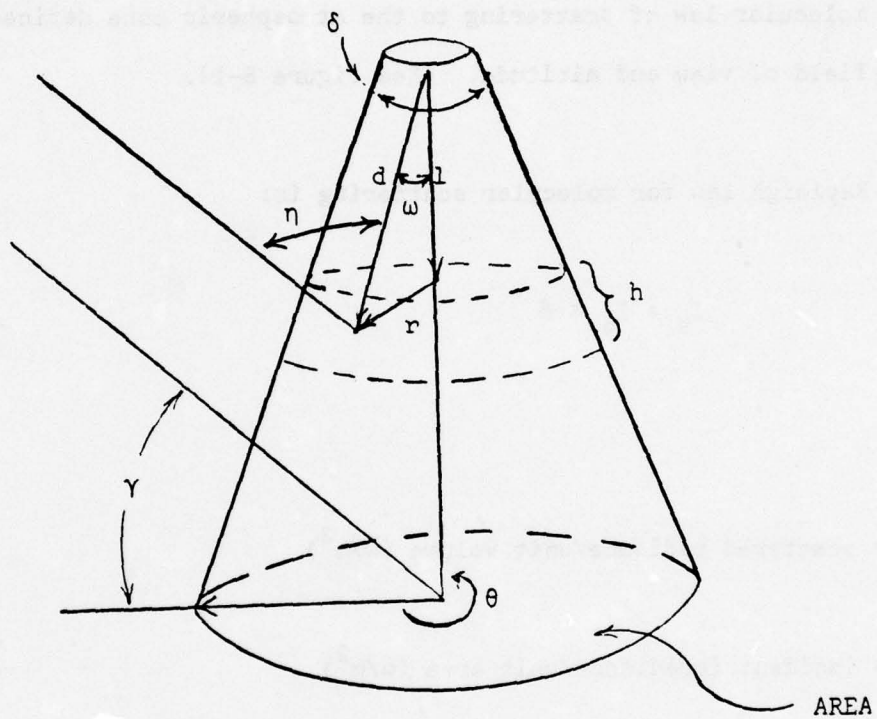


Figure B-1. Atmospheric Cone

where

$\mu$  = refractive index of air

$N(h)$  = atmospheric number density (a function of altitude,  $h$ )

$\lambda$  = wavelength of the radiation

and

$\eta$  = angle between the incident radiation and the scattered radiation

The path luminance (or backscatter),  $D_{TS}$ , is just the percentage of the scattered radiation "captured" by sensor from the volume of the FOV atmospheric cone. So

$$D_{TS} = \int_{VOL} (GCS * I_s) dV$$

$$D_{TS} = \int_{VOL} (GCS * I_o * \beta) dV$$

and  $r = h \tan \omega$ .

where GCS = geometric "capture" cross section/unit area =  $(\frac{1}{d^2})$   
 (See Figure B-1)

$$\therefore D_{TS} = \int_{VOL} \left( \frac{2\pi^2 (\mu - 1)^2}{d^2 N(h) \lambda^4} \right) * (1 + \cos^2 \eta) * I_0 * dV \quad -$$

Dividing up the volume of the cone into layers of circular disks of thickness  $\Delta h$ , the integration over the volume of the cone is approximated by the summation of scattering from these disks. Given this approximation and collecting like terms gives  $D_{TS}$  as

$$D_{TS} = \frac{2\pi^2}{\lambda^4} \sum_h \frac{(\mu - 1)^2}{N(h)} * I_0(h) \Delta h \int_{AREA} \frac{1 + \cos^2 \eta}{d^2} dA$$

where  $I_0(h)$  = the incident solar irradiation on the atmospheric layer at altitude  $h$ . Now letting,

$$K1(\lambda) = \frac{2\pi^2}{\lambda^4},$$

and separating the AREA integration into its component parts gives

$$D_{TS} = K1(\lambda) * \sum_h \frac{(\mu - 1)^2}{N(h)} * I_0(h) \Delta h * \left[ \int_{AREA} \frac{1}{d^2} dA + \int_{AREA} \frac{\cos^2 \eta}{d^2} dA \right]$$

In order to evaluate these two AREA integrations, the integration is performed in cylindrical coordinates, so that integral number 1 becomes:

$$\int_{AREA} \frac{1}{d^2} dA = \int_{r=0}^R \int_{\theta=0}^{2\pi} \left( \frac{1}{d^2} \right) d\theta r dr$$

but  $r = h \tan \omega$ ,  $d = h/\cos \omega$ , and  $dr = h \sec^2 \omega d\omega$  so that integral number 1 becomes

$$\int_{\omega=0}^{\delta/2} \int_{\theta=0}^{2\pi} \left( \frac{\cos^2 \omega h^2 \tan \omega \sec^2 \omega}{h^2} \right) d\omega d\theta$$

$$= \int_{\omega=0}^{\delta/2} \int_{\theta=0}^{2\pi} \tan \omega d\omega d\theta$$

$$= 2\pi \int_{\omega=0}^{\delta/2} \tan \omega d\omega = 2\pi (-\ln \cos \omega) \Big|_0^{\delta/2}$$

$$= 2\pi (-\ln(\cos \delta/2) + \ln(\cos 0))$$

$$= -2\pi \ln(\cos \delta/2)$$

Evaluating the second AREA integral proceeds in a similar manner, so that the second AREA integral becomes

$$\int_{\omega=0}^{\delta/2} \int_{\theta=0}^{2\pi} \tan \omega \cos^2 \eta d\omega d\theta$$

where

$$\cos^2 \eta = \frac{r^2 \cos^2 \theta \cos^2 \gamma - 2rh \cos \theta \cos \gamma \sin \gamma + h^2 \sin^2 \gamma}{r^2 + h^2}$$



Then, substituting for  $r$ ,  $\cos^2 \eta$  becomes

$$\cos^2 \eta = \frac{h^2 \tan^2 \omega \cos^2 \theta \cos^2 \gamma - 2h^2 \tan \omega \cos \theta \cos \gamma \sin \gamma + h^2 \sin^2 \gamma}{h^2 \tan^2 \omega + h^2} -$$

$$= \frac{h^2 (\tan^2 \omega \cos^2 \theta \cos^2 \gamma - 2 \tan \omega \cos \theta \cos \gamma \sin \gamma + \sin^2 \gamma)}{h^2 (\tan^2 \omega + 1)}$$

$$= \frac{(\tan \omega \cos \theta \cos \gamma - \sin \gamma)^2}{\sec^2 \omega}$$

$$= \cos^2 \omega (\tan \omega \cos \theta \cos \gamma - \sin \gamma)^2$$

The second AREA integral then becomes

$$\int_{\omega=0}^{\delta/2} \int_{\theta=0}^{2\pi} \tan \omega \cos^2 \omega (\tan \omega \cos \theta \cos \gamma - \sin \gamma)^2 d\theta d\omega$$

$$= \int_{\omega=0}^{\delta/2} \tan \omega \cos^2 \omega d\omega \int_{\theta=0}^{2\pi} (\tan^2 \omega \cos^2 \theta \cos^2 \gamma - 2 \tan \omega \cos \theta \cos \gamma \sin \gamma + \sin^2 \gamma) d\theta$$

$$= \int_{\omega=0}^{\delta/2} \tan \omega \cos^2 \omega d\omega \left[ \left( \tan^2 \omega \cos^2 \gamma \left( \frac{\theta}{2} + \frac{\sin 2\theta}{4} \right) \Big|_0^{2\pi} \right) - (2 \tan \omega \cos \gamma (\sin \theta) \Big|_0^{2\pi}) + (\sin^2 \gamma (\theta) \Big|_0^{2\pi}) \right]$$

$$= \int_{\omega=0}^{\delta/2} \tan \omega \cos^2 \omega \, d\omega (\pi \tan^2 \omega \cos^2 \gamma + 2\pi \sin^2 \gamma)$$

$$= \pi \cos^2 \gamma \int_{\omega=0}^{\delta/2} \tan^3 \omega \cos^2 \omega \, d\omega + 2\pi \sin^2 \gamma \int_{\omega=0}^{\delta/2} \tan \omega \cos^2 \omega \, d\omega$$

$$= \pi \cos^2 \gamma \int_{\omega=0}^{\delta/2} \frac{\sin^3 \omega}{\cos \omega} \, d\omega + 2\pi \sin^2 \gamma \int_{\omega=0}^{\delta/2} \sin \omega \cos \omega \, d\omega$$

$$= \pi \cos^2 \gamma \int_{\omega=0}^{\delta/2} \frac{(1 - \cos^2 \omega) \sin \omega}{\cos \omega} \, d\omega + 2\pi \sin^2 \gamma \left( \frac{1}{2} \sin^2 \omega \right) \Big|_0^{\delta/2}$$

$$= \pi \cos^2 \gamma \left( \int_{\omega=0}^{\delta/2} \tan \omega \, d\omega - \int_{\omega=0}^{\delta/2} \cos \omega \sin \omega \, d\omega \right) + \pi \sin^2 \gamma \sin^2 \delta/2$$

$$= \pi \cos^2 \gamma \left( (-\ln(\cos \omega)) \Big|_0^{\delta/2} - \left( \frac{1}{2} \sin^2 \omega \right) \Big|_0^{\delta/2} \right) + \pi \sin^2 \gamma \sin^2 \delta/2$$

$$= \pi \cos^2 \gamma (-\ln(\cos \delta/2) - \frac{1}{2} \sin^2 \delta/2) + \pi \sin^2 \gamma \sin^2 \delta/2$$

Combining the 2 AREA integrations,  $D_{TS}$  then becomes

$$D_{TS} = K1 * \sum_h \frac{(\mu - 1)^2}{N(h)} * I_o(h) * \text{AMGDEP} * \Delta h * T2(h)$$

where  $K1 = \frac{2 \pi^2}{\lambda^4}$

$$\begin{aligned} \text{ANGDEP} = & -2\pi \ln(\cos \delta/2) + (\pi \cos^2 \gamma (-\ln(\cos \delta/2) - \frac{1}{2} \sin^2 \delta/2) \\ & + \pi \sin^2 \gamma \sin^2 \delta/2) \end{aligned}$$

and  $T2(h) =$  the atmospheric transmission factor from altitude  $h$  to the sensor

Now, the term,  $(\mu - 1) =$  refractive index - 1, is proportional to the number of scatters  $N(h)$ . The term REFRIX which is (the refractive index) at sea level, computed for  $N$  requires the correction term  $\left(\frac{N(h)}{N(0)}\right)$  to give the correct index of refraction at high altitudes.

Therefore, the (index of refraction - 1) at altitude  $h$  is given by

$$(\mu - 1) = \frac{\text{REFRIX} * N(h)}{N(0)}$$

$$\begin{aligned} \therefore D_{TS} &= K1 * \sum_h \frac{\text{REFRIX}^2 * N(h)}{N(0)^2} * I_o(h) * T2(h) * \text{ANGDEP} * \Delta h \\ &= K1 * \frac{\text{REFRIX}^2}{N(0)^2} * \sum_h N(h) * I_o(h) * T2(h) * \text{ANGDEP} * \Delta h \end{aligned}$$

Also  $I_o(h) = I_o * T1(h)$

where  $T1(h) =$  atmospheric transmission factor from the top of the atmosphere to altitude  $h$ .

Therefore,  $D_{TS} = K3 * \sum_h N(h) * T1(h) * T2(h) * \Delta h$

where  $K3 = K1 * \frac{REFRIX^2}{N(0)^2} * ANGDEP * I_o$



## APPENDIX C

### CALCULATION OF THE NORMALIZED EARTH-SUN DISTANCE

If  $R_o$  is the mean radius of the earth's orbit, then the radius of the orbit at a given point in the orbit is given by the equation (from Kepler's First Law):

$$R = \frac{R_o}{1 + e * (\cos(\theta - 180^\circ - \bar{\omega}_s))}$$

where  $R$  = radius of the orbit

$R_o$  = mean radius of the orbit  $\approx 149.56 \times 10^6$  km

$e$  = eccentricity of the earth's orbit  $\approx .01672$

$\bar{\omega}_s$  = the longitude of the perihelion  $\approx 102^\circ$

and  $\theta$  = the angular position of the orbit as measured from the vernal equinox orbital point (the first point of Aries)

The angle  $\theta$  is defined by the given date. The calculation of  $\theta$  is performed during the calculation for the solar declination (see Appendix D). The form directly usable for correcting the mean solar irradiation values is the inverse normalized earth-sun distance and is given by

$$\left(\frac{R_o}{R}\right) = 1 + .01672 * \cos(\theta - 282^\circ)$$

## APPENDIX D

### CALCULATION OF SOLAR DECLINATION

The calculation of the solar declination involves a rotation of a coordinate system. Assume that the earth revolves around the sun in a circular orbit and the earth axis is not tilted. Then, the solar position can be described by the angle  $\theta$ , setting  $\theta = 0$  at the vernal equinox. With the circular orbit approximation,  $\theta$  is a linear function of time, such that

$$\theta = \left( \frac{360^\circ}{365.25 \text{ days}} \right) \times (\# \text{ of days from vernal equinox})$$

Then, the position of the sun is given by  $P(x,y,z)$  where  $z=0$ ,  $x=\cos\theta$  and  $y=\sin\theta$  (see Figure D-1). Now, to calculate the solar position with the tilt of the earth included, rotate the fixed coordinate system so that the angle between  $z$  and  $z'$  is  $\emptyset = 23.5^\circ$ . Then,

$$\begin{bmatrix} x' \\ y' \\ z' \end{bmatrix} = \begin{bmatrix} 1 & 0 & 0 \\ 0 & \cos\emptyset & -\sin\emptyset \\ 0 & \sin\emptyset & \cos\emptyset \end{bmatrix} \begin{bmatrix} x \\ y \\ z \end{bmatrix}$$

Then  $x'=x$  ;  $y'=y \cos\emptyset - z \sin\emptyset$  and  
 $z'=y \sin\emptyset + z \cos\emptyset$

Substituting  $z=0$ ,  $x=\cos\theta$  and  $y=\sin\theta$  into the above:  $x'=\cos\theta$ ,  $y'=\sin\theta \cos\emptyset$  and  $z'=\sin\theta \sin\emptyset$

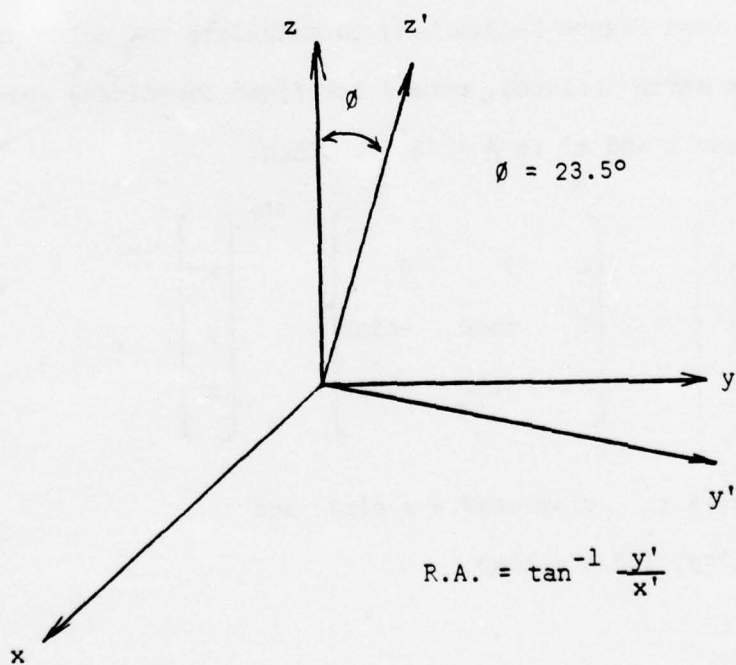
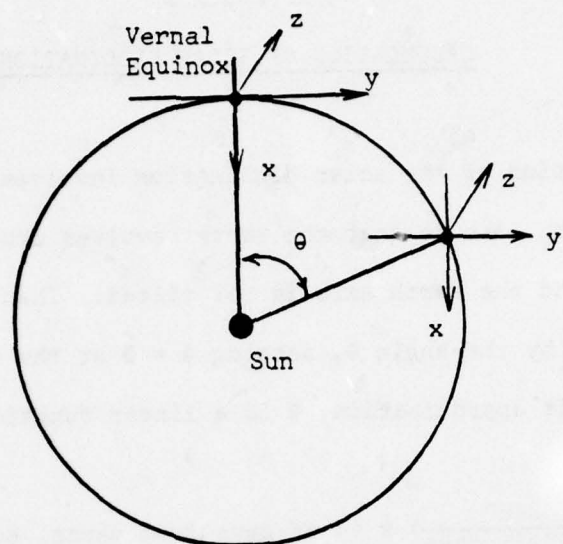


Figure D-1

With  $\phi = 23.5^\circ$ ,

$$y' = .917 \sin\theta \text{ and } z' = .398 \sin\theta$$

The solar declination, the angle between  $z$  and  $z'$ , is

$$\delta = \sin^{-1} z'$$

$$\delta = \sin^{-1}(.398 \sin\theta)$$

To achieve a slightly better approximation of  $\delta$ , instead of assuming a strictly circular orbit, i.e., linear  $\frac{d\theta}{dt}$  throughout the year, assume that  $\frac{d\theta}{dt}$  is linear between the two equinoxes. So that  $\theta$  from March 21 to September 23 is given by

$$\theta = \frac{180^\circ}{186} \times \# \text{ of days from V.E.}$$

and from September 23 to March 21,  $\theta$  is given by

$$\theta = \left[ \frac{180^\circ}{179} \times \# \text{ of days from A.E.} \right] + 180^\circ$$

This will help to correct for the elliptical nature of the earth's orbit.



## APPENDIX E

### CALCULATION OF SOLAR ELEVATION ANGLE

The value of the solar elevation angle,  $\gamma$ , can be calculated through the use of the formula:

$$\sin \gamma = \sin \delta \sin \phi + \cos \delta \cos \phi \cos t_s$$

where  $\delta$  is the solar declination,  $t_s$  is the hour angle of the sun, and  $\phi$  is the latitude of the location. The above formula is just a transformation from one spherical coordinate system to another.

The hour angle,  $t_s$ , is defined as the angle between the celestial meridian and hour circle. The celestial meridian is the great circle containing the north celestial pole, the local zenith, and the south celestial pole. The hour circle is the great circle containing the object of interest (i.e., the sun), and the two poles. The hour angle,  $t_s$ , is thus a function of the time of day and the longitude,  $\Lambda$ , and is given by

$$t_s = (z + \Delta z) + \Lambda + \text{Eq.T.} - 12^h$$

where  $z$  = the local zonal time,  $\Delta z$  = the time zone corresponding to the local time, and the Eq.T. (Equation of Time) is a correction factor used to account for the difference between the true solar position and the mean solar position upon which our time values are based. The relation between

the longitude and time is  $24^h=360^\circ$ ,  $1^h=15^\circ$ ,  $1^m=15'$ , and  $1^s=15''$ . The time zones in the United States are given by;  $\Delta z=+5$  for E.S.T.,  $\Delta z=+6$  for C.T.,  $\Delta z=+7$  for M.T. and  $\Delta z=+8$  for P.T. Longitude is measured from Greenwich Meridian in a positive direction to the east, therefore, in a negative\_ direction to the west. The solar declination will be calculated by the following formula (see Appendix D)

$$\delta = \sin^{-1}(.398 \sin \theta)$$

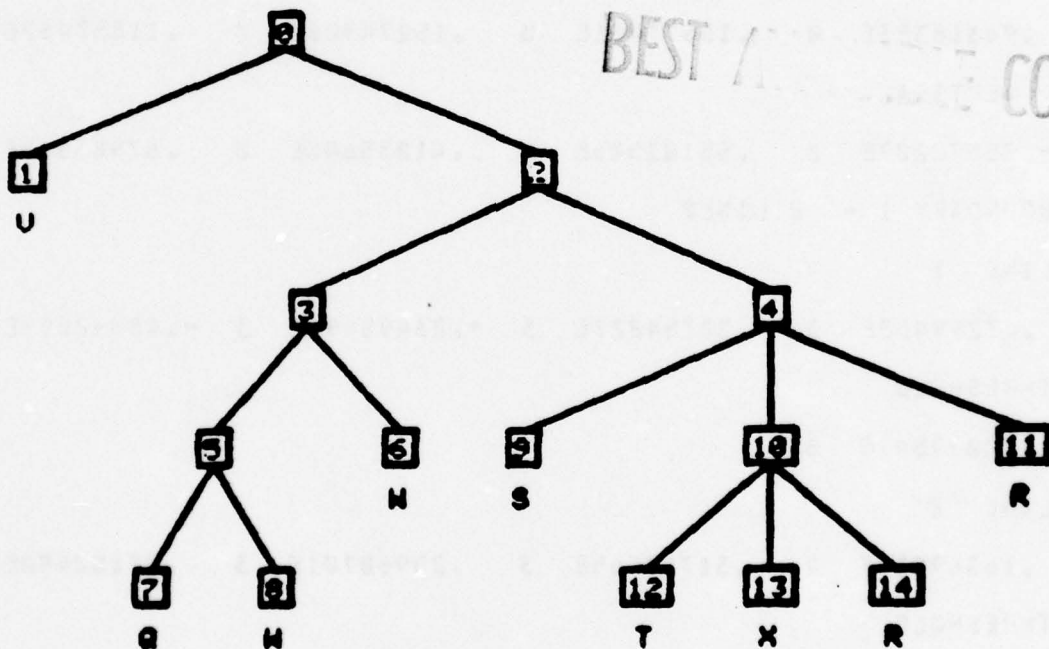
The Equation of Time is given by a combination of two sin functions. The first function accounts for the change in the period of time between two consecutive transits of the sun across a given meridian due to changing velocity of a body in an elliptical orbit. This equation is called the Equation of Time due to eccentricity (of the orbit). The second function accounts for the different relative angular velocity of the earth relative to the hour circles due to the obliquity of the ecliptic. This equation is called the Equation of Time due to obliquity. Combining both functions gives the total Equation of Time, which is given by the following

$$\begin{aligned} \text{EQT} = & 1.875 * \sin(2 \pi \frac{\# \text{ of days from Dec. } 30}{365}) \\ & + 2.25 * \sin(4 \pi * (\frac{\# \text{ of days from Jan. } 10}{365})) \text{ degrees} \end{aligned}$$

# APPENDIX F: CLASSIFICATION LOGIC

The logic used for detecting camouflaged targets (as outlined in Section 7) is presented in detail here. Below we review the symbolism used and the logic tree. The mathematical description of the logic at each node is given on the remaining pages of this appendix.

V - vegetation	S - bare soil
W - coniferous vegetation	T - camouflaged tactical target
X - shadow in W region	Q - camouflaged target covered with netting.



Logic Tree

-----  
NODE 0

5\*(M1-M4)>M4

-----

Node 0: Boolean Logic

-----  
NODE 2

PROJECTION: Eigenvectors of class T covariance matrix.

HORIZONTAL

.96318383E 0 .18677461E 0 .15274906E 0 .11857432E 0

VERTICAL

-.25570207E 0 .55103506E 0 .41085640E 0 .67983368E 0

BOUNDARY 1 - 2 LINES

LINE 1

.87299403E 3 -.32754227E 3 -.23495499E 3 -.48092099E 3

THRESHOLD

-.30029547E 5

LINE 2

.16369938E 4 .31743565E 3 .25960701E 3 .20152480E 3

THRESHOLD

.50517100E 6

-----

Node 2: Two-Space Logic



-----  
NODE 3  
-----

PROJECTION: Eigenvectors (two largest eigenvalues) of class Q covariance  
matrix.

HORIZONTAL

.89063959E 0 .14376872E 0 .16080062E 0 -.40029342E 0

VERTICAL

.40502720E 0 .35981622E -1 -.12439586E -2 .91359550E 0

BOUNDARY 1 - 4 LINES

LINE 1

-.53170954E 4 -.47235770E 3 .16330376E 2 -.11993452E 5

THRESHOLD

-.35438630E 7

LINE 2

-.62701072E 4 -.10121325E 4 -.11320372E 4 .28180677E 4

THRESHOLD

-.13450725E 7

LINE 3

.53290709E 4 .47342157E 3 -.16367156E 2 .12020465E 5

THRESHOLD

.35100147E 7

LINE 4

.60699974E 4 .97983043E 3 .10959083E 4 -.27281293E 4

THRESHOLD

.12616497E 7  
-----

Node 3: Two-Space Logic

PROJECTION:

HORIZONTAL = Fisher direction for classes T and S.

,45600000E -1 ,13000000E 0 -,43900000E 0 -,77000000E 0

VERTICAL : Measurement 4.

,00000000E 0 ,00000000E 0 ,00000000E 0 ,10000000E 1

BOUNDARY 1 = 3 LINES

LINE 1

-,18014132E 3 -,51356077E 3 ,17342552E 4 -,56701401E 4

THRESHOLD

-,82772283E 6

LINE 2

,19176334E 3 ,54669372E 3 -,18461426E 4 -,34870233E 4

THRESHOLD

-,87781972E 6

LINE 3

,35156612E 3 ,10022716E 4 -,33845948E 4 -,25299026E 3

THRESHOLD

-,51433913E 6

BOUNDARY 2 = 2 LINES

LINE 1

-,47214458E 3 -,13460262E 4 ,45454270E 4 ,79726168E 4

THRESHOLD

,20955506E 7

LINE 2

,14527525E 1 ,41416191E 1 -,13985929E 2 ,87704403E 4

THRESHOLD

,16193014E 7

Node 4: Two-Space Logic

-----  
NODE 5  
-----

PROJECTION: Eigenvectors (two smallest eigenvalues) of the class Q  
covariance matrix.

HORIZONTAL

-.13463923E 0 -.87904246E -1 .98487855E 0 .64493131E -1

VERTICAL

-.15680036E 0 .98504249E 0 .64465914E -1 .30807043E -1

BOUNDARY 1 - 4 LINES

LINE 1

.34847141E 4 -.21891478E 5 -.14326835E 4 -.68465238E 3

THRESHOLD

-.43887950E 7

LINE 2

.31390959E 4 .20494760E 4 -.22962314E 5 -.15036489E 4

THRESHOLD

-.43215332E 7

LINE 3

-.34717598E 4 .21810097E 5 .14273575E 4 .68210721E 3

THRESHOLD

.43403198E 7

LINE 4

-.30474137E 4 -.18997792E 4 .22202230E 5 .14560725E 4

THRESHOLD

.41625893E 7  
-----

Node 5: Two-Space Logic

PROJECTION: Optimal Discriminant Plane for classes T and X.

HORIZONTAL

-.21220253E -1 -.39759549E 0 -.31902436E 0 .35150833E 0

VERTICAL

-.18707487E -3 .20514457E -1 .27225758E -1 -.30595796E -1

BOUNDARY 1 - 3 LINES

LINE 1

.45991476E 3 -.35106078E 3 -.43011642E 4 .49623370E 4

THRESHOLD

-.21651758E 4

LINE 2

-.90644934E 2 -.37011809E 4 -.38673999E 4 .43110381E 4

THRESHOLD

-.81748907E 6

LINE 3

-.54062968E 3 -.19056672E 4 .21567686E 4 -.25810652E 4

THRESHOLD

-.56865370E 6

BOUNDARY 2 - 2 LINES

LINE 1

.53743198E 3 .86871850E 4 .63508571E 4 -.69631106E 4

THRESHOLD

.20163782E 7

LINE 2

-.41961633E 3 -.13397839E 4 .18482356E 4 -.21987672E 4

THRESHOLD

-.40607861E 6

Node 10: Two-Space Logic



APPENDIX G  
IMAGERY AVAILABLE FOR ADET PROGRAM

1. Sensor: Spectral Data

<u>Msn #</u> GR73-102	<u>Date Flown</u> 17 Sept. 73	<u>Overall Quality</u> Excellent
<u>Altitude</u> 3,000'-30,800'(AGL)	<u>Film Type</u> 2424	<u>Weather Conditions</u> clear and sunny
<u>Filter</u>	<u>Lens Setting/fl</u>	<u>f-stop</u>
354	9"	8 - 11
5530A	4"	2.8
208	5"	4 - 5.6
219	22"	8 - 11

2. Sensor: Spectral Data

<u>Msn #</u> GR73-103	<u>Date Flown</u> 17 Sept. 73	<u>Overall Quality</u> Excellent
<u>Altitude</u> 5,000'-45,000'(AGL)	<u>Film Type</u> 2424	<u>Weather Conditions</u> clear and sunny
<u>Filter</u>	<u>Lens Setting/fl</u>	<u>f-stop</u>
354	9"	8 - 11
5530A	4"	2.8
357	9"	4 - 5.6
216	19"	5.6 - 8

3. Sensor Spectral Data

<u>Msn #</u> GR73-104	<u>Date Flown</u> 19 Sept. 73	<u>Overall Quality</u> Excellent
<u>Altitude</u> 3,000'-30,000'(AGL)	<u>Film Type</u> 2424	<u>Weather Conditions</u> clear
<u>Filter</u>	<u>Lens Setting/fl</u>	<u>f-stop</u>
354	9"	5.6
5530A	4"	2.8 - 4
208	5"	4 - 5.6
219	22"	8 - 11

4. Sensor: Spectral Data

<u>Msn #</u>	<u>Date Flown</u>	<u>Overall Quality</u>
GR73-110	11 Oct. 73	Excellent
<u>Altitude</u>	<u>Film Type</u>	<u>Weather Conditions</u>
1,500'-17,500'(AGL)	2424	clear
<u>Filter</u>	<u>Lens Setting/fl</u>	<u>f-stop</u>

- Data not recorded on mission data sheet -

5. Sensor: Spectral Data

<u>Msn #</u>	<u>Date Flown</u>	<u>Overall Quality</u>
GR74-081	5 Oct. 74	
<u>Altitude</u>	<u>Film Type</u>	<u>Weather Conditions</u>
16,000'-26,000'(AGL)	SO 289	
41,000'-51,000'(AGL)		
<u>Filter</u>	<u>Lens Setting/fl</u>	<u>f-stop</u>
5000	3"	2.8
5600	16"	2.8
6800	9"	2.8
8600	25"	5.6

6. Sensor: Spectral Data

<u>Msn #</u>	<u>Date Flown</u>	<u>Overall Quality</u>
GR74-084	9 Oct. 74	
<u>Altitude</u>	<u>Film Type</u>	<u>Weather Conditions</u>
6,000'(AGL)	2424	
<u>Filter</u>	<u>Lens Setting/fl</u>	<u>f-stop</u>
5000	3"	2.8
5600	16"	2.8
6800	9"	2.8
8600	25"	5.6

7. Sensor: Spectral Data

Msn #  
GR74-056

Date Flown  
7 Aug. 74

Overall Quality -  
Good

Altitude  
9,000', 5,000'  
15,000', 2,500' (AGL)

Film Type  
SO-289

Weather Conditions  
Clear

Filter

Lens Setting/f1

f-stop

5000  
5600  
6800  
8600

3"  
16"  
9"  
25"

2.8 - 4.0  
2.8 - 4.0  
2.8  
4.0 - 5.6

8. Sensor: Spectral Data

Msn #  
CR74-62

Date Flown  
22 Aug. 74

Overall Quality  
Good

Altitude  
20,000', 15,000'  
10,000', 5,000' (Poor)  
2,500' (AGL)

Film Type  
SO-289

Weather Conditions  
Low Cloud Cover on  
1<sup>st</sup> 5,000' pass  
Clear to partially  
cloudy

Filter

Lens Setting/f1

f-stop

4400  
5600  
6200  
8320

9"  
16"  
5"  
24"

4 - 5.6  
2.8 - 4.0  
4.0 - 5.6  
4.0

9. Sensor: Spectral Data

Msn #  
GR74-71

Date Flown  
19 Sept. 74

Overall Quality  
Good

Altitude  
15,000', 10,000' (AGL)

Film Type  
2424

Weather Conditions  
Clear

Filter

Lens Setting/f1

f-stop

5000  
5600  
6800  
8600

3"  
16"  
9"  
25"

2.8  
2.8  
2.8  
5.6

Mission: GR74-58

12 August 1974 PM

Film: SO-289

Speed: 1/250 sec.

<u>Filters</u>	<u>Band</u>	<u>Aperture</u>	<u>Focus</u>
4400	1	f4.0-5.6	9
5600	2	f2.8-4.0	16
6200	3	f4.0-5.6	5
8300	4	f4.0	24



APPENDIX H

TABLE SHOWING FILM RESOLUTION

Focal Length = 150 mm; Mission GR74-58; Date 12 August 1974; Camera Spectral Data; Film SO-289

RESOLUTION*													
FRAME	FORMAT POS	ALTITUDE IN FEET AGL	# OF GREY SHADES	L OF		XL OF		IMAGE RESOLUTION (LINES/MM)		GROUND RESOLUTION IN FEET			
				GRP. #	WIDTH OF BAR & SPACE	GRP. #	WIDTH OF BAR & SPACE	L OF	XL OF	L OF	XL OF		
Pos.	148	I	3	3	2.82'	7	1.4'	4.94	9.96	2.81	1.19		
Pos.	148	II	2	3	2.82'	7	1.4'	4.94	9.96	2.81	1.19		
Pos.	148	III	3	7	1.4'	9	1.00'	9.96	13.95	1.39	.99		
Pos.	148	IV	2	3	2.82'	5	2.00'	4.94	6.97	2.81	1.98		
Neg.	148	I	2	3	2.82'	6	1.64'	4.94	8.50	2.81	1.63		
Neg.	148	II	3	3	2.82'	6	1.64'	4.94	8.50	2.81	1.63		
Neg.	148	III	4	7	1.4'	8	1.2'	9.96	11.62	1.39	1.19		
Neg.	148	IV	3	4	2.34'	6	1.64'	5.96	8.50	2.32	1.63		

\* Results of interpreter analysis of coverage over Floyd, NY, Test Annex Resolution Target.

## APPENDIX I

### ADET - SITE INFORMATION

Members of RRC have provided extensive ground data concerning the Stockbridge and Floyd test sites. These are in the form of line drawings showing the breakdown of "ADET" scenes into various categories including speciation of vegetation, emplacement of artillery, and locations of military vehicles and cultural structures, as well as, general terrain categories.

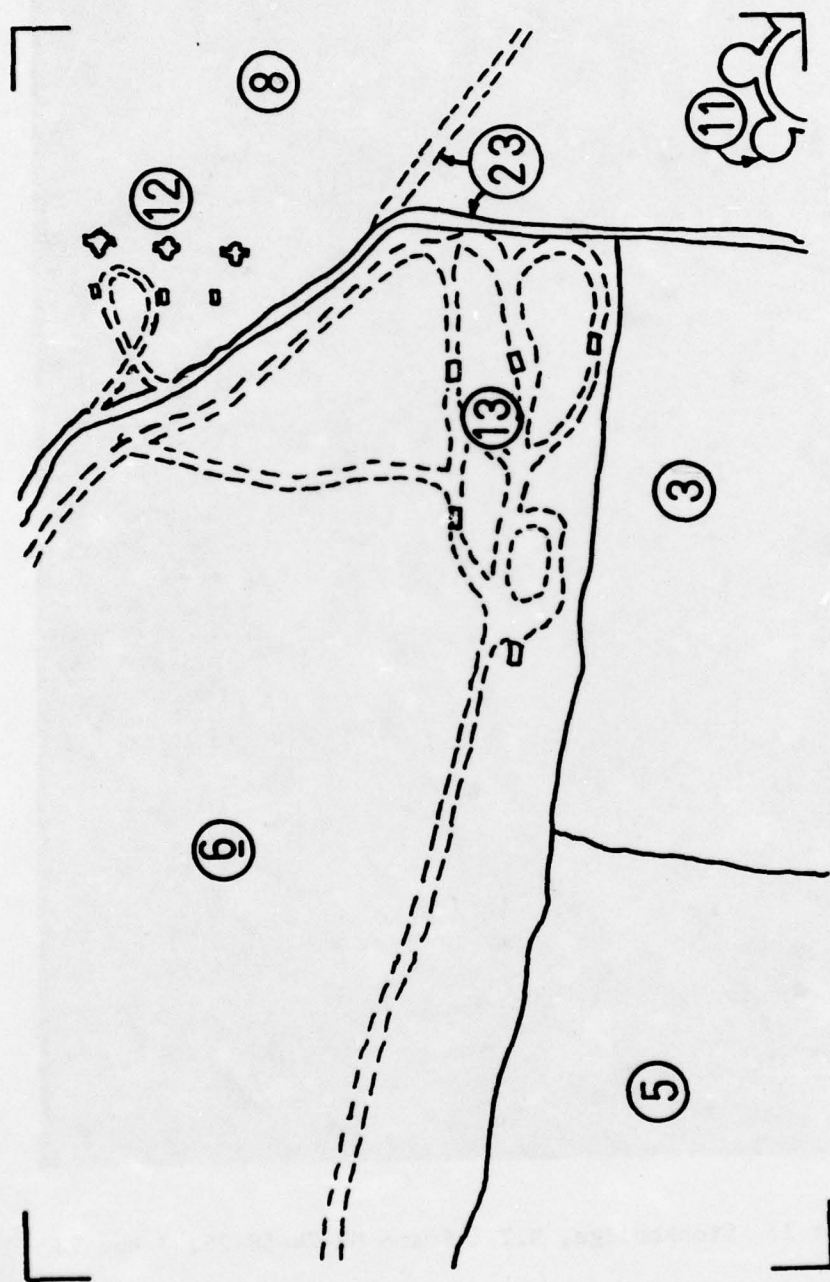
ADET - Key For Stockbridge and Floyd Ground Data

1. Sumac & Apple Trees
2. Scrub & Apple Orchard
3. Spruce Plantation
4. White Pine
5. Mixed Hardwood
6. Light Scrub
7. Heavy Scrub
8. Meadow
9. Crop
10. SAM Site - 10-A-1
11. AAA - 10-A-2
12. Heavy Mortar - 10-A-3
13. Armor Site - 10-A-12
14. Ground Defensive Positions - 10-A-4
15. Heavy Artillery Battery - 10-A-5
16. Mounted Convoy - 10-A-6
17. V/STOL - 10-A-13
18. Water
19. Antennae - Metal
20. Concrete Building
21. Metal Building
22. Wood Building
23. Dirt Road
24. Paved Road
25. Antennae, Wooden
26. Scud Site - 10-A-10
27. Gravel Bed
28. Scotch Pine
29. Seimans Star

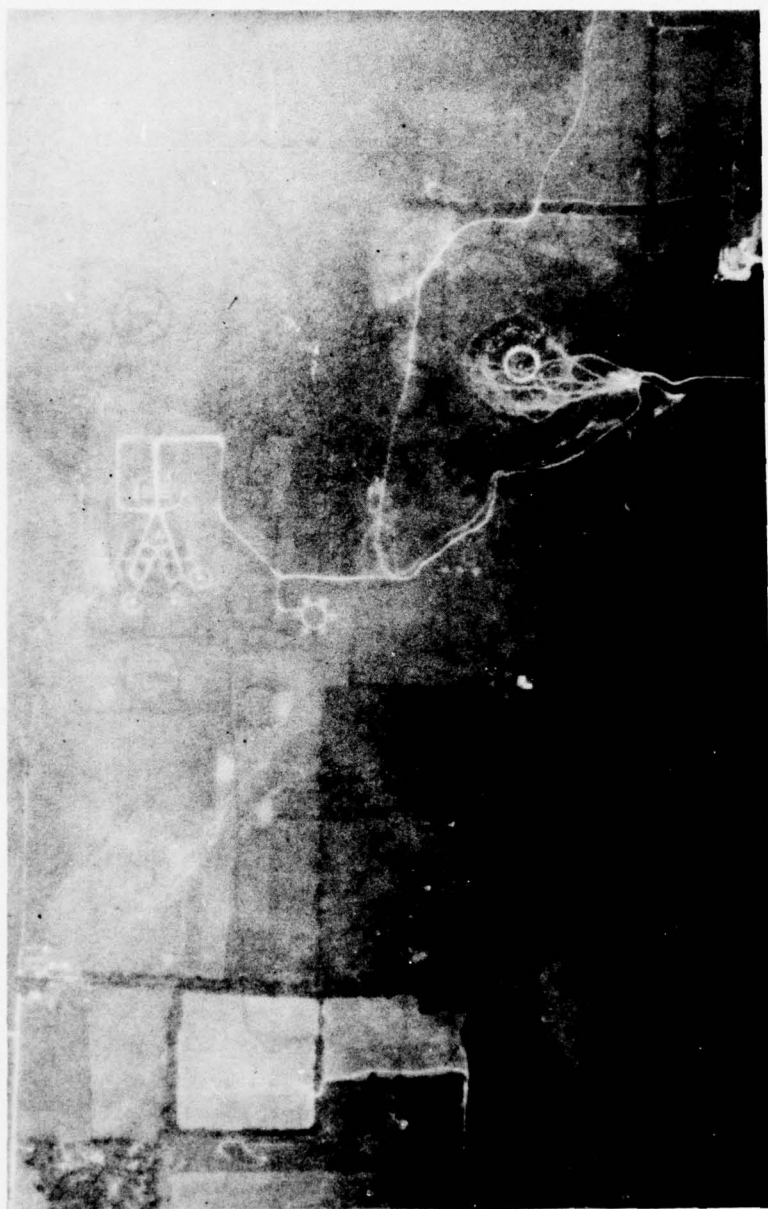




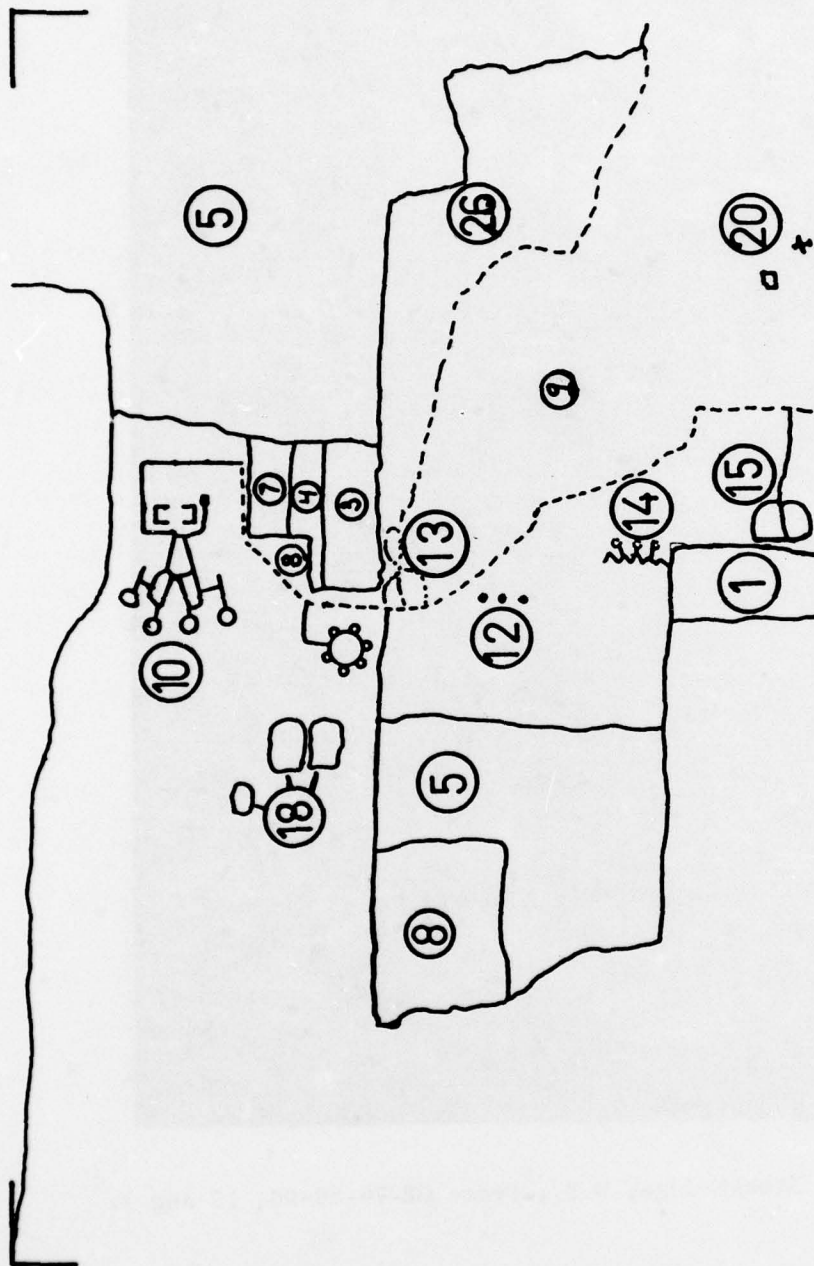
Adet 1: Stockbridge, N.Y.; Frame GR-74-58-25, 7 Aug 74



1 ADET 1



Adet 2: Stockbridge, N.Y.; Frame GR-74-58-90, 12 Aug 74

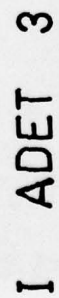


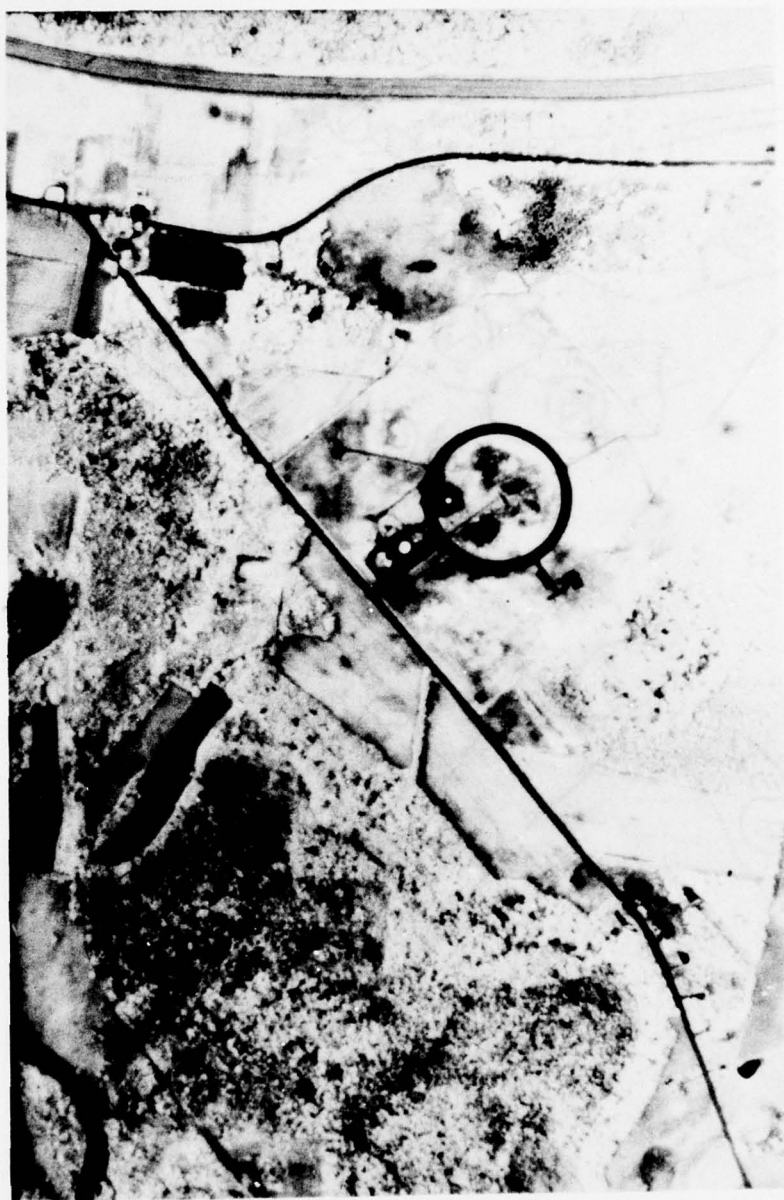
I ADET 02



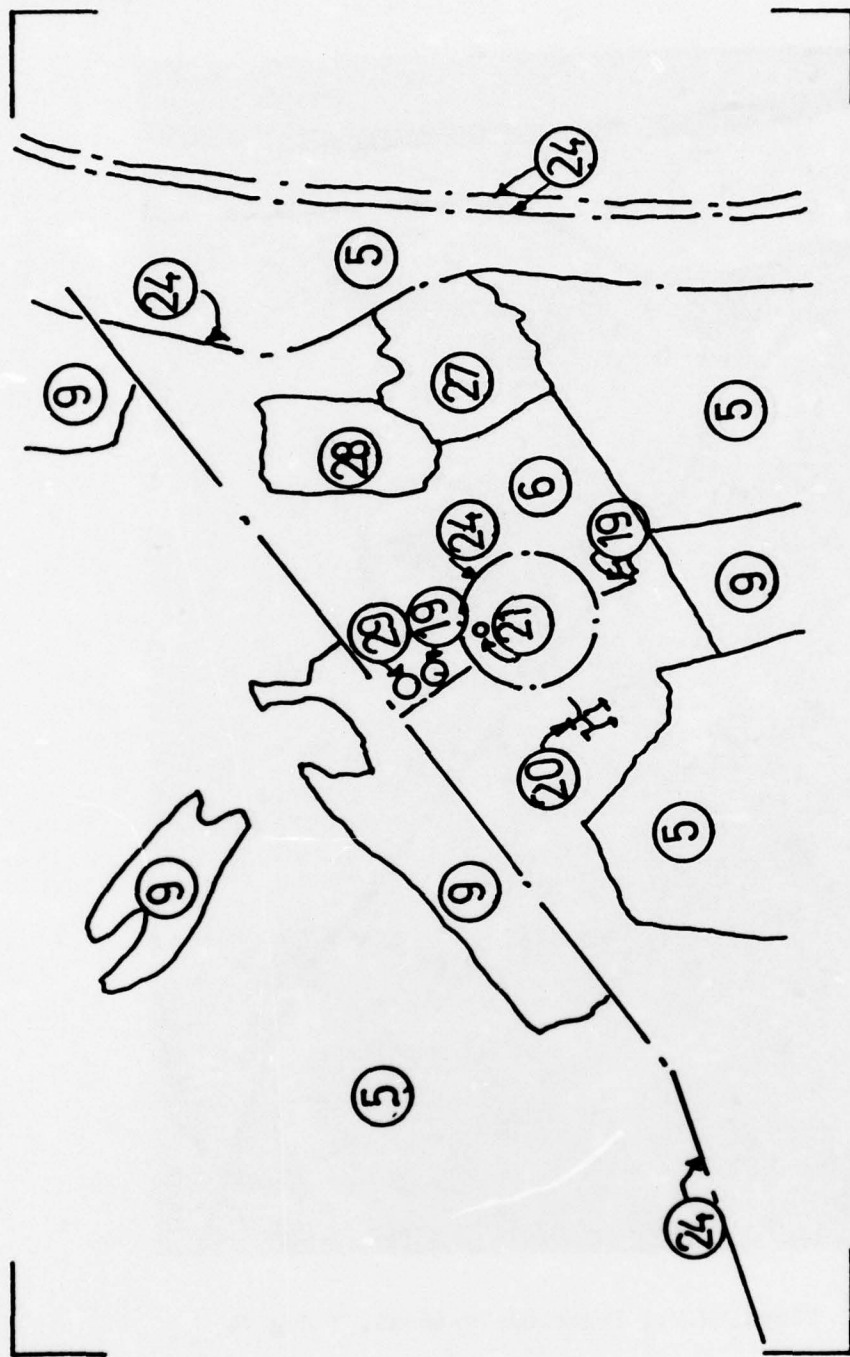


Adet 3: Stockbridge, N.Y.; Frame GR-74-58-50, 12 Aug 74





Adet 4: Floyd, N.Y.; Frame GR-74-56-30, 7 Aug 74

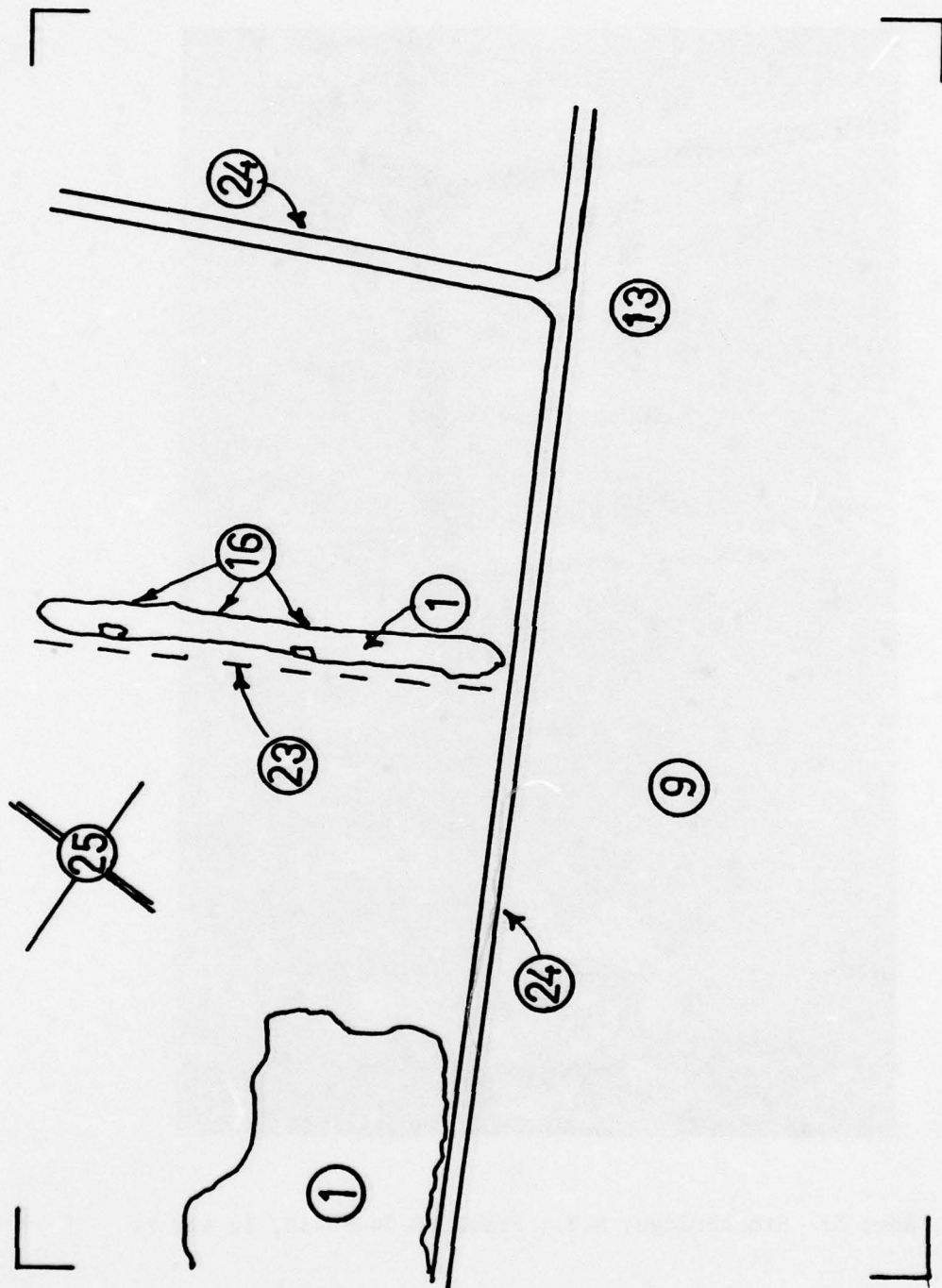


I ADET 04





Adet 5: Stockbridge, N.Y.; Frame GR-74-58-30, 12 Aug 74



IV ADET 05

# METRIC SYSTEM

## BASE UNITS:

Quantity	Unit	SI Symbol	Formula
length	metre	m	...
mass	kilogram	kg	...
time	second	s	...
electric current	ampere	A	...
thermodynamic temperature	kelvin	K	...
amount of substance	mole	mol	...
luminous intensity	candela	cd	...

## SUPPLEMENTARY UNITS:

plane angle	radian	rad	...
solid angle	steradian	sr	...

## DERIVED UNITS:

Acceleration	metre per second squared	...	m/s
activity (of a radioactive source)	disintegration per second	...	(disintegration)/s
angular acceleration	radian per second squared	...	rad/s
angular velocity	radian per second	...	rad/s
area	square metre	...	m
density	kilogram per cubic metre	...	kg/m
electric capacitance	farad	F	A-s/V
electrical conductance	siemens	S	A/V
electric field strength	volt per metre	...	V/m
electric inductance	henry	H	V-s/A
electric potential difference	volt	V	W/A
electric resistance	ohm	...	V/A
electromotive force	volt	V	W/A
energy	joule	J	N-m
entropy	joule per kelvin	...	J/K
force	newton	N	kg-m/s
frequency	hertz	Hz	(cycle)/s
illuminance	lux	lx	lm/m
luminance	candela per square metre	...	cd/m
luminous flux	lumen	lm	cd-sr
magnetic field strength	ampere per metre	...	A/m
magnetic flux	weber	Wb	V-s
magnetic flux density	tesla	T	Wb/m
magnetomotive force	ampere	A	...
power	watt	W	J/s
pressure	pascal	Pa	N/m
quantity of electricity	coulomb	C	A-s
quantity of heat	joule	J	N-m
radiant intensity	watt per steradian	...	W/sr
specific heat	joule per kilogram-kelvin	...	J/kg-K
stress	pascal	Pa	N/m
thermal conductivity	watt per metre-kelvin	...	W/m-K
velocity	metre per second	...	m/s
viscosity, dynamic	pascal-second	...	Pa-s
viscosity, kinematic	square metre per second	...	m/s
voltage	volt	V	W/A
volume	cubic metre	...	m
wavenumber	reciprocal metre	...	(wave)/m
work	joule	J	N-m

## SI PREFIXES:

Multiplication Factors	Prefix	SI Symbol
1 000 000 000 000 = 10 <sup>12</sup>	tera	T
1 000 000 000 = 10 <sup>9</sup>	giga	G
1 000 000 = 10 <sup>6</sup>	mega	M
1 000 = 10 <sup>3</sup>	kilo	k
100 = 10 <sup>2</sup>	hecto*	h
10 = 10 <sup>1</sup>	deka*	da
0.1 = 10 <sup>-1</sup>	deci*	d
0.01 = 10 <sup>-2</sup>	centi*	c
0.001 = 10 <sup>-3</sup>	milli	m
0.000 001 = 10 <sup>-6</sup>	micro	μ
0.000 000 001 = 10 <sup>-9</sup>	nano	n
0.000 000 000 001 = 10 <sup>-12</sup>	pico	p
0.000 000 000 000 001 = 10 <sup>-15</sup>	femto	f
0.000 000 000 000 000 001 = 10 <sup>-18</sup>	atto	a

\* To be avoided where possible.



# *MISSION of Rome Air Development Center*

RADC plans and conducts research, exploratory and advanced development programs in command, control, and communications (C<sup>3</sup>) activities, and in the C<sup>3</sup> areas of information sciences and intelligence. The principal technical mission areas are communications, electromagnetic guidance and control, surveillance of ground and aerospace objects, intelligence data collection and handling, information system technology, ionospheric propagation, solid state sciences, microwave physics and electronic reliability, maintainability and compatibility.

